# DETECTION OF MICROWAVE EMISSION OF EXTENSIVE AIR SHOWERS WITH THE CROME EXPERIMENT

Zur Erlangung des akademischen Grades eines

DOKTORS DER NATURWISSENSCHAFTEN

von der Fakultät für Physik des
Karlsruher Instituts für Technologie (KIT)

genehmigte

DISSERTATION

von

DIPL.-PHYS. FELIX WERNER
aus Bad Ems

Tag der mündlichen Prüfung: 13. Dezember 2013
Referent: Prof. Dr. J. Blümer
Korreferent: Prof. Dr. G. Quast
Betreuer: Dr. R. Engel

November 2013

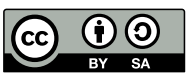

# CONTENTS

# ACRONYMS

| | |
|---|---|
| ADC | analog-to-digital converter |
| AM | amplitude modulation |
| ANKA | Ångströmquelle Karlsruhe |
| CL | confidence level |
| CMB | cosmic microwave background |
| CoREAS | CORSIKA-based Radio Emission from Air Showers |
| CORSIKA | Cosmic-Ray Simulations for KASCADE |
| CROME | Cosmic-Ray Observation via Microwave Emission |
| CW | continuous wave |
| DAQ | data acquisition |
| ECEF | Earth-Centred Earth-Fixed |
| FIR | finite impulse response |
| GPS | Global Positioning System |
| GRASP | General Reflector Antenna Software Package |
| IF | intermediate frequency |
| KASCADE | Karlsruhe Shower Core and Array Detector |
| KRETA | KASCADE Reconstruction for Extensive Air Showers |
| $LN_2$ | liquid nitrogen |
| LNA | low-noise amplifier |
| LNB | low-noise block |
| LNBf | low-noise block feed |
| LO | local oscillator |
| LPDA | log-periodic dipole array |
| LSB | least significant bit |
| LTP | local tangent plane |
| PMT | photomultiplier tube |

| | |
|---|---|
| PPS | pulse-per-second |
| RF | radio frequency |
| RFI | radio frequency interference |
| RMS | root mean square |
| SBAS | Satellite Based Augmentation System |
| SMA | SubMiniature version A |
| SMC | sheet moulding compound |
| VCO | voltage controlled oscillator |

# 1 INTRODUCTION

The Earth is exposed to a continuous flux of charged particles, called *cosmic rays*, which originates from outside of the solar system. The energies of cosmic rays reach up to $\sim 10^{20}$ eV, many orders of magnitude higher than those obtained in man-made accelerators. Cosmic rays of the highest energies are messengers of exceptional non-thermal processes and allow us to study astrophysical objects and the laws of physics under extreme conditions.

One of the central questions of astroparticle physics is that of understanding particle acceleration up to such high energies and identifying the astrophysical objects in which these acceleration processes take place. The key observables to learn more about the sources of cosmic rays are the energy-dependent flux and mass composition of the particles.

Due to the low flux of less than one particle per square kilometre and century, ultra-high energy cosmic rays are studied using ground-based observatories covering several thousand square kilometres, employing the Earth's atmosphere as a calorimeter. The collisions of the cosmic ray particles with the atmospheric molecules lead to the development of cascades of secondary particles, *extensive air showers*. The observation of the longitudinal development of an extensive air shower, in particular the depth of the shower maximum, yields the best estimate of the mass of the primary cosmic ray. Currently, only optical detection techniques, namely the detection of fluorescence and Cherenkov light in the UV, allow this kind of observation. However, optical observations have two drawbacks: First, they strongly depend on the local atmospheric conditions since UV light is scattered by clouds and the highly-variable aerosol content in the atmosphere. Properly accounting for these effects requires the application of an extensive program for atmospheric monitoring and corresponding corrections in data analysis with significant systematic uncertainties. Second, the signals are very faint which restricts the observation time to dark nights with clear atmospheric conditions. Altogether, this leads to duty cycles of less than 15 %. With the study of the mass composition of particles of the highest energies being constrained mainly by the limited aperture of the current generation of cosmic ray observatories, the development of new observation techniques to reach even higher apertures is the key to making significant progress in the field.

In 2008, Gorham and colleagues proposed a new observation technique for extensive air showers. Based on accelerator experiments at an equivalent energy of $3 \times 10^{17}$ eV they concluded that the bremsstrahlung emission of low-energy electrons in the tenuous plasma induced by the particles of an air shower should provide a detectable flux of radio waves at microwave frequencies. Moreover, the emission would be isotropic, enabling the observation of the longitudinal development of an air shower similar to the observation with fluorescence telescopes. However, unlike UV light, microwave radiation below $\sim$ 10 GHz

propagates nearly unattenuated through the atmosphere, even through clouds and rain. At the same time, the amount of background radiation is very low and nearly independent of solar radiation, allowing continuous operation during day and night. Furthermore, highly-optimised and inexpensive off-the-shelf detection electronics is readily available from mass-markets such as satellite TV reception. Therefore, the microwave observation of extensive air showers could have the potential to combine the advantages of measuring the longitudinal development of an air shower with a very high duty cycle and small dependence on the environmental conditions, making it a very promising technology for studying cosmic rays at ultra-high energies.

The aim of this work was to set up an experiment to search for microwave signals of extensive air showers. The KASCADE-Grande air shower array at the Karlsruhe Institute of Technology provided an ideal environment since it allowed the measurement of showers up to the equivalent energy of the accelerator experiment by Gorham et al. Several microwave antennas were installed in the KASCADE-Grande array and a suitable data acquisition system, triggered by the air shower array, was developed. This experimental setup, called Cosmic-Ray Observation via Microwave Emission (CROME), provided one of the first unambiguous detections of a GHz signal of an air shower and allowed the first experimental investigation of the overall emission characteristics. In November 2012, KASCADE-Grande was finally shut down, which also lead to the termination of the data taking with CROME.

After an introduction to cosmic rays and extensive air showers in Chap. 2, the basics of the physics of radio detection are presented in Chap. 3. The experimental setup of CROME, which had to be developed from scratch as no other experiments of similar configuration existed at this time, is then discussed in Chap. 4. This setup was modified in the data taking phase according to the experiences gained. Studies of the detector response and stability as well as the calibration of the different detector components are described in Chap. 5. In the second part of this work, Chap. 6, an analysis and interpretation of the CROME dataset is given. A short overview of the air showers for which a microwave signal has been detected is given in Appendix C.

The results of this thesis have been submitted to Physical Review Letters for publication.

# 2

# COSMIC RAYS AND EXTENSIVE AIR SHOWERS

In this chapter, the current status of the research of cosmic rays is briefly summarised with focus on hadronic cosmic rays at the highest energies. This review follows Ref. [1] and is further based on Refs. [2–4] and references therein. After introducing the well-established observation techniques the recent developments in the new field of microwave detection of extensive air showers are summarised.

## 2.1 COSMIC RAYS

In 1912, more than a century ago, V. F. Hess published measurements of the increasing intensity of ionising radiation with altitude, which he attributed to an extraterrestrial radiation [9]. The term *cosmic rays* that has been established since refers to the flux of particles originating outside of our solar system. These particles cover an energy range of more than ten orders of magnitude, from $10^9$ eV up to at least $10^{20}$ eV. A selection of recent measurements of the energy spectrum beyond $10^{12}$ eV is shown in Fig. 2.1. The differential flux generally follows a power-law $^{dN}/_{dE} \propto E^{\gamma}$. For the representation in Fig. 2.1, the measured flux has been scaled by $E^{2.5}$ to reveal three distinct breaks in the power-law: At $\sim 3 \times 10^{15}$ eV, the spectral index changes from $-2.7$ to $-3.1$—a feature which is known as the *knee*. Around $5 \times 10^{18}$ eV, the energy region of the *ankle*, a hardening of the spectrum is observed. Furthermore, at energies greater than $\sim 5 \times 10^{19}$ eV the flux is significantly *suppressed*.

The overall power-law behaviour of the energy spectrum of cosmic rays is an indication for a non-thermal acceleration process [2]. Currently, the favoured model for the acceleration of cosmic rays is diffusive shock acceleration at strong collissionless shock waves. In particular, cosmic rays with energies up to the knee are thought to originate from the Galactic interstellar material which is accelerated at the shock fronts generated in remnants of supernovae (see Ref. [10] for a recent review). In this scenario, spectral features due to the acceleration process—for example a cut-off at the maximum reachable energy—would be shifted by the magnetic rigidity $\propto {}^{E}/_{Z}$ of the individual elements constituting the cosmic rays. This is, in fact, consistent with observations indicating a trend from light primaries dominating the cosmic ray flux at the knee to heavier primaries up to $\sim 10^{17}$ eV (see, for example, Ref. [11]). However, other models for the knee exist, such as the rigidity-dependent leakage from the Galaxy (see Ref. [12] for a review). At higher energies, the situation is less clear, mostly due to inconclusive measurements of the energy-dependent mass composition and the lack of statistics at ultra-high energies ($\gtrsim 10^{18}$ eV). The ankle can be interpreted as the transition from Galactic to extra-galactic cosmic rays with a lower flux but harder spectrum than the Galactic component [10]. However, for a proton dominated composition at energies $\gtrsim 10^{18}$ eV, an ankle-like feature

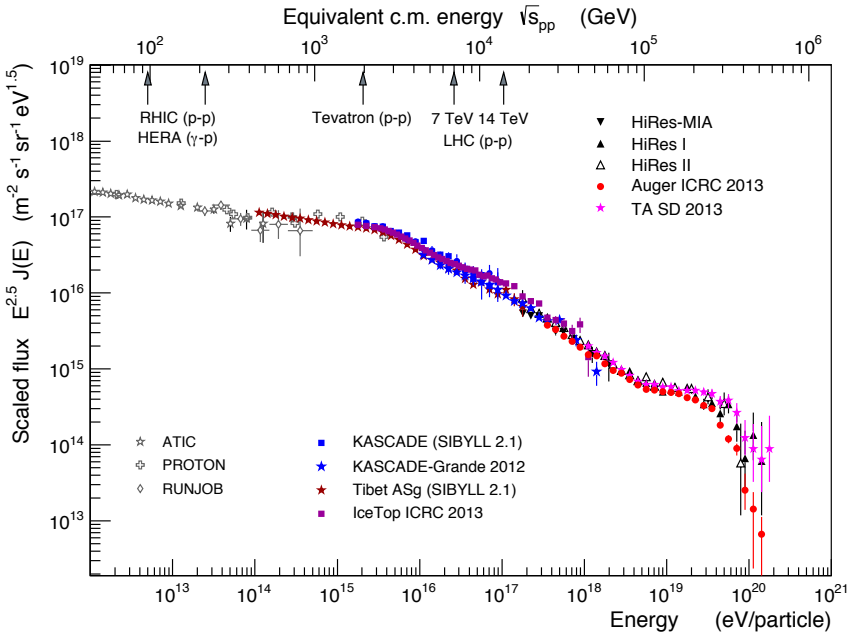


FIG. 2.1 • Measurements of the energy spectrum of the all-particle flux of cosmic rays with energies greater than $10^{12}$ eV. The flux has been scaled by $E^{2.5}$ to reveal deviations from the overall power-law behaviour. The equivalent centre of mass energy assuming protons as cosmic ray particles is shown in the upper scale. From [1] with updated data from [5–8].

would be expected solely from propagation losses: in interactions with the cosmic microwave background (CMB), protons of extra-galactic origin would form $e^+e^-$ pairs, leading to a *dip* in the energy spectrum [13, 14]. Similarly, the interpretation of the flux suppression observed around $\sim 5 \times 10^{19}$ eV is ambiguous: for cosmic rays of extra-galactic origin, a flux suppression is expected at the highest energies for both protons (photo-pion production with the CMB photons which also yields a substantial flux of high-energy photons [15] and neutrinos [16]) and nuclei (photo-disintegration on CMB and IR to UV photons), collectively called the GZK effect after Greisen, Zatsepin, and Kuzmin [16, 17]. However, the rapid decrease of the flux could also be attributed to a maximum accelerator energy close to the GZK cutoff, which seems plausible for many of the known astrophysical accelerators (see Ref. [3] for a review). Similarly to observations at the knee, a detailed study of the energy-dependent mass composition and of the shape of the flux suppression with large statistics would give important hints to distinguish the models. Furthermore, the observation of high-energy *cosmogenic* photons and neutrinos would prove that the composition of cosmic rays at ultra-high energies is dominantly light. So far, no candidates for such secondary particles have been found.

Resolving the ambiguities in the interpretation of the origin and acceleration mechanisms of cosmic rays of the highest energies requires precise measurements of the differential flux and the energy-dependent mass composition of cosmic rays. Up to energies of $\sim 10^{14}$ eV, the chemical composition of cosmic

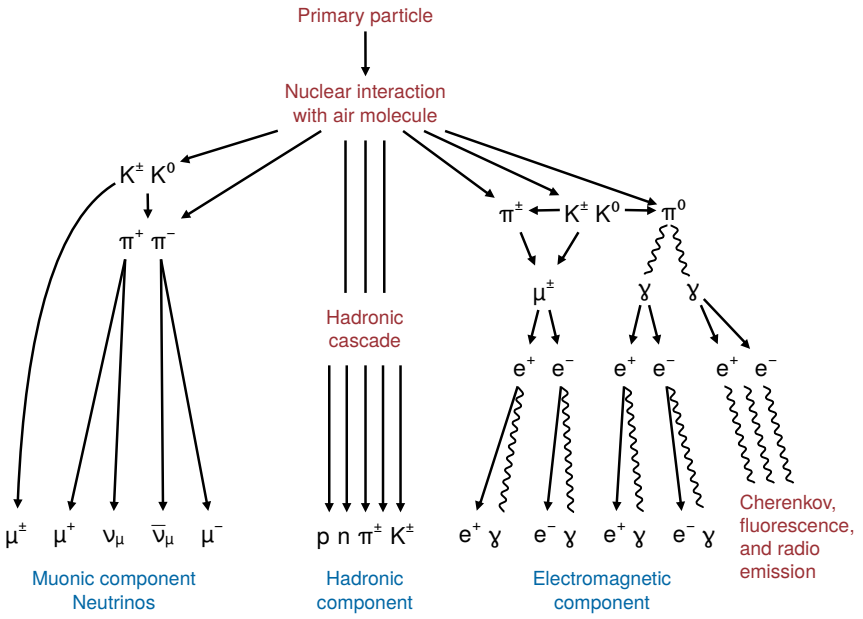


FIG. 2.2 • Development and components of a hadron-induced extensive air shower. The secondary particles are grouped into three components: the hadronic core, the muonic component, and the electromagnetic component. For the measurement of extensive air showers, several observation channels are used: direct detection of the particles of one or more of the components at ground, optical detection of the fluorescence of atmospheric nitrogen or Cherenkov light of the relativistic charged particles, and detection of the radio emission of the charged particles (see text for details). After [18].

rays has been measured by direct observations with balloon-borne or satellite experiments. However, due to the low flux at higher energies, detectors with much larger exposures are required. Therefore, cosmic rays with energies $\gtrsim 10^{14}$ eV are measured indirectly by employing the Earth's atmosphere as a calorimeter and observing the generated *extensive air showers*.

## 2.2 EXTENSIVE AIR SHOWERS

Extensive air showers are particle showers resulting from interactions of cosmic rays with the nuclei in the Earth's atmosphere. The first interaction typically takes place at heights of 15 km to 30 km [1] and produces secondary particles of various types (see Fig. 2.2). An extensive air shower is composed of hadronic, electromagnetic, and muonic components. The most frequently produced hadrons are neutral and charged pions. Due to the short lifetime of neutral pions ($c\tau$ = 25 nm), they decay into two photons without further interactions. Through this process, most of the energy of an air shower is transferred to electromagnetic subshowers, which then dissipate their energy mostly due to the ionisation of air, leaving a trail of a tenuous plasma. The long-lived charged pions ($c\tau$ = 7.8 m) form the bulk of the hadronic subshower together with baryons and, to a lesser extent, kaons. While the high-energy $\pi^{\pm}$ ($\gtrsim$ 30 GeV) reinteract with the atmospheric nuclei, the low-energy $\pi^{\pm}$ decay mostly into muons (and corresponding muon-neutrinos) and feed the muonic subshower.

Since extensive air showers are the products of a multitude of statistical interactions, their properties are best analysed by employing detailed Monte Carlo simulations, e. g. FLUKA [19] or EGS [20] for electromagnetic showers and CORSIKA [21] or AIRES [22] for hadronic showers. The required cross-sections for particle production at energies exceeding the range of accelerator measurements are extrapolated with various hadronic interaction models—e. g. QGSJet [23] or SIBYLL [24]—with significant systematic uncertainties (see Ref. [1] for a recent review). The energy and mass of the primary cosmic ray are then obtained by comparing the measurements with the results of air shower simulations. The energy estimation is, in general, possible with small systematic uncertainties. However, the mass of charged cosmic rays is the most challenging parameter to reconstruct due to strong dependence of the simulated reference showers on the hadronic interaction models (see Ref. [4] for a recent review). Currently, the most reliable estimate of the primary mass is obtained by observing the depth of the shower maximum, $X_{max}$, which is approximately inversely proportional to the mass of the primary particle.[a] Further information can be obtained by analysing the muonic and electromagnetic shower sizes, $N_\mu$ and $N_e$, respectively.

[a] *Typical $X_{max}$ values at $10^{17}$ eV are 570 g cm$^{-2}$ for iron primaries and 680 g cm$^{-2}$ for proton primaries.*

## 2.3 OBSERVATION TECHNIQUES

In the following, an overview of the well-established techniques for the observation of extensive air showers is given, focusing on the advantages and disadvantages of the different methods.

### *Particle detection*

The traditional method for detecting extensive air showers is the sampling of the secondary particle densities on ground using large, sparse arrays of particle detectors, typically scintillators or water-Cherenkov counters. The arrival direction of the cosmic ray is reconstructed from the relative arrival times of the particles in the different detectors. The energy of the primary particle is obtained from the integrated particle count. The mass of the primary particle can be estimated from the ratio of the detected muon and electron numbers. However, this requires a separation of the two components. This, together with shower-to-shower fluctuations and uncertainties in the hadronic cross-sections results in relatively large overall uncertainties. On the other hand, particle detectors have the advantage of a nearly 100 % duty cycle that cannot be reached by optical methods.

### *Optical detection*

Two light production processes are exploited for the observation of extensive air showers in the medium and near UV bands: the isotropic fluorescence emission of atmospheric nitrogen after being excited by charged particles and the Cherenkov emission in the forward direction by the relativistic charged particles in the shower front. Compared to the detection of shower particles at one observation level, optical observations have the distinct advantage that

the shower development can be observed as a function of atmospheric depth. However, the main disadvantage of optical observations is the low duty cycle of about 10 % to 15 %: due to the faint signals and the strong dependence of the light propagation on atmospheric conditions, optical observations are limited to dark nights—about one week before and after new moon—with clear atmospheric conditions.

Fluorescence light is the spontaneous de-excitation radiation from the atmospheric nitrogen molecules after being excited by the passage of charged particles. Since fluorescence light is emitted isotropically, a single fluorescence telescope can be used to observe a large volume of air. The intensity of fluorescence light is proportional to the energy deposit in the atmosphere due to the air shower, the *calorimetric energy*. The proportionality factor, the *fluorescence yield*, has been measured in laboratory experiments and is used to determine the calorimetric energy from the integrated light profile. The energy of the primary particle is then obtained by accounting for the small fraction of invisible energy due to hadrons, muons, and neutrinos which do not deposit all of their energy in the atmosphere. Using fluorescence detectors, the depth of the shower maximum can be observed directly, yielding a very good estimator for the mass of the primary particle.

Most of the Cherenkov light emitted by an air shower is contributed by the relativistic electrons since they are the most abundant charged particles and, at the same time, have a relatively low Cherenkov threshold (~ 21 MeV at sea level). Due to the forward-pointed emission of Cherenkov photons—the Cherenkov angle is about 1.3° at sea level—, only a small ellipsoidal area with a typical diameter of a few hundred metres is illuminated on ground. A notable feature of the lateral light distribution is a prominent shoulder at a distance of 120 m to the shower core [25], beyond which the light distribution steepens. Two types of Cherenkov light detectors are currently employed with different scientific goals.

Non-imaging detectors sample the light distribution on ground, for example, with an array of photomultiplier tubes (PMTs) like the TUNKA [26] experiment in Siberia. The energy and mass of the primary particle are estimated from the photon density (which is strongly correlated with the energy of the shower) and the shape of the lateral light distribution (which depends on the distance to the main emission region and thus $X_{max}$). Due to the limited size of the Cherenkov footprint and the limited duty cycle, a dense array of light detectors is required. Hence, cost constraints limit the applicability of this observation technique to the energy range of $\sim 10^{16}$ eV to $10^{18}$ eV.

Imaging Cherenkov detectors are large telescopes studying TeV $\gamma$-rays for astronomical purposes. An air shower produces a focal plane image which allows the reconstruction of the arrival direction based purely on geometrical considerations. The shape of the image and the determination of the shower size as a function of atmospheric depth is used to suppress the much more abundant hadronic showers. Naturally, stereoscopic observations as employed in the H.E.S.S. experiment [27] are beneficial for the reconstruction.

*Radio detection*

Pioneering studies in the 1960s have shown that extensive air showers produce coherent electromagnetic pulses [28] (see Ref. [29] for a comprehensive review). At that time, the frequency range from several MHz up to 520 MHz [30] has been studied with the conclusion that the emission spectrum is a steeply falling function of the frequency [31]. This is related to the fact that coherent emission from the high-energy particles in the shower disc is only expected for wavelengths larger than ~ 1 m, the typical thickness of the disc. The feasibility of the radio detection of extensive air showers with advanced, digital electronics [32, 33] has lead to increased interest in this detection method in recent years.

It is now understood that the radiation arises mainly from the separation of the particles of opposite charge in the geomagnetic field and the resulting induction of a transverse current [34].[b] Hence, the electric field is polarised transverse to the shower propagation direction and the geomagnetic field vector. Furthermore, the emission strength strongly depends on the angle between the particle trajectories and the geomagnetic field, the geomagnetic angle $\alpha$, specifically $|\mathbf{E}| \propto |\sin \alpha|$. An additional component to the geomagnetic radiation is provided by the variation of the net charge excess, the Askaryan effect [36]. This component is polarised in radial direction towards the shower core. Therefore, interference effects with the geomagnetic radiation are expected. The resulting radio emission due to these processes is coherent up to frequencies of a few hundred MHz, i. e. the electric field strength scales linearly with the number of particles (thus allowing a calorimetric measurement of the shower energy). Furthermore, a number of observables are expected to correlate with the mass of the primary particle, namely the spectral slope [37], the shape of the wavefront [38], and the slope of the lateral distribution of the amplitude of the electric field [39, 40].

[b] *See Ref. [35] for a recent discussion in the context of simulations.*

Contemporary digital radio detectors [32, 33, 41–44] operate at frequencies below 100 MHz to exploit the coherence effects. Typically, an array of low-gain wire antennas measuring at least two polarisation components is deployed. A notable exception is the LOPES-3D [45] configuration, in which tripole antennas are used to achieve an unambiguous reconstruction of all three polarisation components, increasing the sensitivity to inclined showers.

The radio detection of extensive air showers seems to provide a promising combination of mass-sensitivity with a duty cycle which is, in principle, nearly 100 %. However, a cosmic ray detector solely composed of radio antennas, presently, seems to be a challenging endeavour for a number of reasons. First, a self-triggering, large-scale radio array has not been achieved yet. The noise background in the MHz range is very high due to Galactic noise and man-made sources, and the detector bandwidth has to be restricted to several tens of MHz to avoid the densely packed radio broadcast and communication bands. Therefore, pulses due to radio frequency interference (RFI) are indistinguishable from the bandwidth-limited pulses of air showers. Second, since the emission is forward pointed and strongly dependent on the geomagnetic angle, a calculation of the exposure and, hence, the calculation of the cosmic ray flux is subject to significant uncertainties. Third, due to the limited angular range of

the emission, the spacing of the antennas cannot exceed a few hundred metres, limiting this detection method to energies below $\sim 10^{19}$ eV.

*Hybrid detectors*

By combining two or more of the presented detection techniques, many of the disadvantages and systematic uncertainties of the individual methods can be reduced. The two largest air shower detectors, the Pierre Auger Observatory in Argentina [46] and the Telescope Array in the U.S.A. [47], are hybrid experiments of particle detector arrays which are overlooked by fluorescence telescopes. Extensive air showers observed with both detectors are used to calibrate the energy scale of the particle detector array with the nearly model-independent energy determination of the fluorescence detectors. Similarly, the applicability of the radio detection of extensive air showers at ultra-high energies is being studied with a radio extension of the Pierre Auger Observatory [42].

## 2.4 MICROWAVE DETECTION OF EXTENSIVE AIR SHOWERS

In 2008, Gorham and colleagues [48] pointed out that an additional component to the radio emission of extensive air showers could be provided by the ionisation plasma induced by the passage of the high-energy particles of the shower front through the atmosphere. The radiation would be the result of molecular bremsstrahlung: free-free interactions of the plasma electrons with neutral atmospheric molecules.[c] In a test beam experiment at the Stanford linear accelerator center (SLAC), radiation consistent with the hypothesis of molecular bremsstrahlung was observed. An electromagnetic shower was initiated in a 1 $m^3$ anechoic chamber by bunches of $1.2 \times 10^7$ electrons at 28 GeV ($3.36 \times 10^{17}$ eV equivalent shower energy). An LPDA antenna (1 GHz to 8 GHz frequency range) was mounted inside the chamber transverse to the beam direction and cross-polarised to the expected transition and Cherenkov radiation. An exponentially decaying signal attributed to the thermalisation of the free electrons in the shower plasma was observed. Rescaled to the plasma produced by an air shower of energy $E_0 = 3.36 \times 10^{17}$ eV, a spectral energy flux of

$$I_{MBR} = 2.77 \times 10^{-24}\ \mathrm{W\,m^{-2}\,Hz^{-1}} \tag{2–1}$$

was derived for an observation distance of 10 km. It was argued that showers with energies $\gtrsim 8 \times 10^{18}$ eV should be detectable at this distance with standard satellite receiver technology assuming linear scaling of the intensity with the shower energy. Furthermore, indications of non-linear, possibly coherent amplification effects were observed, which could lead to a quadratic scaling of the emitted microwave power with the shower energy.

Together with the results of the beam test experiment also a first search for microwave signals of extensive air showers was published. The prototype detector, AMBER [48], consisted of a 1.8 m parabolic reflector mounted on the rooftop of a building at the University of Hawaii at Mānoa. The reflector was equipped with a four-pixel camera of dual-band (C and $K_u$) and dual-polarised feed horns which were aligned to observe the sky at an elevation of 30°. AMBER

[c] *The mechanism and properties of molecular bremsstrahlung are discussed in detail in Ref. [49].*

was operated in self-trigger mode, with each receiver configured to trigger individually at a constant rate. The data of eight months of stable operation was analysed for air shower-like timing signatures and was found to be inconclusive. It was realised that an existing air shower detector would be required to validate event candidates.

Following the publication of Gorham and colleagues, a number of complementary efforts for the search and characterisation of the microwave emission of air showers were started. In addition, an upgraded variant of the AMBER telescope was installed at the Pierre Auger Observatory and has been taking data in coincidence with the surface detector array since June 2011, overlooking part of the surface detector array similar to the fluorescence telescopes [50].

In the following, a short overview of the projects to measure GHz signals and their state at the time of writing is given. All current experiments operate either in the extended C band (3.4 GHz to 4.2 GHz) or $K_u$ band (10.9 GHz to 14.5 GHz) due to the availability of low-cost microwave receivers (see the following chapter for details).

Besides the relocated AMBER detector, two additional microwave detectors are operated at the Pierre Auger Observatory: the MIDAS telescope and the EASIER array. The MIDAS detector [51] was devised as a self-triggering, imaging telescope, similar to AMBER. However, a considerably larger reflector of 4.5 m diameter was equipped with a densely packed 53-pixel camera of C band feed horns. The design of the camera and the triggering scheme are very similar to a fluorescence telescope and optimised for searches of track-like patterns from distant air showers. During a design validation phase at the University of Chicago, no air shower-like signatures were measured. From this, a limit on the isotropic, unpolarised microwave flux was derived: whereas quadratic scaling of the GHz emission at the flux level measured with the original beam test experiment was excluded, the sensitivity and exposure of the system were not sufficient for excluding the linear scaling (see Ref. [52] for details). In September 2012, the MIDAS camera was installed in a 5 $m^2$ reflector at the Pierre Auger Observatory. Similar to AMBER, the telescope overlooks part of the surface detector array and has been taking data since the beginning of 2013 [50].

With the EASIER experiment, a complementary approach to the observation of air showers from the side has been realised. Part of the sparse surface detector array[d] of the Pierre Auger Observatory has been instrumented with low-gain feed horns operating in the C band [50]. In this setup, the infrastructure—power supply, communication, and triggering—is provided by the surface detectors. The horn antennas are oriented vertically upwards and cover a wide field of view of ~ 100°. In April 2011, seven antennas were deployed. The array was extended to 61 antennas one year later. In early 2012, evidence for the observation of a high energy air shower has been reported [53] and since then, two additional event candidates have been observed [50]. However, no conclusion on the underlying emission mechanism could be drawn due to the small sample size [50].

[d] *The surface detectors are distributed on a triangular grid with 1.5 km edge length.*

Apart from the efforts at the Pierre Auger Observatory, two experiments at Japanese universities operating in the $K_u$ band [54] are worth noting. At Osaka City University, two reflector antennas are operated in coincidence with a scintillator array covering about 300 $m^2$ of effective area. Furthermore, at

Konan University in Kobe, a multi-antenna array of twelve reflectors is installed, for which a 1600 $m^2$ scintillator array is foreseen. Both experiments have taken data for several months without concluding evidence for signals from extensive air showers.

In addition to the search for microwave signals of extensive air showers, the microwave radiation of electromagnetic showers is studied with a new generation of beam test experiments. In two experiments—similar to the original experiment at SLAC—electron beams are injected into Faraday chambers and the transverse radiation of the ionised air is measured with broadband microwave antennas. For the AMY experiment at the beam test facility of the LNF laboratory in Frascati, an electron beam at 510 MeV is injected into an anechoic chamber of $2 \times 2 \times 4\,m^3$ volume [55]. The dominant background is due to direct and scattered Cherenkov radiation and further measurements and simulations are required to improve the sensitivity to a possibly incoherent, isotropic component. To avoid the complications related to Cherenkov radiation, the MAYBE experiment operates at the Van de Graaff facility of the Argonne National Laboratory with an electron beam below the Cherenkov threshold [56]. Incoherent, broadband radiation has been observed and preliminary results indicate that the isotropic flux is several orders of magnitude lower than the original estimates. However, the scaling to extensive air showers is still uncertain. Therefore, an experiment at the electron light source (ELS)—a linear accelerator located at the site of Telescope Array injecting an electron beam into the atmosphere [57]—studies the transverse emission of a fully developed electromagnetic air shower [58]. In first measurements, no evidence for a signal has been found.

# 3 BASICS OF MICROWAVE DETECTION

Microwave radiation is usually picked up with antennas and processed in specialised signal chains before detection. In this chapter, the terminology used in the field of antenna theory is presented. The noise background expected in the microwave frequency bands is discussed, and the decision for operating the main detectors of the experiment in the extended C band (3.4 GHz to 4.2 GHz) is motivated. The properties of reflector antennas—typically used for the detection of weak signals at these frequencies—are introduced along with the receiver electronics.

If no specific references are given in the text, the presented material can be found in introductory text books on microwave engineering or antenna theory, e. g. [59, 60].

## 3.1 ANTENNA THEORY

The response of an antenna to an incident electric field $\mathbf{E}_{\mathrm{inc},\omega}$ of frequency $\omega$ is given by the vector effective length $\mathbf{l}_{\mathrm{eff}}$; the voltage measured at the open-circuit antenna terminals being

$$V_{\mathrm{oc}} = \mathbf{l}_{\mathrm{eff}}(\omega, \theta, \phi) \cdot \mathbf{E}_{\mathrm{inc},\omega}. \tag{3–1}$$

The vector effective length generally depends on the frequency $\omega$ and the direction $(\theta, \phi)$ to the source.[a] Additionally, the polarisation of the receiving antenna and the electric field are encoded in vectorial notation. For far-field applications, both the vector effective length and the electric field are two-component vectors, usually defined in an antenna centred spherical coordinate system,

$$\mathbf{l}_{\mathrm{eff}} = l_\theta \, \hat{\mathbf{e}}_\theta + l_\phi \, \hat{\mathbf{e}}_\phi, \tag{3–2}$$

$$\mathbf{E}_{\mathrm{inc}} = E_\theta \, \hat{\mathbf{e}}_\theta + E_\phi \, \hat{\mathbf{e}}_\phi. \tag{3–3}$$

In the general case that the polarisation of the incoming electric field is not perfectly matched to the polarisation of the receiving antenna, only a fraction of the available power will be extracted by the antenna. The fraction of power received by the antenna is given by the polarisation loss factor

$$\mathrm{PLF} = \frac{|\mathbf{l}_{\mathrm{eff}} \cdot \mathbf{E}_{\mathrm{inc}}|^2}{|\mathbf{l}_{\mathrm{eff}}|^2 \, |\mathbf{E}_{\mathrm{inc}}|^2}. \tag{3–4}$$

For a linearly polarised antenna and electric field the polarisation loss factor is reduced to $\cos^2(\sphericalangle(\mathbf{l}_{\mathrm{eff}}, \mathbf{E}_{\mathrm{inc}}))$. For an unpolarised[b] signal, the expectation value $\langle \mathrm{PLF} \rangle = ½$. Similarly, for a circularly polarised wave detected by a linearly polarised antenna, and vice versa, $\langle \mathrm{PLF} \rangle = ½$.

[a] *Both dependencies are dropped in the following when aiding the clarity of presentation.*

[b] *In this work, the terms* unpolarised *and* randomly polarised *are used interchangeably.*

The time-averaged energy flux of an incident transverse electromagnetic wave with peak amplitude $\widehat{\mathbf{E}}_{\text{inc}}$ is given by its Poynting flux

$$S_{\text{inc}} = \frac{1}{2}\frac{|\widehat{\mathbf{E}}_{\text{inc}}|^2}{Z_0}, \tag{3–5}$$

with $Z_0 = \mu_0 c_0 \approx 120\pi\,\Omega$ being the impedance of free space. The power $P_L$ available at the terminals of an antenna is calculated using its effective area $A_{\text{eff}}$,

$$P_L = \text{PLF} \cdot A_{\text{eff}}(\omega, \theta, \phi) \cdot S_{\text{inc}}. \tag{3–6}$$

Similarly to the vector effective length, the effective area depends on the frequency $\omega$ and the direction $(\theta, \phi)$ to the source of the incident wave. Note that the effective area is defined for an incident wave of matched polarisation and the polarisation loss has to be treated separately. However, the radiation efficiency of the antenna, accounting for internal conduction and dielectric loss, is included in $A_{\text{eff}}$.

The effective area is related to the vector effective length via

$$A_{\text{eff}}(\omega, \theta, \phi) = \frac{1}{4}\frac{Z_0}{Z_L}\,|\mathbf{l}_{\text{eff}}(\omega, \theta, \phi)|^2, \tag{3–7}$$

where $Z_L$ is the load impedance.

It is often useful to give the antenna gain G instead of its effective area, related via

$$A_{\text{eff}}(\omega, \theta, \phi) = \frac{\lambda^2}{4\pi}\,G(\omega, \theta, \phi). \tag{3–8}$$

The gain is defined as the ratio of the radiation intensity in a given direction to the radiation intensity obtained with a reference antenna with both antennas accepting the same power at their terminals. Typically, a lossless isotropic radiator is used as reference and the gain is given in units of dBi,

$$G\,[\text{dBi}] = 10\log_{10}(G). \tag{3–9}$$

As for the effective area, the gain is defined for a wave of matched polarisation. When needed, it can be decomposed into two components, e. g. $G = G_\theta + G_\phi$ in spherical coordinates.

Due to conservation of power, the gain of any lossless antenna, integrated over all directions is

$$\iint_{4\pi} \mathrm{d}\Omega\, G(\theta, \phi) = 4\pi. \tag{3–10}$$

It follows that antennas with a high gain in one direction exhibit low gain in other directions, i. e. a narrow field of view. The direction dependent gain of an antenna is commonly called the *radiation pattern*, with typical characteristics being the maximum or boresight gain $G_{\text{max}}$ and the half-power beamwidth $\theta_{3\,\text{dB}}$ (full-width half-maximum of the radiation pattern).

## 3.2 NOISE AND SYSTEM TEMPERATURE

The sensitivity of any detector is related to the amount of undesired background signals—in the case of radio frequency (RF) systems, the noise power in the observed part of the electromagnetic spectrum. In addition to natural and anthropogenic external sources of radiation, each electric component contributes to the overall noise of a detection system. For microwave systems it is often convenient to give the spectral density of the noise power of any noise source in the form of an equivalent noise temperature $T_n(\nu)$ [61]. It is related to the noise power $N$ over the frequency bandwidth $\Delta\nu$ via

$$N = \int_{\Delta\nu} d\nu \, k_B T_n(\nu), \tag{3–11}$$

where $k_B$ is the Boltzmann constant. In case the noise temperature is reasonably flat within the detector bandwidth it is often sufficient to use the average noise temperature $T_n$, for which the expression simplifies to

$$N = k_B T_n \, \Delta\nu. \tag{3–12}$$

Note that the noise temperature is not necessarily connected to the *physical* temperature of the noise source. However, the definition was chosen deliberately: in the Rayleigh-Jeans approximation $h\nu \ll k_B T$—suitable for the typical frequencies and temperatures we are concerned with[c]—a resistor at *physical* temperature $T$ has the same equivalent noise temperature

[c] *See [61] for a review of this topic.*

$$T_n = T. \tag{3–13}$$

The above relation can be derived from similar arguments as the classical derivation of black body radiation, although in one dimension [62]. In fact, the same relation holds for the noise power transferred to a matched load by an antenna observing a black body radiator [63]. To illustrate this, consider a lossless antenna mounted in a cavity which is lined with black body radiators, e. g. microwave absorbers. The spectral energy density of the unpolarised electromagnetic field at frequency $\nu$ in the cavity is

$$E_\gamma \frac{dN_\gamma}{dV\, d\nu} = \frac{8\pi\nu^2}{c^3} k_B T. \qquad \text{(Rayleigh-Jeans law)} \tag{3–14}$$

Since the black body radiation is isotropic, the spectral energy flux in the cavity is related to the energy density via

$$E_\gamma \frac{dN_\gamma}{dA\, d\Omega\, d\nu\, dt} = \frac{c}{4\pi} \cdot E_\gamma \frac{dN_\gamma}{dV\, d\nu} = \frac{2 k_B T}{\lambda^2}. \tag{3–15}$$

Employing Eqs. (3–6), (3–8), and (3–10) from antenna theory, the power detected by the antenna in the bandwidth $\Delta\nu$ and transferred to its load becomes (including a polarisation loss factor of ½)

$$P_L = \frac{1}{2}\int_{\Delta\nu} d\nu \iint_{4\pi} d\Omega\, A_{\text{eff}}(\theta,\phi)\,\frac{2k_B T}{\lambda^2} \tag{3–16}$$

$$= \frac{1}{2}\int_{\Delta\nu} d\nu \iint_{4\pi} d\Omega\,\frac{\lambda^2}{4\pi}\,G(\theta,\phi)\,\frac{2k_B T}{\lambda^2} \tag{3–17}$$

$$= k_B T \Delta\nu. \tag{3–18}$$

An antenna observing a black body therefore produces the same spectral noise power as a resistor at temperature T. In radio astronomy, the term *antenna temperature* $T_A$ is commonly used for the equivalent noise temperature of the spectral output power of an antenna at a given frequency.

The total noise temperature of a detection chain, commonly called the system temperature $T_{sys}$, includes the external contribution $T_A$ and the noise contributions from every component in the detector. A detection chain is typically a cascaded network of amplifiers and filters. The system temperature is then the sum of the noise temperatures $T_i$ of the individual components[d] weighted by the inverse gains $G_i^{-1}$ of all previous components in the cascade,

[d] *The noise temperature is typically referenced to the input of a component.*

$$T_{sys} = T_A + T_1 + \frac{T_2}{G_1} + \frac{T_3}{G_1 G_2} + \dots. \tag{3–19}$$

Therefore, the first stage of a detection system should ideally be a low-noise amplifier with a relatively large gain $G_1$, so that the noise contributions of all subsequent components are negligible.

## 3.3 ATMOSPHERIC ATTENUATION AND NOISE BACKGROUND

The extended C band ranging from 3.4 GHz to 4.2 GHz was selected as the main operating range for the detectors of the CROME experiment. This band is particularly attractive for several reasons:

- LOW NATURAL BACKGROUND RADIATION. In Fig. 3.1 the frequency spectra of various natural noise sources are shown. For an antenna which is pointing vertically up and operating between about 1 GHz and 10 GHz, the terrestrial microwave window [66], the natural lower noise limit is given by the CMB. Towards lower frequencies, the antenna temperature rises rapidly due to the Galactic synchrotron emission. Radiation of higher frequencies can be absorbed by atmospheric oxygen and water vapour—above about 10 GHz, the noise temperature of a terrestrial antenna is dominated by the emission related to these absorption processes.

- NEGLIGIBLE ABSORPTION IN THE ATMOSPHERE. At microwave frequencies, the main absorption of radiation is due to resonances of water vapour $H_2O$ and molecular oxygen $O_2$. The lowest frequency lines are located at 22 GHz and 50 GHz, respectively [65]. The absorption spectrum for typical

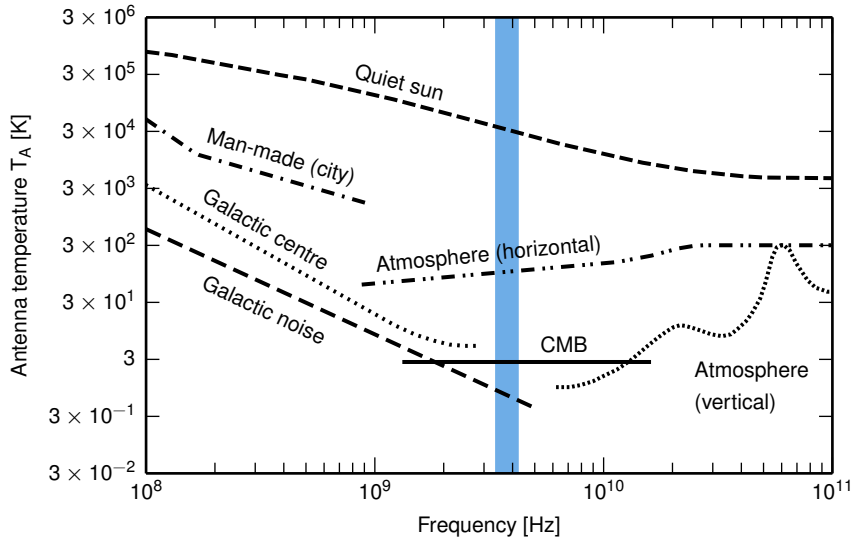


FIG. 3.1 • Effective antenna temperature due to external noise sources (adapted from [64]). The extended C band (3.4 GHz to 4.2 GHz)—marked by the shaded region—is characterised by very low noise from natural sources, particularly in vertical direction.

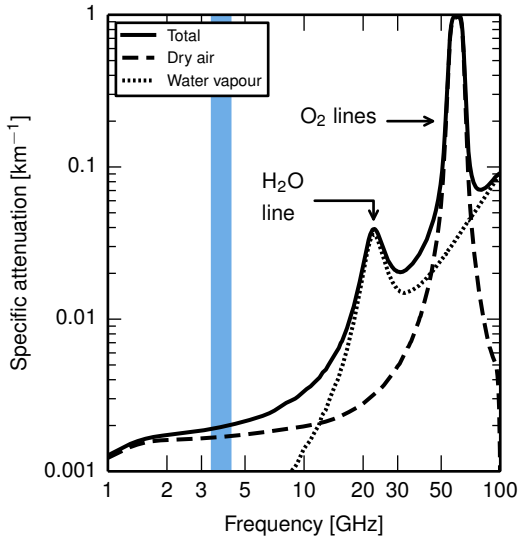


FIG. 3.2 • Specific attenuation of microwave radiation due to atmospheric gases as a function of frequency. Calculated with the Millimeter-wave Propagation Model (MPM93) [65] for an atmosphere at 15 °C with 50 % relative humidity and an atmospheric pressure of 1013 mbar, similar to sea level. In the extended C band, marked by the shaded region, radiation is attenuated by less than 0.2 % per km.

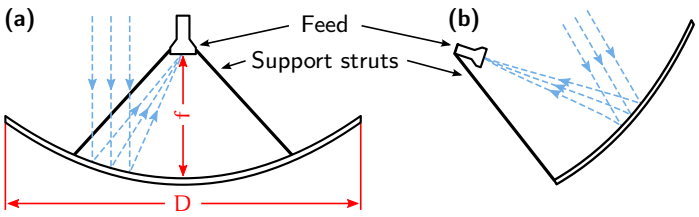


FIG. 3.3 • Types of reflector configurations: **(a)** prime focus, and **(b)** offset-fed parabolic reflectors.

atmospheric conditions at ground level are shown in Fig. 3.2. The specific attenuation is less than 1 % per km below 10 GHz. For example, the radiation of an air shower observed at sea level at a distance of 20 km is attenuated by ~4 % in the C band. In comparison, fluorescence light emitted in the near UV band would be attenuated by ~80 % due to Rayleigh scattering off the air molecules alone [67].[e]

[e] *Additionally, Mie scattering off aerosols leads to further attenuation.*

- LITTLE MAN-MADE INTERFERENCE. Since most parts of the C band are reserved for satellite down-links, it is essentially free of terrestrial RFI. The frequency band also lies far away from common GHz sources such as Wi-Fi access points and clients (2.4 GHz, 5 GHz), or mobile phones (≤ 2.6 GHz in Europe).

- AVAILABILITY OF HIGHLY-OPTIMISED, OFF-THE-SHELF COMPONENTS [48]. Given the low-noise environment, the receiving electronics will give a large contribution to system temperature. Therefore, much effort went into the development of inexpensive, high-performance reception systems, particularly for mass markets such as satellite TV reception. As a result, a typical, modern C band receiver has a (power) gain of about 65 dB, can have a noise temperature as low as 30 K, and is available for less than 100 €. At the same time, the receivers are robust, well-tested, and protected against weather influence, making them ideal detectors for our purposes.

## 3.4 REFLECTOR ANTENNAS

High-gain antennas for microwave frequencies are usually built in the form of parabolic reflectors with matched horn antennas—often called feed horns or simply feeds—mounted in the focal point. Two configurations of parabolic reflectors have been used in the CROME experiment: prime focus and offset-fed reflectors, see Fig. 3.3. In the prime focus design, the reflector is shaped like a truncated paraboloid with a circular rim. Radiation entering perpendicular to the rim is focused coherently at the focal point at distance f above the centre of the reflector surface. Part of the radiation is blocked by the receiver and its support construction. To minimise the loss in aperture, an offset-fed reflector made of an asymmetrical segment of a paraboloid can be used. In this design, the focal point is located on one side of the reflector, outside the radiation zone.

The geometry of prime focus reflectors is defined by the diameter D and the focal length f of the paraboloid.[f] The antenna gain G at wavelength λ can be

[f] *Instead of the focal length, the ratio* $^{f}/_{D}$ *is often given by manufacturers.*

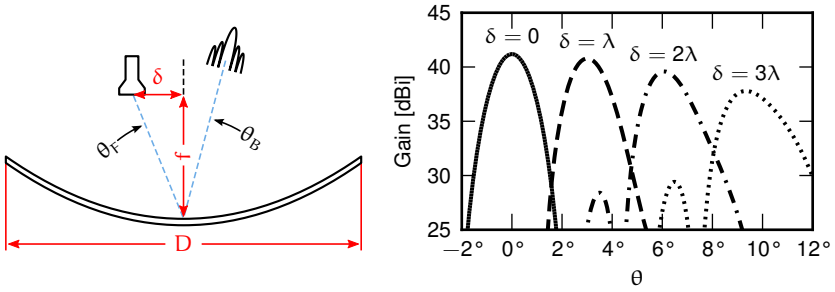


FIG. 3.4 · Illustration of a receiver laterally shifted from the focal point by the distance δ (left panel) and effect of this shift on the radiation pattern (right panel). The radiation patterns were calculated for a parabolic reflector with diameter D = 3.4 m and focal length f = 1.2 m at 3.8 GHz (λ = 8 cm) using the General Reflector Antenna Software Package (GRASP) [71] (see § 5.1.6 for a brief description).

calculated from the geometric area A and the (generally wavelength dependent) antenna efficiency η(λ),

$$G(\lambda) = \eta(\lambda) \cdot A \cdot \frac{4\pi}{\lambda^2} = \eta(\lambda) \cdot \left[\frac{\pi D}{\lambda}\right]^2. \tag{3–20}$$

The antenna efficiency is mainly defined by the radiation pattern of the feed (primary pattern) [68]. Ideally, the primary pattern should be symmetric in the E and H planes and result in a uniformly illuminated reflector surface with no spill over the reflector edge. Both under-illumination of the reflector surface and spillover decrease the efficiency. Spillover also increases the noise of the antenna, as radiation from behind the reflector, e. g. thermal radiation from ground, is picked up. A real primary pattern is always a compromise between all requirements. For circular feed horns with an edge illumination taper of about −10 dB and good-quality reflectors, typical efficiencies range between 50 % and 70 %. For example, the 3.4 m reflectors that are used as C band detectors for CROME have a mid-band gain of ~12,500 (41 dBi), corresponding to an efficiency of about 70 %.

The high gain that can be achieved with a parabolic reflector antenna is directly related to the sharp, pencil-like secondary radiation pattern, called beam in this context. The half-power beamwidth $\theta_{3\,\mathrm{dB}}$, corresponding to the full-width half-maximum field of view, can be estimated [69] with

$$\theta_{3\,\mathrm{dB}} \approx 70° \cdot \frac{\lambda}{D}. \tag{3–21}$$

For the antenna mentioned above, the mainlobe is ~ 1.6° wide in the C band. A cost-effective and simple method to increase the solid angle viewed by a reflector antenna is to mount a matrix of feed horns around the focal point [70]. The lateral defocusing of a feed horn, i. e. moving its phase centre parallel to the reflector plane out of the focal point, is illustrated in Fig. 3.4. When a feed horn is defocused by the scan distance δ, the angle between the reflector axis and the boresight direction is given by

$$\theta_B = \mathrm{BDF} \cdot \arctan\left(\frac{\delta}{f}\right) = \mathrm{BDF} \cdot \theta_F. \tag{3–22}$$

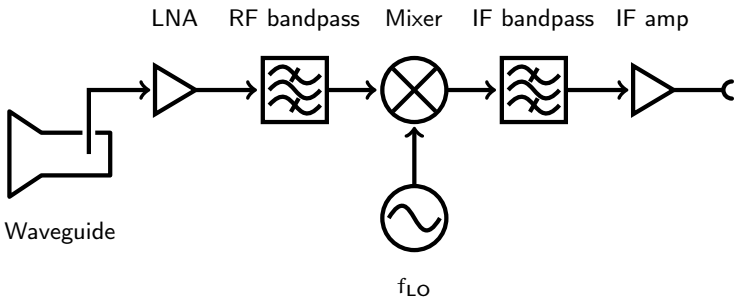


FIG. 3.5 • Block diagram of a low-noise block (LNB). See text for an explanation of the individual components.

The beam deviation factor BDF is typically 0.7 to 0.9, depending on $^f/_D$ and the primary radiation pattern [72].

Increasing the field of view of a parabolic reflector antenna comes at the expense of efficiency: with increasing scan distance, the boresight gain drops, the beam broadens and the height of the first sidelobe (coma lobe) increases. The effects of defocusing on the radiation pattern are shown in the right panel of Fig. 3.4. For a prime focus reflector, the additional aperture blockage due to the camera supporting the feed horns further decreases the boresight gain.

## 3.5 LOW-NOISE BLOCKS (LNBS)

At the time of planning the CROME setup, it was already clear that only very limited time would remain for operating the experiment in coincidence with KASCADE-Grande. Therefore, it was decided to use commercial and readily available components for the microwave detectors. For the C band, low-noise blocks (LNBs), intended for the reception of satellite TV and data services, are used as feeds in parabolic reflectors. LNBs are compact, self-contained receivers perfoming the following tasks:

- detection of the desired polarisation of the incoming radiation and amplification of the RF signal with a low-noise amplifier (LNA),
- filtering for the desired frequency band, and
- down-conversion to a lower frequency band using a stabilised local oscillator (LO) and mixer.

The block diagram of an LNB is shown in Fig. 3.5. The incoming radiation is usually picked up with one (single polarisation) or two perpendicular (dual or circular polarisation) quarter-wavelength antennas mounted in a waveguide. The waveguide is either a reflector-matched feed horn[g] or ends in a standard flange for a separate feed horn. The RF signal is amplified, typically by ~ 20 dB, with an amplifier optimised for low-noise in the detection band and bandpass filtered. By mixing the RF signal with a sinusoid generated by a local oscillator, the RF band is effectively down-converted to a lower frequency band, the intermediate frequency (IF) range.[h] Harmonics and intermodulation products

[g] *The combination of LNB and feed horn is often abbreviated with LNBf.*

[h] *More information on down-conversion is given in appendix § A.1.*

generated by the down-conversion as well as left-overs of the oscillator frequency are removed by a bandpass in the intermediate frequency range. A further amplifier with a gain of > 30 dB is used to counter losses on the following transmission line, which is typically connected with a 75 Ω type F connector.[i]

For C band LNBs the local oscillator frequency is typically $f_{LO} = 5.15\,\text{GHz}$ with a stability of a few hundred kHz—the RF band of 3.4 GHz to 4.2 GHz is thus mirrored and down-converted to 0.95 GHz to 1.75 GHz.

[i] *See § A.2 for a brief explanation of characteristic impedance.*

# 4

# THE CROME SETUP

In this chapter, the hardware setup and data acquisition system of CROME are described. The aims of the experiment and its basic concept are introduced. Since the experiment was embedded in the KASCADE-Grande air shower detector to make use of its triggering and reconstruction facilities, the array is briefly described.

## 4.1 AIMS OF THE EXPERIMENT AND CONCEPT

The aim of the CROME experiment was the search for microwave radiation from extensive air showers. On successful detection, the radiation characteristics, particularly the isotropy of the radiation, were to be studied to conclude whether microwave detection could provide a feasible option for a next generation air shower detector.

The basic idea was to construct high-gain microwave antennas pointing nearly vertically up into the atmosphere above an existing cosmic ray detector, see Fig. 4.1.[a] The readout of the antennas can be triggered by the air shower detector and the existing air shower reconstruction can be used for event selection and studies of the signal properties. However, the key differences to the initial AMBER setup are (a) the external triggering, which allows the selection of shower-related signals and a study of a possible dependence on the geometry, and (b) the field of view: air showers are viewed from the forward direction instead of from the side. This has two main benefits: first, it minimises the distance to the maximum of shower development and therefore the expected main source of radiation. Second, since the antenna is placed in the propagation direction of detected air showers, the emitted microwave energy arrives at the antenna in a short time window. This time compression of the signal leads to a natural increase of the signal-to-noise ratio.

KASCADE-Grande, a detector array for extensive air showers located at the Campus North of the Karlsruhe Institute of Technology, was found to be a well-suited site to build a prototype microwave detector for several reasons.

[a] *Around the same time, a similar concept was devised independently for the EASIER detector at the Pierre Auger Observatory (see § 2.4).*

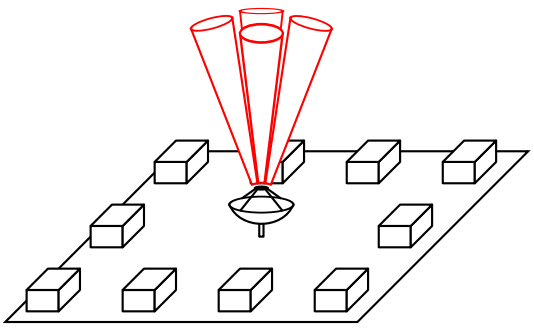

FIG. 4.1 • Schematic of the detector concept. An air shower detector provides a trigger signal for the read-out of a multi-beam reflector antenna. The antenna is located within the array and aligned to view incoming extensive air showers from their forward direction.

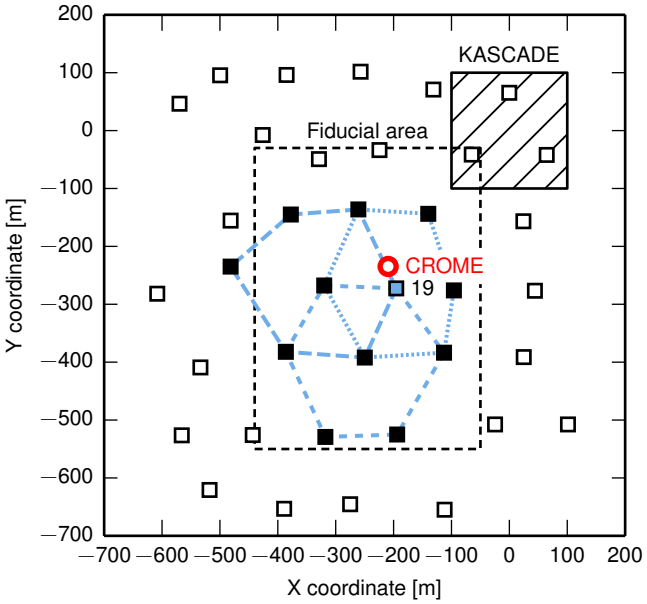


FIG. 4.2 • Location of the CROME antennas within the KASCADE-Grande detector array (KASCADE-Grande coordinate system). The positions of the Grande stations are indicated by squares, with the stations of the three inner hexagons providing the trigger for CROME marked with solid squares. Station 19, which is also used for time synchronisation, is indicated separately. The fiducial area of the Grande reconstruction is shown as dashed rectangle.

For one, KASCADE-Grande covered an energy range of cosmic rays of $10^{16}$ eV to $10^{18}$ eV which includes the equivalent shower energy used in the test beam measurements at SLAC. Also, a short roundtrip time is beneficial for an R&D detector which requires frequent changes and maintenance. Additionally, the local KASCADE-Grande group could provide assistance in supplying the microwave detector with a trigger and on using the shower reconstruction.

## 4.2 KASCADE-GRANDE

The KASCADE-Grande experiment consisted of the dense Karlsruhe Shower Core and Array Detector (KASCADE) scintillator array [73] and the Grande scintillator array [74]. It was operated for about 9 years until November 2012.

The KASCADE array was formed by a total of 252 stations distributed on a 200 m × 200 m area. Each station contained unshielded liquid scintillators for the detection of the electromagnetic shower component. The 192 outer stations were equipped with additional shielded plastic scintillators to allow the independent reconstruction of the muonic component.

The Grande array was made of 37 stations, each containing 10 $m^2$ of plastic scintillator detectors viewed by 16 high-gain and 4 low-gain PMTs to cover a large dynamic range. The stations were arranged on an irregular grid of 137 m average spacing covering an area of 0.5 $km^2$, see Fig. 4.2.

A Grande station produced a trigger logic signal when the combined currents of the high-gain PMTs exceeded a threshold. The logic signal of each station was

sent over 700 m long cables to the coincidence logic contained in the central data acquisition (DAQ). The Grande array was partitioned into 18 overlapping trigger hexagons, each formed by one central and six outer Grande stations. When all stations of any hexagon triggered, the signals of all stations were read out and stored for offline processing.

The arrival direction of a detected air shower is reconstructed by fitting the relative arrival times of the shower particles with a theoretical shower front obtained from CORSIKA [21] simulations [74]. The location of the shower core and the number of charged particles $N_{ch}$ are reconstructed by fitting a lateral distribution function to the measured number of particles. The muon number $N_{\mu}$ is derived from the KASCADE data. The complete reconstruction is implemented in a program called KRETA. Full efficiency of the detector and the reconstruction chain is reached for primary energies above $10^{16}$ eV. The reconstruction procedure and its performance is described in detail in Ref. [74].

In this work, the shower energy is taken from the energy reconstruction with the $N_{ch} - N_{\mu}$ method [75].[b] It is based on a combination of $N_{ch}$ and $N_{\mu}$ and is calibrated using CORSIKA simulations with the QGSJet-II [23] hadronic interaction model.

To obtain a consistent performance of the reconstruction, quality cuts are applied to the data [77].[c] This includes rejecting showers with reconstructed core positions outside the fiducial area shown in Fig. 4.2. Applying all quality cuts, the reconstruction accuracy is 0.8° for the arrival direction and 6 m for the core position [74]. The primary energy is estimated with an uncertainty of $\leq 20\,\%$ for heavy primaries with energies above $10^{16.5}$ eV.

[b] *See [76] for a comparison with other methods used by the KASCADE-Grande collaboration.*

[c] *The quality cuts are described in detail in the context of the event selection (§ 6.1).*

## 4.3 EXPERIMENT OVERVIEW

For the electronics and DAQ of the CROME experiment, space in a container previously used for the DAQ of the Piccolo trigger array [74] was provided. The DAQ container is located near the centre of the Grande array and an empty area next to it was found to provide sufficient space for the installation of microwave detectors. The position within the array is marked in Fig. 4.2.

The experimental efforts began in June 2010 with setting up a single off-the-shelf antenna manufactured for the reception of satellite TV, see Fig. 4.3. By November 2012, the time KASCADE-Grande was shutdown, the experiment had evolved into a radio antenna array covering multiple frequency bands from several kHz to more than 10 GHz, see Fig. 4.4. The work presented in this thesis is focused on the antennas operated in the extended C band (3.4 GHz to 4.2 GHz). The experimental efforts surrounding the L band detectors are documented in Refs. [78–81]. A preliminary analysis of the data collected with the VLF antenna is presented in Ref. [82].

A few weeks after the installation of the first $K_u$ band antenna at the CROME site in June 2010, a 150 cm offset-fed reflector (Gibertini OP150 S) with a three-feed holder was set up, see Fig. 4.5. While another $K_u$ band feed (Smart TSX 11) was installed in the focal point, two C band feeds (Panorama ER861) were mounted on the outer positions. This prototype setup was mainly used to gain

FIG. 4.3 • Photograph of the CROME experiment in its initial phase (June 2010). The first antenna, a 90 cm reflector operated in the lower $K_u$ band (10.7 GHz to 11.7 GHz), is visible in front of the DAQ container. The container on the left, part of the Piccolo trigger cluster, was removed later.

FIG. 4.4 • Photograph of the CROME experiment in one of its last configurations (May 2012). The three largest antennas, 3.4 m reflectors, are operated in the extended C band (3.4 GHz to 4.2 GHz) and are the leading instruments of the experiment. On the left, a VHF LPDA antenna (30 MHz to 80 MHz) that was reused from the LOPES* experiment is visible, three others were distributed around the area. Two smaller reflectors, one in the background (black), one on the right hand side (metallic), were used for measurements in the L band (1 GHz to 2 GHz). A VLF antenna (~ 100 kHz to several MHz) was mounted on the long pole seen on the far right.

FIG. 4.5 • Offset-fed 150 cm reflector with one central $K_u$ band feed and two outer C band feeds (foreground), and 90 cm reflector with two $K_u$ band feeds (background).

FIG. 4.6 • Prime focus 3.4 m reflector with custom-made four feed C band camera. The two reflectors shown in Fig. 4.5 are visible in the background.

FIG. 4.7 • Close up of one of the nine feed cameras mounted in the 3.4 m reflectors. The final configuration is shown, in which the four corner feed horns are equipped with *two* LNBs for dual-polarised measurements.

experience with the installation and operation of a microwave detector and investigate the RF background.

After preliminary analyses revealed no obvious signal candidates, we decided to switch to a prime focus reflector with higher gain, increasing the sensitivity and at the same time allowing the installation of a larger camera with more feed horns to increase the field of view. A 3.4 m reflector (Prodelin 1344, $^{f}/_{D} = 0.35$)[d] was installed in September 2010, see Fig. 4.6. A custom-made camera supporting four receivers was mounted, centred at the focal point. The receivers consisted of Norsat 8215F LNBs mounted on reflector-matched feed horns provided by Prodelin.

[d] *A detailed description of the reflector is given in § 5.1.6.*

The field of view covered by the four beams was approximately 6°×6°, centred in zenith direction, with half-power beamwidths of ~ 1.6°. To increase the field of view, a final, larger camera supporting a 3 × 3 receiver matrix has been installed since November 2011, see Fig. 4.7. The central feed is mounted in the focal point for maximum gain and the total field of view is about 10° × 10°. More details on the radiation patterns are given in § 5.1.6.

To further increase the region of the sky covered with CROME detectors, two additional antennas identical in construction have been installed. The second 3.4 m reflector has been installed in April 2011 and was first aligned similarly to the first 3.4 m reflector, pointing vertically, but rotated to cover the gaps of the field of view of the first 3.4 m reflector. In October 2011 it was tilted 15° towards magnetic north to cover a separate region of the sky and to study a possible dependence of the event rate on the geomagnetic field direction. In the beginning of 2012, the first microwave signals correlated with air shower events were discovered. To increase statistics during the limited lifetime of

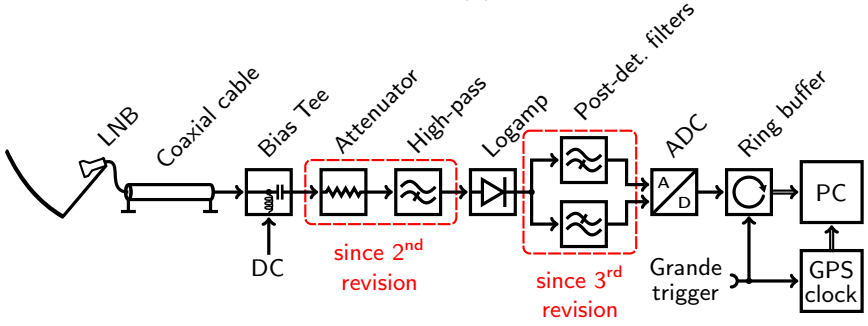


FIG. 4.8 • Block diagram of the detection electronics. A microwave detector, an LNB mounted in a parabolic reflector, is supplied with power using a Bias Tee. The microwave signal is attenuated to reduce reflections and filtered to remove the background generated by aircraft altimeter radars (2nd revision). The waveforms are demodulated by a logarithmic amplifier (logamp) and distributed to two channels: a fast envelope for the detection of transients, and a slow envelope for determining the noise background (3rd revision). The output voltage is continuously sampled with a USB oscilloscope (ADC and ring buffer). The voltage trace and a GPS-derived event timestamp are read-out and stored for offline processing when a high-energy air shower is detected by KASCADE-Grande.

KASCADE-Grande, a third 3.4 m reflector was installed in April 2012 with its field of view tilted 15° from the vertical towards magnetic south.

The C band receivers mounted in the cameras are linearly polarised and arranged in a checkerboard pattern. However, a second polarisation port is available at each feed horn. After realising that the detected signals are at least partially polarised, starting in February 2012 the corner feed horns of each camera were gradually equipped with additional LNBs, effectively adding a second polarisation to four of the nine beams of each antenna. A close up of this configuration is shown in Fig. 4.7.

## 4.4 DATA ACQUISITION HARDWARE

### *Detection electronics*

The IF waveforms of the LNBs are processed with an electronics chain, designed by O. Krömer (IPE/KIT), and subsequently sampled with USB oscilloscopes. A block diagram of the electronics chain is shown in Fig. 4.8 (the different revisions shown in the block diagram are discussed below). The transmission line, 75 Ω coaxial cable (Kathrein LCD95 or Kathrein LCD111), is typically 30 m to 50 m long. The electronics chain is based on components with 50 Ω impedance (nominal). Hence, an impedance mismatch occurs at the interface to the transmission line.[e] The resulting reflections are attenuated by the coaxial cables to a negligible level.[f] The transmission line is biased with a DC voltage using a Bias Tee (Mini-Circuits ZFBT-352-FT+) to supply power to the active electronics of an LNB. Since the bandwidth of the RF signal is too high to be sampled with standard oscilloscopes, the signal is demodulated prior to sampling with a demodulating logarithmic amplifier (Mini-Circuits ZX47-60-S+ logamp). The logamp converts the wideband RF signal to a voltage approximately proportional to the logarithm of the RF power.[g] In the default configuration, the output voltage is lowpass filtered to 6 MHz video bandwidth which corresponds to an exponential rise time of ~ 30 ns. The output signal of the logamp is then

[e] *See § A.2 for a short review of characteristic impedance and reflections.*

[f] *A minimum length of ~20 m is required.*

[g] *See § 5.1.3 for a detailed explanation.*

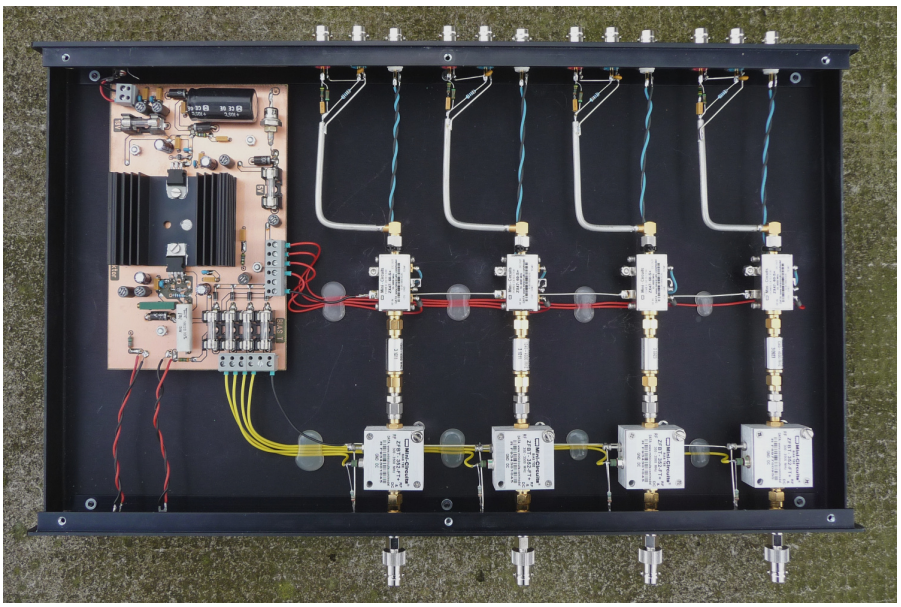

FIG. 4.9 • Photograph of the final revision of the electronics chain. Four channels are contained in one aluminium box and supplied by a common power supply (left). Each channel consists of (bottom to top) a Bias Tee, 6 dB attenuator, high-pass filter, logarithmic amplifier, and three output ports (left to right: fast envelope, slow envelope, temperature sensor).

digitised using a Pico Technology PicoScope 6402 or 6403 USB oscilloscope with 8 bit vertical resolution and 350 MHz analogue bandwidth.

The RF components of four electronics chains are mounted in one aluminium box, see Fig. 4.9 for a photograph, and powered with an 18 V switching power supply. The input voltage is filtered and distributed to the Bias Tees via an adjustable voltage divider and to the logarithmic amplifiers through a 5 V linear regulator. Throughout the first year of the experiment, the electronics chain was revised several times. For a short period between October 2010 and January 2011, external DC reduction filters were used to reduce the voltage range of the video signal and hence increase the resolution of the sampled traces. Similar filters were permanently installed in the electronics chains starting December 2010. Since then, each electronics chain provided two outputs: the slow envelope, a low-pass filtered channel for the precise measurement of the average power, and the fast envelope, a high-pass filtered channel for the measurement of transients (as expected from signals of air showers). Details on these filters are given in § 5.1.2.

In the first months of operation, the dominant sources of transient background in the C band channels were altimeter radars from aircrafts passing through the fields of view of the receivers, see § 5.3. The radars operate at ~ 4.3 GHz and can, therefore, be suppressed using a high-pass filter in the IF range. In December 2010, such filters (Mini-Circuits VHF-1200) were installed at the inputs of the logarithmic amplifiers along with additional 6 dB attenuators (Radiall R411806124) to suppress reflections.

In April 2011, the video bandwidth of the logarithmic amplifiers was increased from ~ 6 MHz to ~ 60 MHz to improve the sensitivity to very short RF pulses, see § 5.1.3 for details.

*Triggering and timing*

The CROME DAQ was triggered by high-energy Grande showers using a logical `AND` combination of the logic signals of the 12 stations forming the three inner Grande hexagons (filled squares in Fig. 4.2). The trigger signal was distributed to the individual oscilloscopes and an additional Meinberg GPS167LCD-MP GPS clock. The GPS-derived timestamps are used to match the digitised voltage traces to the events of KASCADE-Grande for offline analyses.[h]

[h] *The timestamps of KASCADE-Grande events are generated by the same type of clock.*

Given that a GHz signal from an air shower emitted in forward direction can be as short as a few ns, a reliable determination of the time offset between the Grande and CROME DAQs was very important. To reduce the uncertainty in estimating the time window in which a microwave signal would be expected, we decided to additionally digitise the trigger signal of a single Grande particle detector with the CROME DAQ. In November 2010, the logic signal of the Grande station nearest to the CROME antennas, station 19, was connected to one of the CROME digitisers. For this, the same type and length of cable was used as for connecting the station to the Grande DAQ. Accounting for cable and electronics delays, the arrival time of the shower particles in the station can be calculated directly in the time frame of the CROME DAQ.[i]

[i] *This is shown in detail in § 6.1.2.*

## 4.5 MONITORING AND DATA TAKING SOFTWARE

*PicoScope DAQ software*

The first few months of the experiment, the graphical oscilloscope software supplied by the vendor for the Microsoft Windows platform, was used for the readout and storage of voltage traces. However, several limitations of the software made a longterm use unfeasible. First, events were held in memory and therefore traces were lost when the operating system halted or rebooted. Furthermore, the software imposed an artificial limit of about 1000 events for one data run. A run had to be stopped manually before reaching the limit to avoid losing events. Second, events were stored without an identifying timestamp. The voltage traces could only be associated with KASCADE-Grande events unambiguously if the number of events captured by a PicoScope was equal to the number of triggers that had been sent. However, this was not always the case, one reason being the long acquisition dead time of $\mathcal{O}$ (100 ms). A few triggers were lost each week and the corresponding data runs had to be discarded. The frequency of lost data runs increased with the number of connected oscilloscopes.

To avoid these limitations, a custom DAQ software was designed and implemented in late 2010. The design of the program is shown in Fig. 4.10. It is based on the multi-threaded producer-consumer pattern. The main thread is used to configure the oscilloscope and to push an event structure containing the voltage samples along with a UTC timestamp to a threadsafe queue if a trigger is

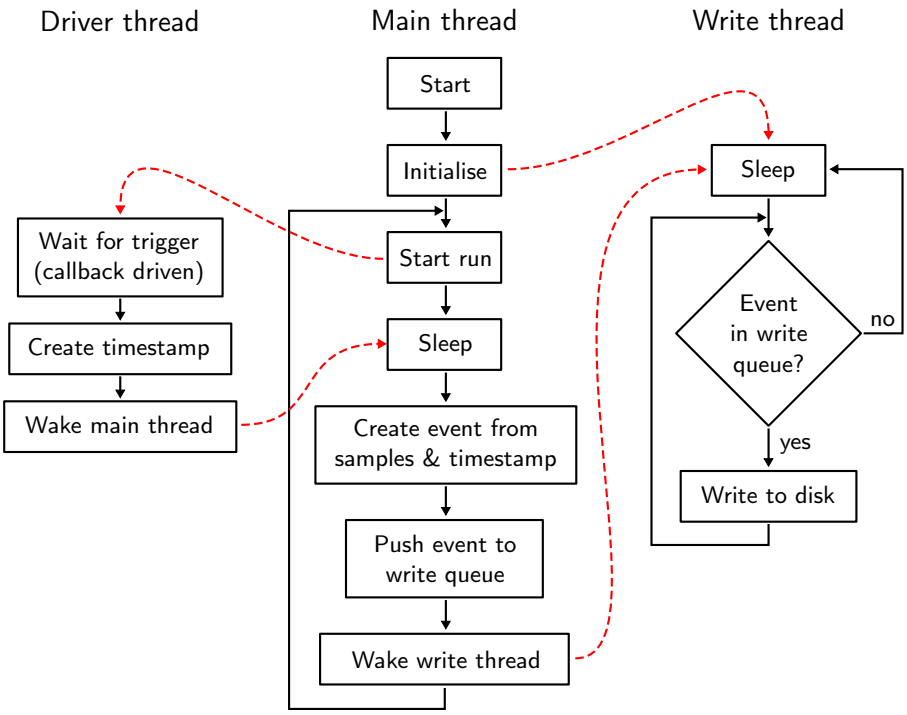


FIG. 4.10 • Multi-threaded design of the DAQ software developed for CROME. Cross-thread signals are indicated by dashed lines.

detected. The oscilloscope is then set up for the next trigger. When a new event arrives in the queue, a background thread is notified and the event is written to disk.

The new DAQ software was implemented in C++ using Microsoft Visual C++ 2010. Along with the C++ standard template library, the Boost C++ libraries [83] were used, e. g. for multithreading, cross-thread signalling, and resource locking. Additionally, optional compression of the voltage traces on disk was implemented using the bzip2 library [84].

With the described multi-threaded design, the deadtime of the DAQ was reduced to ~ 10 ms. Up to 11 oscilloscopes (44 channels) were connected at the same time with no detrimental effect on the performance.[j] With the new DAQ software, the typical duration of a run was extended from one to five days.

[j] *For this it was necessary to distribute the oscilloscope connections over 5 independent USB-2.0 chipsets.*

### *GPS logger*

For offline analyses, the voltage traces captured by the PicoScopes are associated with the appropriate KASCADE-Grande events via GPS-derived timestamps. To obtain timestamps for each Grande trigger, the GPS clock installed in the CROME DAQ was configured to write the current timestamp to a RS-232 serial port when a Grande trigger was received. The serial port was connected to the DAQ PC with a generic USB–RS-232 converter.

A Python [85] script was developed to listen to the virtual serial port installed by the drivers of the converter. The timestamps were received in text form and appended to a separate file for each data run. In an offline analysis step, the GPS timestamps are associated with the oscilloscope traces and merged

with the information provided by the KASCADE-Grande reconstruction for the appropriate event.

*Automated backup and monitoring*

In addition to the above applications for the data taking of CROME, periodic backups of the collected data were set up and several tools for monitoring the status of the experiment were developed.

Automated backups were implemented using rsync [86] to mirror the DAQ database, mounted remotely using the Common Internet File System (CIFS), to a storage cluster. The integrity of the backup was verified periodically by calculating the checksums of all data files.

To check whether the detectors performed as expected and the captured voltage traces were free of defects, a cross-platform event browser was developed (see Fig. 4.11). The browser was implemented in Python using the Qt toolkit [87] for the graphical interface, NumPy [88] for calculating the frequency spectra of the voltage traces, and matplotlib for plotting [89].

Additionally, an interactive website was developed which provided an overview of the current and past data runs (see Fig. 4.12). This allowed quick checks of the performance of the detectors and the RFI contamination. The underlying data was provided by a JSON database that was automatically updated after each periodic backup of the DAQ data. An additional PHP script was developed to stream voltage traces of individual events when requested for display. Interactive plotting was implemented using the jQuery JavaScript library [90] and the Flot plotting plugin [91].

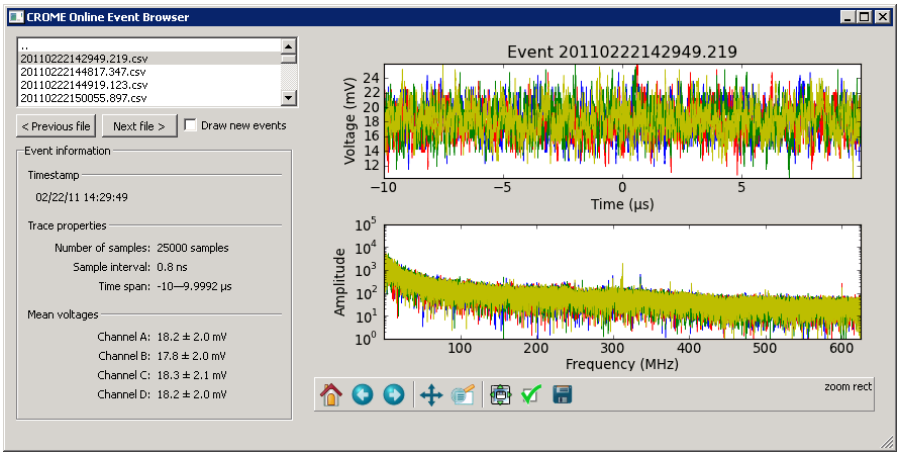


FIG. 4.11 • Screen capture of the CROME online event browser. General event information is shown in a panel on the left, while the voltage traces and the corresponding frequency spectra are shown in two interactive graphs on the right.

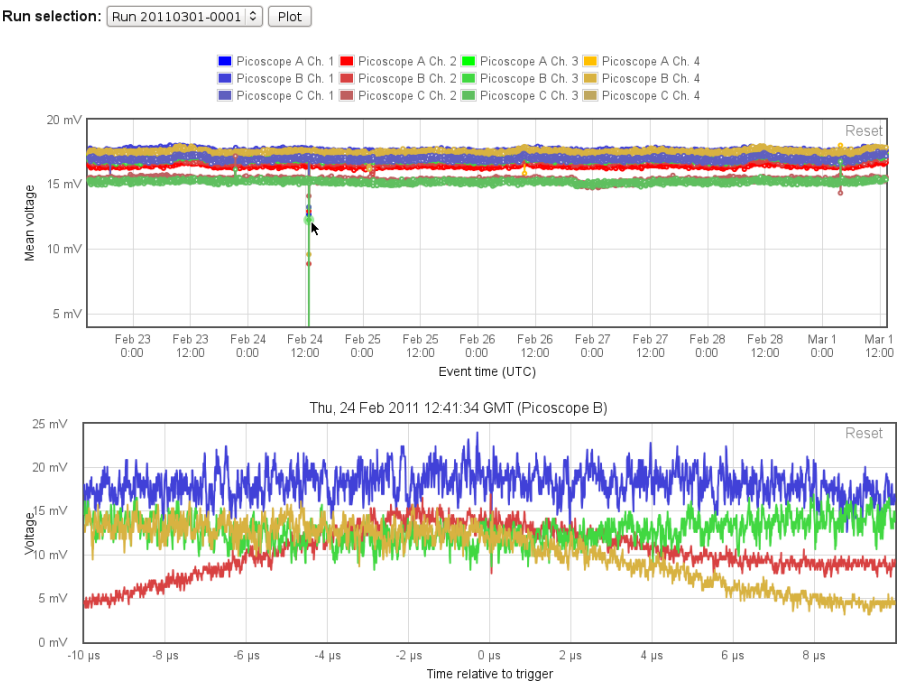


FIG. 4.12 • Screen capture of the web event browser. For a selected run, the evolution of the average voltages, corresponding to the received power, are shown for each data channel. The voltage traces of the selected event, which is contaminated with RFI, are shown in the lower graph.

# 5 DETECTOR CALIBRATION

A solid understanding of the detector characteristics is fundamental for its operation and the interpretation of the measured data. In this chapter, the experimental efforts in characterising the electronics and modelling its response are presented. To select and study event candidates, the position of the antennas and the pointing directions of the individual channels have to be known for the KASCADE-Grande coordinate system—the corresponding surveys and pointing measurements are described. Furthermore, the most prominent sources of RFI and the stability of the detector are discussed.

## 5.1 DETECTOR CHARACTERISTICS AND MODELLING

Over the course of the experiment, a number of measurements have been performed on the individual detector components to advance our understanding of the electronics response. Based on the results of these measurements, a simulation chain has been implemented.

In the following, the individual components of the detectors are described in detail together with dedicated measurements. For each set of components, the simulation model that has been implemented is described. The description is ordered in reverse of the actual signal path, i. e. starting with the oscilloscope and ending with the antenna system.

### 5.1.1 *Oscilloscope*

The output voltages of the electronics chains are sampled with USB oscilloscopes of the Pico Technology PicoScope 6400 series. The oscilloscopes feature four single-ended BNC inputs, each with configurable impedance (50 Ω, 1 MΩ) and operating range (±50 mV up to ±20 V in nine steps). The vertical resolution is 8 bit ($\Delta V = {}^{100\,\mathrm{mV}}/_{2^8-2} = 393.7\,\mu\mathrm{V}$ in the smallest input range) and the maximum sampling rate with four active channels is 1.25 GHz (0.8 ns sampling time). The −3 dB analogue bandwidth is quoted as 350 MHz. An additional offset voltage can be configured for each channel to shift the input range. A common sample buffer of 128 MS (PicoScope 6402) or 512 MS (PicoScope 6403) is shared by the active channels, which limits the maximum trace length. An additional 50 Ω input is available for triggering only.

#### *Data acquisition*

In normal data acquisition mode, the fast envelope outputs of the electronics chains were digitised with a ±50 mV input range, 50 Ω input impedance, and 1.25 GHz sampling rate. Time windows of ±10 µs (25 000 samples) around the trigger time were stored. The noise floor of the ADCs is comprised of white noise

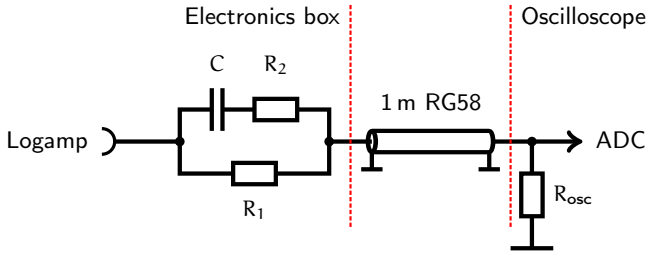


FIG. 5.1 • Schematic of the post-detection filter. The main part of the filter is contained in the electronics box as the last element of the electronics chain. The output is connected to an oscilloscope with a 1 m RG58 cable. In combination with the oscilloscope termination (50 Ω or 1 MΩ) the filter acts as a frequency dependent voltage divider.

with a standard deviation of 0.4 least significant bits (LSBs) (157.5 µV). Each ADC channel has an additional voltage offset of up to 4 LSBs (1.6 mV) which can be measured by shorting the input.

For calibration measurements the input range was usually set to ±2 V at 1 MΩ input impedance, effectively disabling the fast envelope filter.

*Simulation model*

The simulation model takes a discrete time sequence of voltage samples with sampling time $t_{s,sim}$ as input. The functionality of the oscilloscope is simulated in four steps: downsampling, addition of noise, discretisation, and clipping.[a]

[a] *The frequency dependent input attenuation is not considered since the logamp model is tuned to match the measured rise time of the complete detection chain, see § 5.1.3.*

For the simulation of the downsampling process, the sampling time of the oscilloscope $t_s$ is required to be a multiple of the input sampling time $t_{s,sim}$. For this case, downsampling is implemented simply by selecting each $n^{th}$ sample, with $n = t_s/t_{s,sim}$, of the input sequence. Since the oscilloscopes are not synchronised with a common clock source, the phase offset of the ADC clock with respect to the input trace has to be considered. The phase offset is taken to be uniformly distributed in $[0, t_s)$ in discrete steps of $t_{s,sim}$. The simulated time jitter is then

$$\sigma_t = \sqrt{\frac{t_s^2 - t_{s,sim}^2}{12}}, \tag{5–1}$$

converging to the real jitter $\sqrt{t_s^2/12}$ for $t_{s,sim} \ll t_s$.

[b] *Channel offsets are taken into account in the calibration of the offset voltages of the logamps.*

Noise taken from a zero-mean[b] Gaussian distribution with standard deviation $\sigma_V = 0.4$ LSBs is added to the voltage samples. The downsampled sequence is then discretised in steps of $\Delta V$ and clipped for the measurement range of the channel.

### 5.1.2 *Post-Detection Filters*

Starting with the second revision of the electronics chain, the output voltage of a logamp is filtered by a passive RC filter, see Fig. 5.1. The main purpose of the filter is to increase the effective resolution for measuring transients while retaining sensitivity to the average noise level by attenuating low frequencies relative to high frequencies. For frequencies lower than a characteristic frequency $f_c$ the

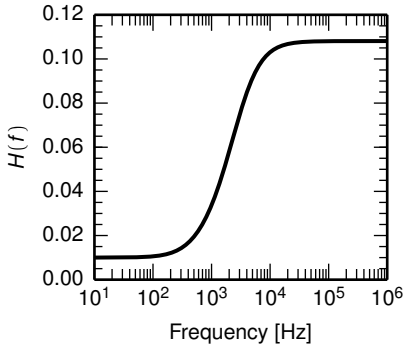


FIG. 5.2 • Transfer function of the post-detection filter as a function of frequency. For frequencies significantly higher (lower) than the characteristic frequency of ~ 3 kHz the transfer function converges to 0.112 (0.0097).

filter effectively acts as a voltage divider between $R_1$ and $R_{osc}$ and the transfer function will converge to

$$H(f \ll f_c) = \frac{R_{osc}}{R_1 + R_{osc}}. \tag{5–2}$$

For frequencies higher than $f_c$ the resistance of the capacitor is negligible and a voltage divider between $R_1 \parallel R_2$ and $R_{osc}$ is formed:

$$H(f \gg f_c) = \frac{R_1 R_{osc} + R_2 R_{osc}}{R_1 R_2 + R_1 R_{osc} + R_2 R_{osc}}. \tag{5–3}$$

The complete transfer function of the filter is

$$H(f) = \frac{R_{osc} + CR_1 R_{osc} \cdot s + CR_2 R_{osc} \cdot s}{R_1 + R_{osc} + CR_1 R_2 \cdot s + CR_1 R_{osc} \cdot s + CR_2 R_{osc} \cdot s}, \tag{5–4}$$

with $s = i2\pi f$.

The values of the electrical components were selected to obtain an attenuation of ~ 0.1 for frequencies above 10 kHz, and ~ 0.01 for lower frequencies:

$$\begin{aligned} R_1 &= 5100\,\Omega \\ R_2 &= 430\,\Omega \\ R_{osc} &= 50\,\Omega \text{ (oscilloscope termination)} \\ C &= 100\,\text{nF} \end{aligned}$$

Note that for a termination of $R_{osc} = 1\,M\Omega$ the transfer function is, for practical purposes, unity. The transfer function for a filter with these components and $R_{osc} = 50\,\Omega$ is shown in Fig. 5.1. The transition region is expected to be between 100 Hz and 100 kHz and the nominal high (low) frequency attenuation is 0.112 (0.0097).

*Measurements*

For the above analysis the influence of the output impedance of the logamp and the parasitic capacities at the oscilloscope input have been neglected. In addition, component tolerances, the mechanical structure, and the transmission line are expected to introduce further corrections and frequency dependences. It is

therefore desirable to measure the actual transfer function for each combination of logamp, filter, and oscilloscope.

As a first approximation, the voltage measured at the input of a post-detection filter has been compared with the output voltage. The filter output was measured as in normal data acquisition (1 m RG58 cable, 50 Ω termination), while the voltage at the filter input was measured with a Pico Technology TA101 high-impedance voltage probe. For frequencies below ~ 150 MHz the impedance of the probe is high enough not to influence the characteristics of the system. Measurements at higher frequencies were affected by induced resonances. The DC attenuation of the filter is 0.009 81 ± 0.000 02. The attenuation between 1 MHz and 150 MHz is 0.107 with a ripple of ±0.005. The observed ripple is not reproduced by the model and a result of the effects discussed above. For a detailed understanding of the filter and the consequences of the frequency dependence, more measurements are required.

Another practical measure for the high-frequency attenuation can be derived from the standard deviations of the traces measured at the input and the output of the filter. For trace lengths which are short compared to $f_c^{-1}$, the ratio of the two standard deviations corresponds to the high-frequency attenuation convolved with the output spectrum of the logamp. For the measurements discussed in the previous paragraph the ratio is 0.106 ± 0.001.

*Simulation model*

Lacking a realistic model for the transfer function, a simplified simulation has been implemented. Given a discrete time sequence of voltage samples $V_i$, the output samples are calculated via

$$V_{i,out} = (V_i - M) \cdot H_{AC} + M \cdot H_{DC}, \tag{5–5}$$

with M being the mean voltage of the sequence[c] and $H_{AC} = 0.106$ ($H_{DC} = 0.0098$) the high-frequency (low-frequency) limits of the (ideal) transfer function. In other words, all flucutations within the trace are assumed to be of "high" frequency. Note that this approach is only valid for trace lengths $\ll f_c^{-1}$.

[c] *For simulations of transient signals, the mean outside the signal window is calculated.*

### 5.1.3 *Demodulating Logarithmic Amplifier*

The down-converted and filtered RF signals are transformed using a demodulating logarithmic amplifier, also called logarithmic power detector or simply logamp. A logamp is typically used to detect signal strengths over a large dynamic range by converting the signal power to a voltage approximately proportional to the logarithm of the power. An ideal logamp implements the function

$$V_{out} = V_{slope}\,[\mathrm{V\,dB^{-1}}] \cdot (P_{in}\,[\mathrm{dBm}] - P_o\,[\mathrm{dBm}]), \tag{5–6}$$

i. e. the output voltage $V_{out}$ is proportional to the input power $P_{in}$ in dBm, with $V_{slope}$ being the slope and $P_o$ the intercept of the response curve.[d]

A detailed understanding of this highly non-linear transformation is crucial for the interpretation of the sampled traces. In the following, the transformation technique will be analysed and the properties of the specific logamp used

[d] *Units of dBm are typically used, but the reference power level actually cancels since $P_{in} - P_o$ yields the power ratio in dB.*

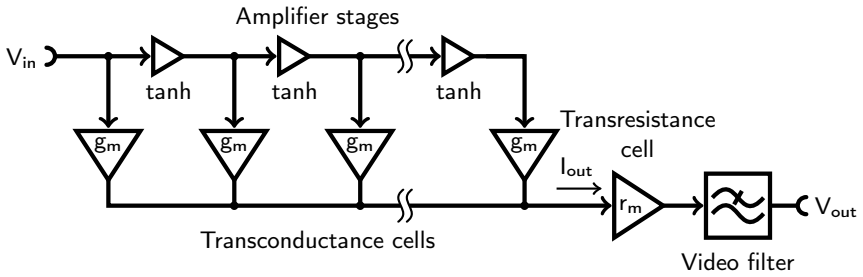


FIG. 5.3 • Simplified block diagram of a demodulating logarithmic amplifier. The input waveform $V_{in}$ is passed through a cascade of non-linear amplifiers. The output voltages of each amplifier stage are rectified and converted to currents in transconductance cells $g_m$. The combined currents $I_{out}$ are converted back to a voltage in a transresistance cell $r_m$. The waveform is low-pass filtered to reduce the ripple. The output voltage $V_{out}$ is approximately proportional to the logarithm of the input power.

for CROME will be demonstrated with a set of measurements. Based on these findings, a simulation model was implemented, which will be introduced and compared with the measurements.

*Logamp theory*

In the CROME electronics chain, a Mini-Circuits ZX47-60+ logamp is used, which is based on the Analog Devices AD8318 chip [92, 93]. The logarithmic response is implemented using the *progressive compression* technique. A simplified block diagram is shown in Fig. 5.3. The RF input voltage is fed through a cascaded chain of non-linear amplifiers, each amplifier saturating at an input voltage of $E_K$ (knee voltage). The input signal will hence clip at a certain stage depending on its magnitude. The output of each amplifier is full-wave rectified and converted to a current via transconductance cells. The currents are summed by connecting the outputs of the transconductance cells and converted back to a voltage with a transresistance cell.

To understand why the output voltage increases linearly with an exponential increase of the input signal in this design, let us first consider a cascade of $n_{cells}$ idealised amplifier cells. Each cell implements the so-called $A/0$ transfer function depicted in Fig. 5.4a, its incremental gain being $A$ for $|V_{in}| < E_K$ and 0 otherwise. The output voltage will be formed by $n_{clip}$ clipping amplifier stages and $n$ non-clipping amplifier stages. The latter contribution will be dominated by the output of the last non-clipping amplifier stage,

$$V_{out} \approx A^n \cdot |V_{in}| + n_{clip} \cdot A \cdot E_K, \tag{5–7}$$

with $n_{cells} = n + n_{clip}$. The number of unsaturated stages $n$ can be calculated from the condition

$$A^{n-1} \cdot |V_{in}| = E_K. \tag{5–8}$$

Taking into account that $n$ is a positive integer[e] and limited to $n_{cells}$, three

[e] *The floor operation, $\lfloor\,\rfloor$, will be used to denote this.*

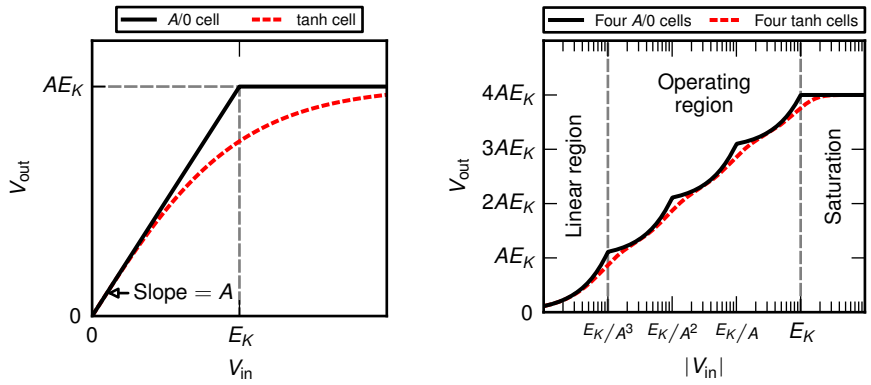


(A) Transfer function for an amplifier cell of a logamp: the idealised A/0 function (black line) and the hyperbolic tangent (tanh) implemented in practice (red dashed line). Both functions have a small signal gain of A and saturate at $V_{in} = E_K$.

(B) Output voltage of an ideal logamp with four amplifier stages comprised of A/0 cells (black line) or tanh cells (red dashed line) as a function of input voltage. Note the logarithmic scale of the abscissa.

FIG. 5.4 · Transfer functions for two types of amplifier cells (left panel), and resulting transfer functions for an ideal logamp with four cells (right panel).

cases emerge: 1) the linear region, in which no cell is saturated, 2) the operating region of the logamp, and 3) saturation of the complete amplifier cascade;

$$n = \begin{cases} n_{\text{cells}} & \text{if } A^{n_{\text{cells}}-1} \cdot |V_{\text{in}}| < E_K, \\ \left\lfloor 1 + \log_A \frac{E_K}{|V_{\text{in}}|} \right\rfloor & \text{if } A^{n_{\text{cells}}-1} \cdot |V_{\text{in}}| \geq E_K > |V_{\text{in}}|, \\ 0 & \text{otherwise.} \end{cases} \tag{5–9}$$

Inserting this into Eq. (5–7),

$$V_{\text{out}} = A^{\lfloor 1+\log_A E_K/|V_{\text{in}}| \rfloor} \cdot |V_{\text{in}}| + \left( n_{\text{cells}} - \left\lfloor 1 + \log_A \frac{E_K}{|V_{\text{in}}|} \right\rfloor \right) \cdot A \cdot E_K, \tag{5–10}$$

for the operating region. Neglecting the quantisation of n, the logarithmic dependence on the input voltage becomes apparent:

$$V_{\text{out}} \approx \left( n_{\text{cells}} - \log_A \frac{E_K}{|V_{\text{in}}|} \right) \cdot A \cdot E_K \tag{5–11}$$

$$= \left( n_{\text{cells}} - \log_A E_K + \log_A |V_{\text{in}}| \right) \cdot A \cdot E_K. \tag{5–12}$$

The slope per dB of this approximation,

$$V_{\text{slope}} = \frac{1}{20} \frac{\partial V_{\text{out}}}{\partial \log_{10} V_{\text{in}}} = \frac{A \cdot E_K}{20 \log_{10} A}, \tag{5–13}$$

is constant and determined entirely by the voltage gain A of an amplifier stage and its knee voltage $E_K$. Due to the quantisation of n, the output voltage in Eq. (5–10) is piecewise linear, with discontinuities at multiples of $A \cdot E_K$. This

is illustrated in Fig. 5.4b for a logamp comprised of four A/0 amplifier stages (solid line). For practical applications, the transfer functions of the amplifier cells are realised in hyperbolic tangent (tanh) shape [94], see Fig. 5.4a. The smooth transition from the linear region to saturation results in a smooth output voltage curve—the output voltage of a cascade of four tanh amplifier stages is shown in Fig. 5.4b as dashed line. The log-conformance of this type of cascade is typically of the order of ±1 dB.

*Practical considerations and limitations*

In an ideal logamp, the number of amplifier cells determines the lower limit of the dynamic range. However, for a real logamp the lower limit is increased by internal noise. Still, large dynamic ranges of up to 60 dB have been realised.

As described above, the output voltage of a real logamp is derived from the combined currents of the full-wave rectified outputs of transconductance cells. In this process, the voltage will typically be adjusted by an offset and rescaled to a useful range. The bandwidth of the output voltage is typically limited by the bandwidth of the amplifier cells and any stray capacitance at the output stage. In practical applications, an additional low-pass filtering is added to reduce any unwanted fluctuations of the output voltage, e. g. the ripple introduced by the full-wave rectification. Such a low-pass filter, also called video filter, is typically included at the output stage of the logamp, and its corner frequency $\Delta\nu_{\text{video}}$ (video bandwidth) can be adjusted using external circuitry. The inverse video bandwidth determines the rise time[f] of the detector $\tau = (2\pi\,\nu_{\text{video}})^{-1}$ and hence the sensitivity for short RF pulses. For the geometry of the CROME detectors, microwave pulses from air showers are expected to be as short as a few nanoseconds. Therefore, the video bandwidth should be adjusted to be as large as possible, in the ideal case matching the analogue bandwidth of the oscilloscope sampling the output.

[f] *The rise time is defined here as the exponential time constant, i.e., the time it takes for a deviation from the steady-state to pass* $\exp -1$ *of the full step height.*

Due to the non-linear transformation implemented in a logamp, all information on input frequency and phase are lost. In other words, the input spectrum and waveform cannot be recovered, and analyses depending on the phase, e. g. reconstructing the polarisation ellipse of a measured signal, are not possible.

From the above derivation of the response of a logamp it is clear that logamps do not react on the input power, but on the input *waveform*. It follows that input signals with equivalent RMS powers but different waveforms yield different output voltages. Conversely, the shape of the input waveform must be known to calculate the input power from the measured output voltage. For example, when applying a calibration curve derived from sinusoidal inputs, the input power calculated from an output voltage has to be rescaled by −3.0 dB for a square wave input, and +2.5 dB for white noise [95]. Hence, for our application, reconstructing the input power is only possible assuming an emission model for the microwave radiation of air showers.

TAB. 5.1 • Typical values of the parameters of the AD8318 logamp for frequencies below 2 GHz [93, 94].

| Parameter | Value |
|---|---|
| amplifier stages | $n_{cells} = 9$ (tanh type) |
| nominal gain | $A = 8.7\,\mathrm{dB}$ |
| knee voltage | $E_K = 2k_B T e^{-1}$ * |
| −3 dB cell bandwidth | $\Delta\nu_{cell} = 10.5\,\mathrm{GHz}$ |
| slope | $V_{slope} = -25\,\mathrm{mV\,dB^{-1}}$ |
| intercept | $P_o = 21\,\mathrm{dBm}$ |
| ±1 dB dynamic range | −1 dBm to −58 dBm |
| temperature sensitivity | $< 0.01\,\mathrm{dB\,K^{-1}}$ |
| video bandwidth | 45 MHz† |

* $E_K \approx 50\,\mathrm{mV}$ at room temperature.
† Can be reduced with external circuitry (see text).

*Specifications of the AD8318 logamp*

The typical values for the parameters of the AD8318 logamp are given in Tab. 5.1. Note that the slope of the response curve is negative, meaning that the output voltage *decreases* with increasing input power. The corner frequency of the video filter can be adjusted using an external capacitor. On the Mini-Circuits PCB, a 15 pF capacitor is added to reduce the bandwidth to $\Delta\nu_{video} \approx 6\,\mathrm{MHz}$ (corresponding to a rise time of ~ 30 ns).

To verify the parameters given by the manufacturer, a series of tests was performed using microwave signal generators. It is important to note that the tests were not performed on isolated logamps, but on complete electronics chains.

*Log-conformance and frequency dependence*

The log-conformance of the detector curve was tested by applying continuous sine waves with frequencies of 900 MHz to 1800 MHz in steps of 100 MHz and RMS powers of −64 dBm to 22 dBm in steps of 2 dB. For this measurement, a Rohde & Schwarz SMF100A signal generator was connected to the SMA input of an electronics chain.[g] The fast envelope output was digitised using a PicoScope 6402. In Fig. 5.5a, the average voltage $V_{fast}$ is plotted as a function of the input power $P_{in}$. A linear dependence of the output voltage can be observed for $10\,\mathrm{mV} \lesssim V_{fast} \lesssim 20\,\mathrm{mV}$. For frequencies lower than about 1200 MHz, the attenuation of the high-pass filter in the electronics chain leads to a shift of the detector curve to higher voltages.

To estimate the log-conformance, the data points with $10\,\mathrm{mV} < V_{fast} < 18\,\mathrm{mV}$[h] were fitted with a line, yielding the parameters $V_{slope}$ and $V_{offset}$ for each

[g] *The generator was kindly provided by V. Verzi and colleagues during our stay at the AMY experiment at the Frascati linear accelerator.*

[h] *This voltage range contains the typical dynamic range of the CROME detectors.*

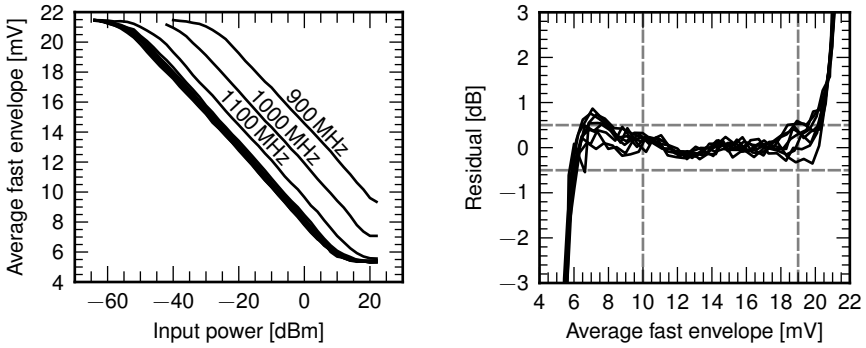


(A) Calibration curves of an electronics chain for frequencies of 900 MHz to 1800 MHz. The average fast envelope output is shown as a function of input power. For frequencies $\lesssim 1200$ MHz the attenuation due to the high-pass filter results in shifts to higher voltages.

(B) Log-conformance of the electronics chain derived from line fits to the calibration curves between 10 mV and 19 mV output voltage. The fit residuals are shown in dB as a function of the fast envelope voltage. In the region marked by dashed lines the log-conformance is better than ±0.5 dB.

FIG. 5.5 • Calibration curves (A) and derived log-conformance (B) of an electronics chain measured for sinusodial inputs from a microwave signal generator.

frequency. The residuals of the fits converted to dB, $\left(V_{\text{fast}} - V_{\text{slope}} \cdot P_{\text{in}} - V_{\text{offset}}\right) \cdot V_{\text{slope}}^{-1}$, are shown in Fig. 5.5b as a function of $V_{\text{fast}}$. For the fitted voltage range, the residuals are within ±0.5 dB, which demonstrates the excellent log-conformance of the detector. The region is marked by dashed lines in Fig. 5.5b.

The fit parameters can be used to study the frequency dependence of the electronics chain. The intercepts of the fitted lines are within ±1.0 dB for frequencies ≥ 1200 MHz. The spread is compatible with the ripple of the attenuation of the high-pass filter (see next section). The average fitted slope $\langle V_{\text{slope}} \rangle = -242\,\mu\text{V dB}^{-1}$, and the slopes vary by less than ±2 % over the full frequency range.

*Pulse response*

Understanding the response of the detector to short RF pulses is important for estimating the sensitivity of the detector to signals from air showers. Three series of measurements were done in this respect. The first measurements, done in February 2011, showed that the end-to-end rise time of the second-to-last revision of the detection electronics was ~ 30 ns. Following this finding, the external video filters of the logamps were removed from the Mini-Circuits PCB to improve the sensitivity to the short transients expected from air showers. A subsequent measurement in April 2011 revealed an improved rise time of the upgraded channels of ~ 4 ns, but was limited by the rise time of the pulse generator. The third series of measurements was performed in December 2011 with a faster signal generator. The rise time of the channels was determined to be about 3 ns, a factor of ~ 10 faster than for unmodified logamps.

The first two measurement series were done in collaboration with A. Schlaich at the Institute for Neutron Physics and Reactor Technology (KIT). An Agilent

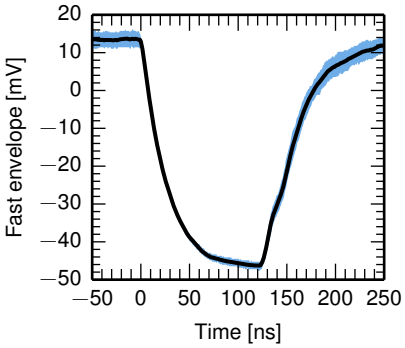


FIG. 5.6 • Response of the second-to-last revision of the electronics chain, including a Norsat 8215F LNB, to a 120 ns RF pulse at 3.6 GHz. The average of 120 pulses is shown as black line. 68 % of all measured pulses are contained in the shaded region. The rising and falling edge have an exponential shape with a time constant of ~ 30 ns.

N5183A MXG microwave signal generator was used to generate RF pulses of 120 ns width (the minimum available pulse width). The rise time of the RF pulses themselves was estimated by sampling the pulses directly. The exponential time constant of the envelope power, i. e. the time interval between the start of the pulse and the envelope power reaching 63.2 % of the maximum output power, is $\tau_{gen} \approx 4$ ns.

In the first series of measurements, a 3.4 GHz two-element Yagi antenna was used to transmit the RF pulses. To match the signal to the dynamic range of the detector and to minimise reflections at the antenna terminal, a total of 50 dB of attenuation were installed in the signal path. The signal was received by a Norsat LNB at approximately 1 m distance of the transmitting antenna. It was connected to an electronics chain of the second-to-last revision, i. e. containing all upgrades except the modified logamps. The fast envelope output was digitised with a PicoScope 6403. For synchronisation, the generator and the PicoScope were triggered by the same source.

The carrier frequency was swept from 3.3 GHz to 4.0 GHz in steps of 100 MHz at a constant power level. At 3.6 GHz, the output power was additionally swept over a range of 25 dB. For each setting, more than one hundred pulses were measured. The average fast envelope trace of 120 pulses at 3.6 GHz and the highest power level are shown in Fig. 5.6. The rise time is estimated to ~ 30 ns by fitting an exponential pulse shape. Within the statistical and systematic errors of the fits, the rise time is independent of both the carrier frequency and the amplitude.

In the second series of measurements the signal generator was directly connected to the SMA inputs of the electronics box to avoid the interference of external noise. Prior to the measurements, two of the four logamps contained in the electronics box had been modified by removing the external video filters. The pulse responses of one unmodified and one modified electronics chain (averaged over 65 measurements each) to a 120 ns long pulse with 1.4 GHz carrier frequency are shown in Fig. 5.7. For the modified logamps, the improved rise time is clearly visible. As a result, the shape of the (nearly) rectangular envelope is reproduced more accurately and the sensitivity of the electronics chain for short pulses is improved.

The rising and falling edges of the detected pulses are symmetric and well described by exponentials with a time constant of $\tau = (28 \pm 2)$ ns for the unmodified logamps, and $\tau = (4.0 \pm 0.4)$ ns for the modified logamps. Since

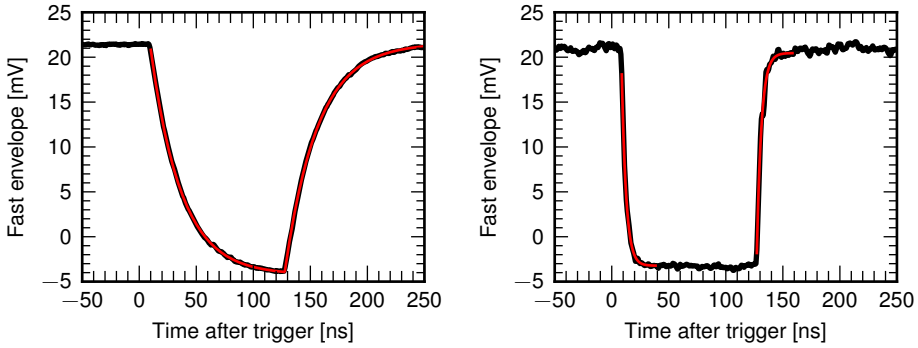


FIG. 5.7 • Response of the second-to-last revision (left panel) and last revision (right panel) of the electronics chain to a 120 ns RF pulse at 1.4 GHz. The averages of 65 measured pulses (thick black lines) are overlayed by exponential fits (thin red lines) to the rising and falling edges. The rise time improved from 28 ns to ≤ 4 ns. The faster rise time of the modified logamps result in an improved sensitivity for short transients as expected from air showers.

the latter time constant is in the range of the rise time of the RF pulses, it is to be treated as an upper limit to the actual rise time of the detector.

The above measurements were repeated with a different signal generator (Rohde & Schwarz SMF100A) for comparison. The RF pulses were characterised using a LeCroy WavePro 7300A oscilloscope[i] with 3 GHz analogue bandwidth: they exhibit rise times of $\tau_{gen} \approx 3\,ns$, slightly faster than for the previously used Agilent signal generator. The pulses were fed directly into an electronics chain with modified logamps and the fast envelope output was sampled with a PicoScope 6403. The shape of the output pulse is well described by symmetric exponential edges with time constants of $\tau = (2.9 \pm 0.4)$ ns. Again, this value is an upper limit to the actual rise time of the detector, albeit the lowest we were able to measure with the available equipment. Since the shape of the pulses was measured both at the input of the electronics box with a high-bandwidth oscilloscope and at the output, this set of measurements can be used to verify the simulation model of the electronics chain.

[i] *The oscilloscope was also kindly provided by V. Verzi and colleagues.*

*Simulation model*

Based on the measurement results and the specifications given in the datasheet of the AD8318, a simulation model has been developed.

The nine amplifier cells are modelled with hyperbolic tangent transfer functions with the parameters given in Tab. 5.1. The cell bandwidth is treated as infinite, i. e. the individual cell outputs are not filtered. Thermal noise at the input of the amplifier cascade is simulated as white noise. The scaling and shifting due to the transconductance and transresistance cells is simulated by scaling the sum of the rectified cell output voltages by

$$S = f_{corr} \cdot V_{slope} \cdot \frac{20 \log_{10}(A)}{A \cdot E_K}, \tag{5–14}$$

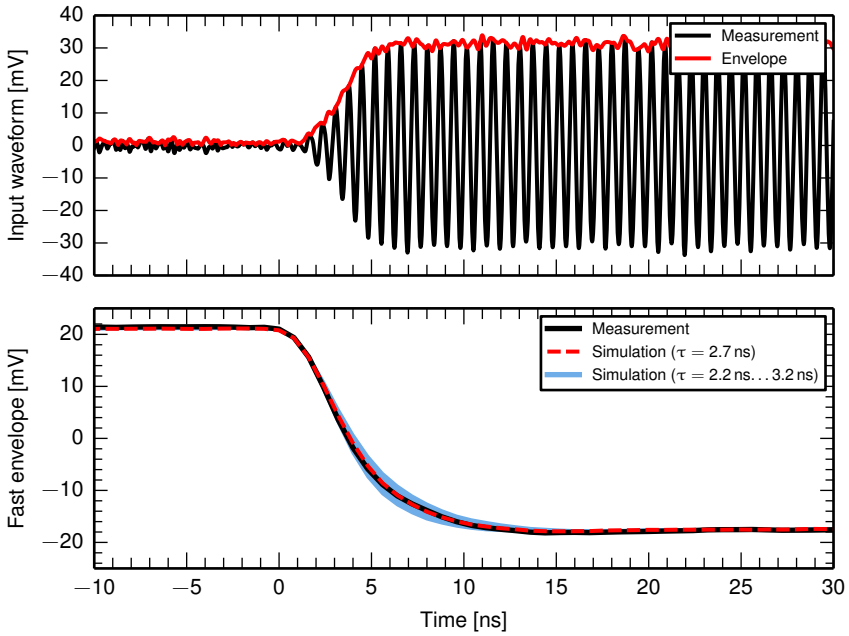


FIG. 5.8 • Input waveform (upper panel) and response of the complete electronics chain (lower panel, black line) compared to the simulated response (red dashed line). The input waveform, an RF pulse with carrier frequency 1.4 GHz, was measured with a fast oscilloscope. The shown pulse response is the average of 291 measured pulses. The pulse response was simulated assuming different time constants $\tau$ (blue shaded region) and is best reproduced with $\tau = 2.7$ ns.

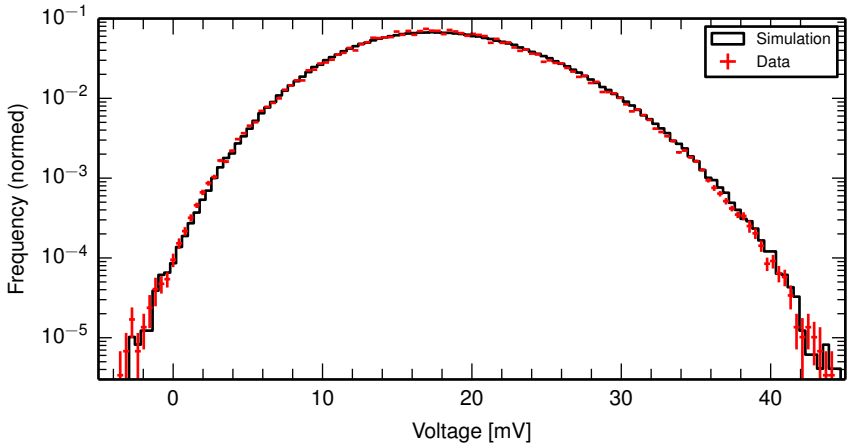


FIG. 5.9 • Simulated (black histogram) and measured (red histogram) noise distribution for the complete detection chain. The measured distribution for 200 µs of antenna data (10 captured traces) is shown. The shape of the noise distribution is well reproduced by the simulation.

and adding an offset voltage

$$V_{\text{offset}} = \left[ 10 \log_{10} \left( \left( \frac{E_K}{f_{\text{corr}} A^{n_{\text{cells}}}} \right)^2 \cdot \frac{1}{50\,\Omega \cdot 1\,\text{mW}} \right) - P_0\,[\text{dBm}] \right] \cdot V_{\text{slope}}. \quad (5\text{–}15)$$

An empirical correction factor $f_{\text{corr}}$ is used to account for differences between the implementation and the simplified model on which Eq. (5–13) is based. The factor is determined from the slope of the simulated calibration curve in the region of interest. For example, for a sinusoidal input, a correction factor of $f_{\text{corr}} = 1.025$ produces the requested slope and offset in the region of $-50\,\text{dBm} < P_{\text{in}} < -25\,\text{dBm}$.

The video filter is modelled as a first-order low-pass filter with a configurable time constant $\tau$. The exponential rising and falling edges observed in the measurements are well reproduced by this type of filter.

In summary, the simulation model has three free parameters which have to be determined experimentally for each device:

- $V_{\text{slope}}$ [V dB$^{-1}$]: the slope of the detector curve,
- $P_0$ [dBm]: the intercept power of the detector curve, and
- $\tau$ [s]: the time constant of the video filter.

*Validation of simulation model*

The last set of measurements discussed above was used to validate the simulation model of the complete electronics chain and derive the time constants of the logamps used in these measurements. In Fig. 5.8, the waveform of an RF pulse is shown (upper panel, black line) as measured with a high-bandwidth oscilloscope. The measured response of the electronics chain to such pulses is shown in the lower panel as black line. The simulated response to the input waveform is shown as dashed red line for a time constant of $\tau = 2.7$ ns. The simulation reproduces the rising edge of the pulse as well as the overall shape and amplitude of the measurements.

A further test of the simulation model was to compare the distribution of noise voltage samples measured with the CROME antennas with simulations. For the simulation, white noise was filtered to the effective band of an LNB (see § 5.1.5 for details) and fed into the detector simulation. In Fig. 5.9, the distribution of the simulated output voltage (black histogram) is shown in comparison to the measured distribution of ten traces (200 µs, 250 000 samples). The noise power was adjusted to reproduce the measured average voltage. The shape of the noise distribution is reproduced by the simulation over more than four orders of magnitude. Furthermore, the good agreement of the simulation with the measurements is an indication that the noise voltage measured with the CROME antennas is dominated by thermal noise.

### 5.1.4 *Passive Components*

In the signal path between an LNB and the detecting logamp, the IF signals are attenuated due to the following passive components:

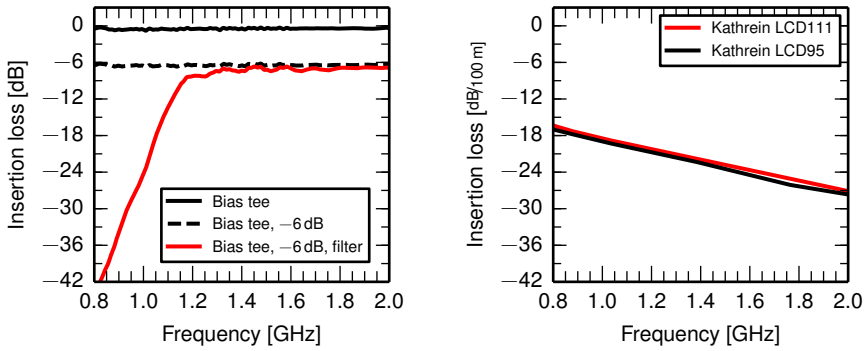


(A) Cumulative insertion loss of the passive components of the electronics chain.

(B) Attenuation per 100 m of the coaxial cables used to connect the LNBs.

FIG. 5.10 • Insertion loss of the passive components in the signal path between an LNB and the detecting logamp as a function of frequency: (A) components of an electronics chain, (B) cable attenuation taken from the datasheets.

- several tens of metres Kathrein LCD95 or LCD111 coaxial cable
- input adapters of the electronics box (F (75 Ω)–BNC (50 Ω)–SMA)
- Mini-Circuits ZFBT-352-FT+ bias tee
- Radiall R411806124 6 dB attenuator
- Mini-Circuits VHF-1200 high-pass filter

The insertion loss of the components was measured using an Agilent N9923A RF network analyser. The attenuation of the 75 Ω cables and the adapters however could not be measured to a satisfying degree of accuracy using the 50 Ω measurement system. The results of the measurements for the 50 Ω components are summarised in Fig. 5.10a. The attenuation curves of the cables taken from the datasheets are shown in Fig. 5.10b. The frequency dependence of the combined insertion loss is dominated by the high-pass filters and the cables. The main purpose of the high-pass filter is to attenuate aircraft altimeter radars operating at 4.3 GHz (850 MHz after down-conversion), just outside the operating band of the LNBs. The −3 dB corner frequency of the used Mini-Circuits VHF-1200 high-pass filter is 1150 MHz and its attenuation increases by about 10 dB per 100 MHz with decreasing frequency. Aircraft altimeter signals are attenuated by more than 30 dB with respect to the passband. Above 1200 MHz, the insertion of the high-pass filter leads to a ripple of about 1.7 dB.

The cable attenuation is about 18.5 dB per 100 m at 1 GHz and increases with a rate of 0.9 dB per 100 MHz. Due to the frequency dependence, the noise spectrum of the LNBs at the input of the logamps peaks at ~ 1.3 GHz.

### 5.1.5 *LNB*

The first electronic part in a detection chain is a Norsat 8215F C band LNB. The input frequency range of 3.4 GHz to 4.2 GHz is down-converted using a local

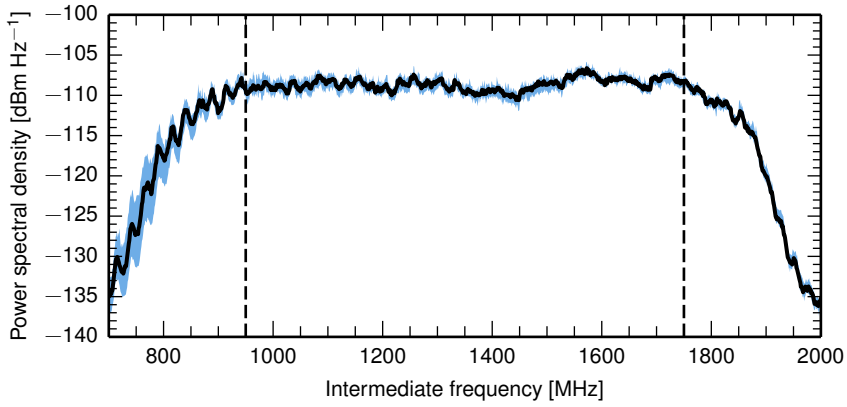


FIG. 5.11 • Median power spectral density from black body radiation at room temperature (black line) and total spread (shaded region) of eight Norsat 8215F LNBs with attached feed horns as a function of frequency in the IF band. The nominal IF band is indicated by dashed lines. The measurements were done in a shielded anechoic chamber at room temperature and corrected for the insertion and mismatch loss of the measurement chain. Part of the observed ripple, particularly at low frequencies, is due to impedance mismatches.

oscillator (LO) at $f_{LO} = 5.15\,\text{GHz}$ to the IF band of 950 MHz to 1750 MHz (low-side down-conversion, cf. § A.1). The conversion gain is not clearly specified by the manufacturer but expected to be in the range of 60 dB to 70 dB. The noise temperature is specified as 15 K. The active electronics of the LNB is supplied via the central conductor of the 75 Ω F connector. The 1 dB compression point, i. e. the output power at which the actual transfer function differs from the ideal, linear transfer function by more than 1 dB, is at $P_{1\,\text{dB}} = 8\,\text{dBm}$.

*Output spectrum*

To estimate the conversion gain and the gain flatness, the output spectrum of several LNBs was measured with a spectrum analyser. To suppress external interference and provide a known power level at the waveguide entrance, a small cryostat with a volume of 25 l was converted to a shielded anechoic chamber: lined with microwave absorbers (Telemeter Electronic EPF-51) it acts as a black body, i. e. a thermal noise source at room temperature.[j] A copper plate covering the container provides shielding and a fixture for a single Norsat LNB with attached feed horn.

[j] *The reflectivity of the absorber is* $< -25$ *dB above 3 GHz.*

In the Rayleigh-Jeans approximation, the thermal noise detected by an LNB is flat in frequency with a power spectral density of

$$N_\nu(T) = k_B T, \tag{5–16}$$

where T is the physical temperature of the absorber (see § 3.2). For room temperature, $T \approx 293\,\text{K}$, the detected power spectral density is $N_\nu(293\,\text{K}) \approx 4 \times 10^{21}\,\text{W Hz}^{-1} \approx -174\,\text{dBm Hz}^{-1}$.

Eight LNBs with feed horns have been tested in the chamber. A 5 m coaxial cable (Kathrein LCD111) was used to connect the LNBs to a benchtop spectrum analyser (Tektronix RSA 3408A) via a 75 Ω bias tee (Aeroflex 8875FFM3-03).

In Fig. 5.11 the median power spectral density for the eight tested LNBs is shown along with the total spread (shaded region). The spectra have been corrected for the approximate insertion and mismatch loss in the measurement chain. Due to the lack of 75 Ω measurement equipment, the specifications for cable and adapter losses given by the manufacturers have been used and the systematic uncertainty of the measurement is estimated to ±2 dB.

Comparing the noise spectra to the thermal input noise power, the average passband gain is estimated to 64.5 dB. The passband ripple is ±1.1 dB. Note that this is an upper limit to the actual passband ripple, since part of the observed fluctuations are due to the impedance mismatch (decreasing for longer cables) and the IF ripple of the spectrum analyser. The flat region of the spectrum extends beyond the specified passband, resulting in −3 dB and noise equivalent bandwidths of 955 MHz around the midband frequency. The bandwidth is reduced to 660 MHz when taking into account the high-pass filter of the electronics chain. The spectra of the individual LNBs vary by ±1.6 dB with respect to the median.

*Temperature dependent gain*

The LNBs are exposed to large daily and seasonal temperature fluctuations. The baseline level of the regular run data was found to correlate with the outside temperature. To identify the main cause for this correlation, the temperature dependence of the output spectrum of a spare LNB was tested in a simple laboratory experiment: the LNB was heated with a hot-air gun. After reaching thermal equilibrium, the hot-air gun was turned off and the spectrum and surface temperature of the LNB casing were recorded repeatedly during the cooling process. A temperature dependence of the conversion gain of about $-0.1\ \mathrm{dB\,K^{-1}}$ was observed, which is fully consistent with the overall fluctuations observed in the regular run data. Using the data collected over the course of more than one year, the temperature coefficients of the conversion gain of all LNBs have been estimated. This is shown in detail in § 5.3.

*Noise temperature*

Since the conversion gain of the LNBs is large compared to the subsequent losses in the electronics chain, the noise temperature of the complete system will be dominated by the noise temperature of the LNB (see § 3.2). The manufacturer specifies the noise temperature of the Norsat 8215F series as 15 K. To verify this claim, the noise temperature of a number of LNBs has been measured using the Y factor method. The method is based on comparing the output power of the LNBs when measuring two known input noise levels: a hot load of equivalent noise temperature $T_{n,hot}$ and a cold load $T_{n,cold}$. The output power $N_i$ measured for load i includes the noise contribution of the receiver system, the receiver noise temperature $T_{rx}$,

$$N_i = k_B (T_{n,i} + T_{rx}) \Delta\nu, \tag{5–17}$$

where $\Delta\nu$ is the measurement bandwidth.[k] The ratio of the powers measured

[k] *Note that both* $T_{n,i}$ *and* $T_{rx}$ *can change with frequency.*

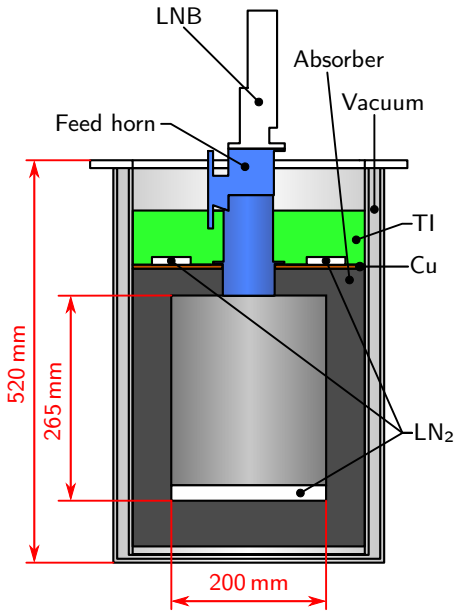


FIG. 5.12 · Technical drawing of the cryostat converted to a small, shielded anechoic chamber which can be cooled down to liquid nitrogen ($LN_2$) temperature. The inner volume is lined with flat microwave absorbers and acts as a black body. The top of the volume is covered by a copper plate providing shielding and a fixture for a single Norsat LNB with attached feed horn. Additional thermal insulation (TI) improves the uniformity of the temperature within the chamber. For cooling, liquid nitrogen is poured onto the copper plate and into the chamber, leaving thin layers of boiling $LN_2$.

with the two loads is called the Y factor,

$$Y = \frac{N_{hot}}{N_{cold}} = \frac{T_{n,hot} + T_{rx}}{T_{n,cold} + T_{rx}}. \tag{5–18}$$

For a given Y factor, the receiver noise temperature can be determined via

$$T_{rx} = \frac{Y \cdot T_{n,cold} - T_{n,hot}}{1 - Y}. \tag{5–19}$$

For measuring the Y factor, thermal loads with different physical temperatures $T_i$ have been used. The equivalent noise temperature of a thermal load measured by a single-polarisation receiver is $T_{n,i} = T_i$ in the Rayleigh-Jeans approximation.

For the purpose of measuring two different thermal loads in a short period of time, a second cryostat was converted into a shielded anechoic chamber, see Fig. 5.12. The inner volumes of the two cryostats are constructed identically. Thermal insulation was added on top of the second cryostat to allow cooling the volume uniformly down to $T_{cold} = 77.15\,K$ using liquid nitrogen ($LN_2$) while the other cryostat is kept at room temperature, $T_{hot} = 293\,K$. The temperature of the microwave absorber has been monitored at several positions to assert a uniform temperature distribution. During the measurements, an LNB with feed horn is first mounted in the chamber kept at room temperature until the output power is stable (warm-up period of the electronics). The LNB is then placed in the cooled chamber for a short period of time ($\lesssim 10\,s$) to avoid drifts of the electronics due to a change in temperature.

In two sets of measurements, the output power of the LNBs was measured using different methods. In the first method, the LNBs were connected to a complete electronics chain (last revision) as used in the experiment. This has the advantage of including the contributions of all components in the measurement. However, with this method no information on the frequency dependence of

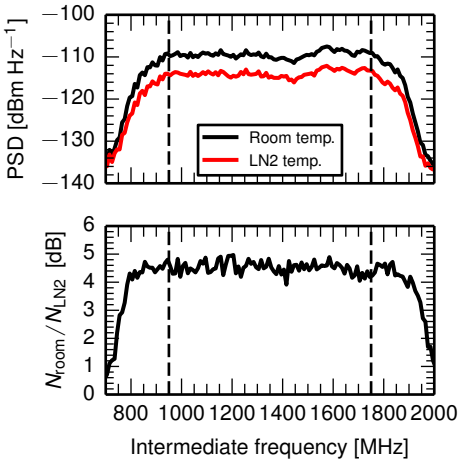


FIG. 5.13 · Power spectral densities (PSD, upper panel) obtained for a Norsat 8215F LNB mounted in an anechoic chamber at room temperature (black line) and at $LN_2$ temperature (red line). The ratio of the two spectra, the Y factor, is shown in the lower panel. In the nominal passband, indicated by dashed lines in both panels, the Y factor is approximately flat in frequency. The ratio of the integrated powers yields a receiver noise temperature of 42 K (see text).

the noise temperature can be obtained and an average slope of the power detector curve has to be used to convert the measured voltage difference to the Y factor. Therefore, a second set of measurements was obtained using a spectrum analyser by employing the same setup as for determining the output spectra of the LNBs.

The frequency dependent Y factors have been measured for three spare LNBs using the spectrum analyser setup. The spectra obtained for the two loads are shown in Fig. 5.13 for one LNB (upper panel) together with the ratio of the spectra (lower panel). The Y factors of all three LNBs are approximately flat in the extended passband, with the observed ripple being fully compatible with statistical noise. The Y factors calculated from the integrated spectra yield receiver noise temperatures of 42 K to 44 K.

Using a complete electronics chain, the change in the slow envelope voltage between the two loads has been measured for 13 LNBs. Using an average slope of the power detector curve of −25 mV dB$^{-1}$ for the conversion of voltage to Y factor, receiver noise temperatures between 42 K and 52 K have been obtained.

The noise temperatures obtained with both methods are compatible considering the different sample sizes. The noise temperatures are significantly larger than the 15 K claimed by the manufacturer. This discrepancy has been confirmed independently by P. Gorham [96]. Note, that the system temperature of the complete detector also includes the contribution of external radiation received by the LNB. An estimate of this contribution is given at the end of the next section.

### *Simulation model*

Since the LNB is the first electrical component in the detection chain, noise is simulated at this stage. The noise voltage is generated from a zero-mean Gaussian distribution with a standard deviation of

$$\sigma_n = \sqrt{k_B T_{sys} \nu_{sim} Z}, \tag{5–20}$$

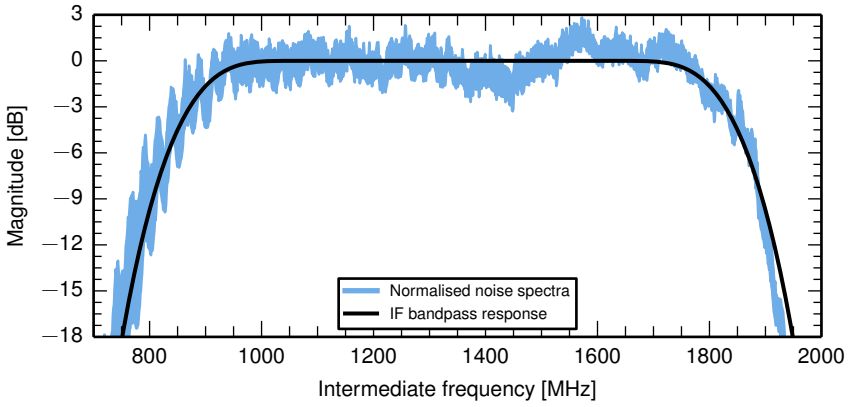


FIG. 5.14 • Range of normalised noise power spectral densities acquired for eight LNBs (blue region) as a function of frequency compared with the magnitude response of the simulated IF bandpass filter (black line). The bandwidth and roll-off rate of the simulated filter were chosen to approximately reproduce the features of the measured spectra.

where $T_{sys}$ is the system temperature of the detector, $\nu_{sim} = 1/2t_{s,sim}$ the bandwidth of the simulation (Nyquist frequency), and $Z = 75\,\Omega$ the system impedance.

The thermal noise is added to the input sequence of voltage samples. The samples are multiplied by $\sqrt{G_{LNB}}$, where $G_{LNB}$ is the power gain of the LNB. The temperature dependence of the gain is modelled using a linear temperature coefficient $g_T$.

The RF filter is implemented as a finite impulse response (FIR) filter. The coefficients are generated by applying a Blackman window to an ideal lowpass filter with corner-frequency $f_c = 1035$ MHz and upshifting to the midband frequency of 3.8 GHz. This results in a bandpass filter with a −3 dB bandwidth of 955 MHz. The mixing process is simulated using

$$V_{i,out} = 2V_i \cdot \cos(2\pi f_{LO} \cdot i \cdot t_{s,sim} + \phi_0), \tag{5–21}$$

with the phase offset $\phi_0$ drawn from a uniform distribution in $[0, 2\pi)$. Note the factor of two in Eq. (5–21), which is used to preserve the amplitude in the IF band. The subsequent IF bandpass is generated from the same FIR lowpass as the RF filter, but centred at the IF midband frequency of 1.35 GHz. A comparison of the attenuation curve of the IF FIR filter with the normalised output spectra of the LNBs is shown in Fig. 5.14.

### 5.1.6 *Reflector Antenna*

The reflectors used for the C band detectors are prime focus parabolic reflectors manufactured by Prodelin (1344 series). The parameters of the reflectors are specified as $D = 335.3$ cm, $f = 119.1$ cm ($f/D = 0.355$). The reflectors consist of eight segments of sheet moulding compound (SMC) with embedded reflecting material. They are installed on galvanised steel posts mounted on solid iron blocks. The pointing has been fixed during installation and is stabilised by additional steel ropes, see Fig. 4.6.

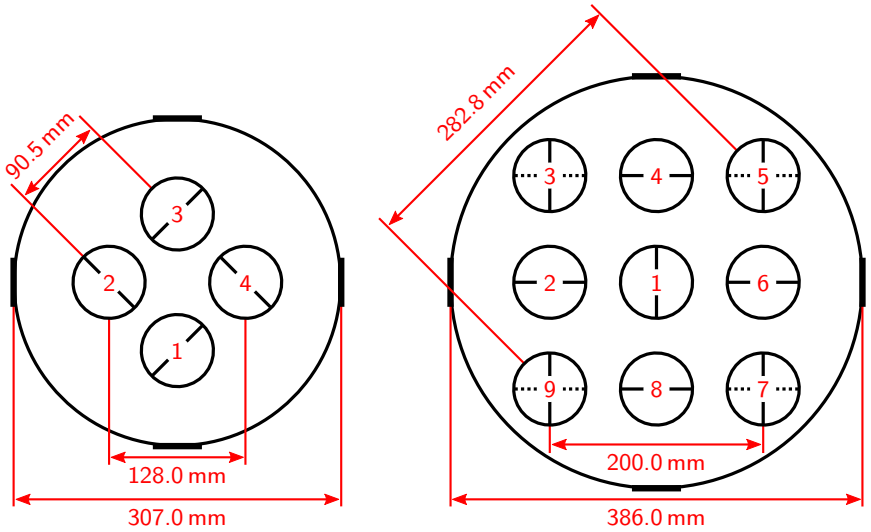


FIG. 5.15 • Technical drawings of the camera types that were used in the 3.4 m reflector antennas (top view). The four mounting positions for the struts supporting the camera body are indicated by thick lines. Each feed position is shown with the channel number and polarisation axis. The second polarisations of the dual-polarised feed horns are indicated by dotted lines.

*Mechanical quality*

To verify the specifications of the manufacturer, the depth of the first reflector was measured in steps of 20 cm along the north-south and east-west axes using a plumb line. Both sets of measurements are well described by a parabola with a focal length of $(118.7 \pm 0.2)$ cm, with residuals being $< 3$ mm. The diameter of the reflector was measured to be $(335.0 \pm 0.2)$ cm. Both parameters agree well with the specifications of the manufacturer. Since the measurements were done for the non-reflective SMC shell, the specifications of the manufacturer are used in the following.

*Camera design*

Two designs have been used for the cameras supporting the feed horns, a four feed and a nine feed design. Both camera types were realised as flat steel discs with an additional welded ring to mount four support struts (refer to Fig. 4.7 for a photograph of the nine feed camera). Technical drawings of the cameras are shown in Fig. 5.15. The cameras were mounted such that the feed entrance windows are at a height of 119.0 cm above the reflector base and particular care has been taken to centre and level the cameras with respect to the reflector plane.

*Radiation patterns*

To estimate the sensitivity of the antenna, the secondary radiation patterns of the feeds, i. e. gain as a function of direction, were calculated. The antenna gain is typically calculated for the transmit mode. For this, the electric field $\mathbf{E}(\mathbf{r})$ produced by the electric current distribution $\mathbf{J}(\mathbf{r}')$ on the reflector surface

induced by the primary radiation pattern is computed. Assuming the reflector is a perfect electric conductor [97],

$$\mathbf{E}(\mathbf{r}) = \frac{1}{i\omega\mu\epsilon}\left[\nabla(\nabla\cdot\mathbf{A}(\mathbf{r})) + k^2\mathbf{A}(\mathbf{r})\right], \tag{5–22}$$

with the vector potential

$$\mathbf{A}(\mathbf{r}) = \iint_S dS'\mu\mathbf{J}(\mathbf{r}')\frac{e^{-ik|\mathbf{r}-\mathbf{r}'|}}{4\pi|\mathbf{r}-\mathbf{r}'|} \tag{5–23}$$

and the reflector surface S.

Usually, two approximations are applied for solving the integral: 1) the far-field approximation, and 2) the physical optics approximation, for which the surface currents are approximated with those induced on an infinite conducting plane illuminated by a plane wave. The integral is then solved numerically, usually employing further approximations to improve the efficiency and numerical stability (see e. g. Ref. [98]).

We decided to rely on a commercial software package, GRASP 9 (student edition) [71], for the simulation of the radiation characteristics. In GRASP, the far-field and physical optics approximations discussed above are implemented and corrections for edge effects at the reflector rim are applied [71, 99]. However, in the free student edition effects introduced by the gaps between the reflector segments and the struts are not simulated, and the aperture blockage due to the camera is approximated with a central hole in the reflector with the diameter of the camera. The primary radiation pattern is assumed to be Gaussian with an edge taper of −12 dB at 70° from the forward direction. The reflector parameters given by the manufacturer were used along with the camera dimensions shown in Fig. 5.15.

Since no asymmetric structures are simulated, the secondary radiation patterns depend only on two parameters: the feed displacement $\delta$ and the radius of the camera shadow $r_s$. The secondary radiation patterns of all feeds can be obtained via rotation in azimuth of the radiation patterns obtained from four basic sets of parameters:

| Camera type | Feed position (no.) | $\delta$ [mm] | $r_s$ [mm] |
|---|---|---|---|
| Four feed | any (1–4) | 64.0 | 153.5 |
| Nine feed | central (1) | 0.0 | 193.0 |
| | edge (2, 4, 6, 8) | 100.0 | 193.0 |
| | corner (3, 5, 7, 9) | 141.4 | 193.0 |

The secondary radiation patterns simulated with GRASP for these configurations are shown in Fig. 5.16. The patterns agree well with the qualitative descriptions given in § 3.4. For increasing feed displacements, the boresight gain drops marginally from 41 dBi to 40 dBi at midband frequency. At the same time, the beam broadens slightly from 1.7° to 1.8° and the strength of the first side lobe (coma lobe) increases from −27 dB to −11 dB relative to the main lobe.

TAB. 5.2 • Parameters of the simulated radiation patterns—boresight gain $G_{max}$, boresight angle $\theta_B$, and half-power beamwidth $\theta_{3\,dB}$—for individual camera configurations—feed displacement $\delta$ and shadow radius $r_s$—, and frequencies $f$.

| $\delta$ [mm] | $r_s$ [mm] | $f$ [GHz] | $G_{max}$ [dBi] | $\theta_B$ | $\theta_{3\,dB}$ |
|---|---|---|---|---|---|
| 64.0 | 153.5 | 3.4 | 39.8 | 2.5° | 1.9° |
| | | 3.8 | 40.8 | 2.5° | 1.7° |
| | | 4.2 | 41.6 | 2.5° | 1.5° |
| 0.0 | 193.0 | 3.4 | 40.0 | 0.0° | 1.9° |
| | | 3.8 | 40.9 | 0.0° | 1.7° |
| | | 4.2 | 41.8 | 0.0° | 1.5° |
| 100.0 | 193.0 | 3.4 | 39.4 | 3.8° | 1.9° |
| | | 3.8 | 40.3 | 3.8° | 1.7° |
| | | 4.2 | 41.0 | 3.8° | 1.6° |
| 141.4 | 193.0 | 3.4 | 38.9 | 5.4° | 2.0° |
| | | 3.8 | 39.6 | 5.4° | 1.8° |
| | | 4.2 | 40.2 | 5.5° | 1.7° |

The simulations confirm that a multi-feed camera is a very efficient method to increase the aperture of the detector system. The main parameters of the radiation patterns are summarised in Tab. 5.2.

In reality, the levels of the side lobes are expected to be slightly larger due to the scattering of the radiation on the camera body, support struts and reflector gaps. The primary feed patterns are also not expected to be ideally Gaussian and are further modified due to the structure of the camera body and the neighbouring feed horns. Still, direct measurements of the main lobes of the radiation patterns with an airborne microwave emitter are in good agreement with the simulations down to a level of −10 dB, see § B.4.

*Estimate of end-to-end system temperature*

The end-to-end noise temperature of the system is one of the crucial parameters determining the sensitivity of the detector. The temperature of the receiver electronics chain $T_{rx}$ was measured to be in the range of 42 K to 52 K, see § 5.1.5. In the end-to-end system temperature, the noise power received by the LNB from external sources $T_{ext}$ is also included. While most of the received power originates from the observed sky (equivalent noise temperature $T_{sky}$), due to spillover, part of the surrounding environment also contributes with an equivalent noise temperature of $T_{ambient} \approx 300$ K. From the above simulations the spillover is estimated to be $f_{spill} \approx 10\,\%$.[1] Without additional RFI sources, the external contribution to the end-to-end system temperature can be approximated by

[1] *About half of the spillover is due to the central hole in the simulated reflector.*

$$T_{ext} = (1 - f_{spill}) \cdot T_{sky} + f_{spill} \cdot T_{ambient}. \tag{5–24}$$

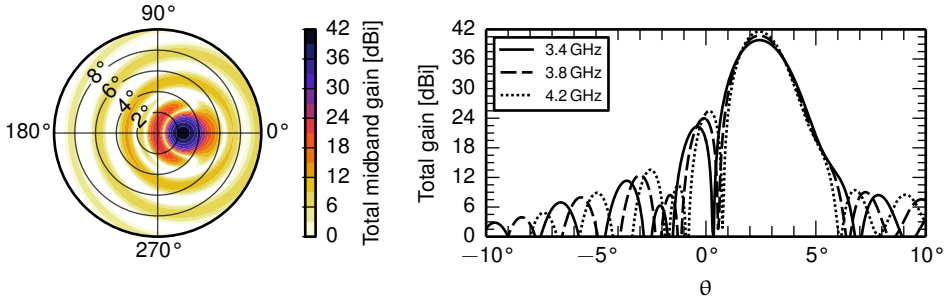


(A) Four feed camera ($\delta$ = 64.0 mm, $r_s$ = 153.5 mm).

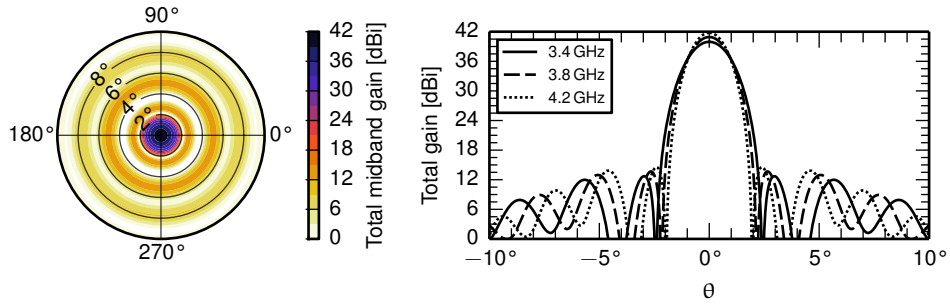


(B) Nine feed camera, central feed ($\delta$ = 0.0 mm, $r_s$ = 193.0 mm).

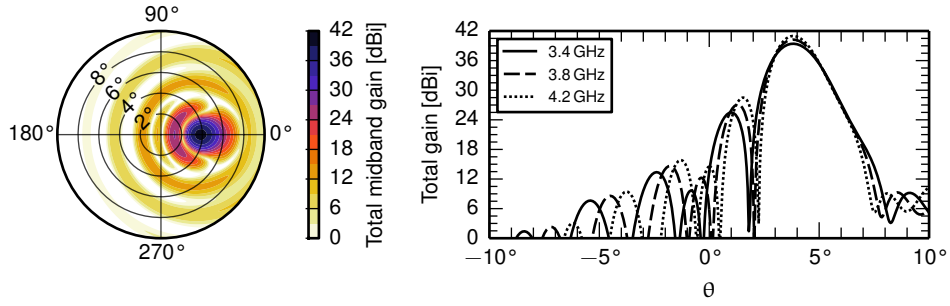


(C) Nine feed camera, edge feed ($\delta$ = 100.0 mm, $r_s$ = 193.0 mm).

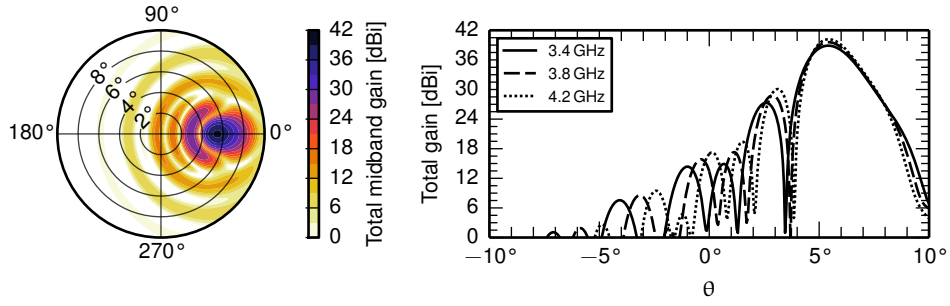


(D) Nine feed camera, corner feed ($\delta$ = 141.4 mm, $r_s$ = 193.0 mm).

FIG. 5.16 • Simulated radiation patterns in two-dimensional polar representation for midband frequency (3.8 GHz, left panels) and spherical cuts along the main lobe segment ($\phi$ = 180° and $\phi$ = 0°) for 3.4 GHz, 3.8 GHz, and 4.2 GHz (right panels). One pattern per feed configuration is shown; other patterns are obtained via rotation in $\phi$. (A) Feed in four feed camera. (B)–(C) Central, edge, and corner feeds in nine feed camera.

For clear sky, $T_{sky} \approx 5\,K$, the external noise contribution is $T_{ext} \approx 35\,K$, yielding an estimated end-to-end system temperature in the range of 77 K to 87 K.

Since the system temperature of the electronics is known from previous measurements, the estimate can be cross-checked using the Y factor method. When covering the entrance window of an LNB that is installed in a camera with a microwave absorber at ambient temperature, the detected noise temperature is approximately $T_{ambient}$. Measuring the power $N_{hot}$ with absorber and the power $N_{cold}$ without absorber, the external contribution to the system temperature can be estimated:

$$Y = \frac{N_{hot}}{N_{cold}} = \frac{T_{ambient} + T_{rx}}{T_{ext} + T_{rx}} \tag{5–25}$$

$$T_{ext} = \frac{T_{ambient} + (1 - Y)T_{rx}}{Y} \tag{5–26}$$

On a day with clear sky the measurement of four channels resulted in Y factors of about 6.5 dB. The corresponding external noise temperature is in the range of 27 K to 35 K, which is in good agreement with the above estimate. We therefore conservatively estimate the end-to-end system temperature of the detector as $T_{sys} = 90\,K$.

## 5.2 GEOMETRY

For defining geometrical cuts and calculating the expected signal for a given KASCADE-Grande shower, the positions and pointing directions of the CROME detectors within the KASCADE-Grande coordinate system are required. To avoid a systematic bias, the accuracy of the position is required to be significantly better than the core uncertainty of the KASCADE-Grande reconstruction (6 m). On the other hand, the accuracy required in determining the pointing must be significantly better than the typical half-power beamwidth of a channel (1.8°) and the typical uncertainty of the arrival direction of the showers reconstructed with KASCADE-Grande (0.8°).

In the first part of the section, the surveys of the antenna positions with a differential GPS system are presented. In the second part, two methods that have been used for estimating the pointing of the individual channels are discussed.

### 5.2.1 *Absolute Positions*

A Magellan ProMark 3 differential GPS system was used to measure the locations of distinct points on the reflectors. A nearby survey point with known coordinates was used as reference and allows the calculation of the reflector locations in the WGS 84 reference system. To calculate the reflector positions relative to the Grande detectors, the corners of three Grande stations and one Piccolo station were also included in the survey.

For each reflector, the locations of the eight segment joints have been measured. The centre and orientation of each reflector aperture have been determined by a numerical least-square fit of a circle in the three-dimensional cartesian space of the local tangent plane (LTP)[m]. The fit residuals are less than

[m] *The local tangent plane is the geodetic coordinate system with* $\mathbf{e}_x$ *pointing east,* $\mathbf{e}_y$ *north,* $\mathbf{e}_z$ *up, and azimuth angles counted counter-clockwise from* $\mathbf{e}_x$ *towards* $\mathbf{e}_y$.

2 cm, demonstrating the good relative precision of the differential GPS system. Repeated surveys on different days (changing ionospheric conditions) and times of day (changing satellite constellations) resulted in variations of ±2 cm in easting, northing, and altitude of the centres, and ±0.3° for the orientations of the fitted apertures. The accuracy of the coordinates is mainly influenced by the accuracy of the survey point that was used as reference. Unfortunately, no uncertainty estimate could be acquired from the land surveying office. Since the typical accuracy of such survey points is in the cm range, we conservatively estimate the total uncertainty to ±10 cm for easting, northing, and altitude. The average WGS 84 coordinates of the reflector centres are given in Tab. 5.3. The fitted orientations are used for estimating the pointing of the channels in the next section.

To calculate the locations of the CROME antennas within the KASCADE-Grande coordinate system, the positions measured for the nearby Grande and Piccolo stations are first used to determine the azimuthal orientation and origin of the coordinate system. Fitting the cartesian coordinates measured in the LTP of the survey point to the coordinates of the same points given in the KASCADE-Grande coordinate system[n] yields four parameters: the azimuthal rotation $\phi_{KG}$ of the KASCADE-Grande coordinate system with respect to geodetic north, and the coordinates of the survey point in the KASCADE-Grande system:

[n] *The list of coordinates was kindly provided by J. Wochele (IKP/KIT).*

$$\begin{aligned} \phi_{KG} &= (15.22 \pm 0.02)^\circ \\ X_{survey} &= (-212.66 \pm 0.04)\,\mathrm{m} \\ Y_{survey} &= (-401.46 \pm 0.03)\,\mathrm{m} \\ Z_{survey} &= (0.20 \pm 0.08)\,\mathrm{m}) \end{aligned}$$

Using these parameters, the coordinates of the reflector centres have been transformed to the KASCADE-Grande coordinate system, see Tab. 5.4. The combined systematic uncertainties are estimated to be ~ 10 cm in X, Y, and Z, respectively.

### 5.2.2 *Pointing*

During installation, the reflectors were aligned using an electronic inclinometer and a pair of binoculars with integrated compass. Both measurements are subject to errors which translate into an uncertainty of the calculated beam directions of a few degrees, too large for our purposes. Hence, two other, independent methods have been used to determine the orientations of the receivers after installation: differential GPS measurements, and direct measurements of the secondary radiation patterns using an airborne C band emitter.

#### *Conventions*

In the local coordinate system of an antenna the aperture is located in the $xy$ plane ($z = 0$). For a nine-feed camera, the central beam points in positive $z$ direction, i. e. along the aperture normal. The camera is oriented with receiver 2 in negative $x$ direction of the centre, i. e. its beam pointing towards positive $x$ (see Fig. 5.15).

The transformation from the local antenna coordinate system to the LTP involves two rotations: a rotation around the local $z$ axis by the camera azimuth angle $\phi_c$, and a rotation by $\theta_a$, the zenith angle of the aperture normal, around the tilting axis $\boldsymbol{\nu}_t$ of the antenna. The tilting axis is perpendicular to $\boldsymbol{e}_z$ and the aperture normal, both defined in the LTP,

$$\boldsymbol{\nu}_t = \begin{pmatrix} -\sin\phi_a \\ \cos\phi_a \\ 0 \end{pmatrix}, \tag{5–27}$$

with $\phi_a$ being the azimuth of the aperture normal. The combined rotation matrix is

$$\mathbf{R} = \begin{pmatrix} \sin^2\phi_a\,(1-\cos\theta_a)+\cos\theta_a & \sin\phi_a\cos\phi_a\,(\cos\theta_a-1) & \cos\phi_a\sin\theta_a \\ \sin\phi_a\cos\phi_a\,(\cos\theta_a-1) & \cos^2\phi_a\,(1-\cos\theta_a)+\cos\theta_a & \sin\phi_a\sin\theta_a \\ -\cos\phi_a\sin\theta_a & -\sin\phi_a\sin\theta_a & \cos\theta_a \end{pmatrix}. \tag{5–28}$$

For analyses in the context of the KASCADE-Grande coordinate system, an additional rotation by $\phi_{KG} = 15.0°$ around $\boldsymbol{e}_z$ has to be taken into account.[o]

[o] *This is the value used in the KRETA framework.*

*Differential GPS measurements*

In the differential GPS surveys described in the previous section, the positions of the outermost points of the segment joints have been measured. A three-dimensional least-squares fit of a circle yields the spherical angles of the aperture normal $\theta_a$ and $\phi_a$. The angular uncertainty estimated from the shape of the minimum of the fit statistics and from repeated measurements is 0.1°. After applying the inverse rotation $R^\top$ (with $\phi_c = 0°$), the azimuth angles of the vectors connecting opposing points are calculated. The azimuth angles modulo 45° typically vary by less than ±0.2°, and hence the azimuthal rotation of the antenna aperture can be calculated with a precision of ~ 0.1°. However, the camera is fixed during installation with a certain mechanical tolerance with respect to the antenna aperture. A (realistic) lateral misalignment of a camera of 5 mm relative to the centre of a reflector, would, for example, result in an angular offset of the boresight axes of all receivers of 0.2°. On the other hand, a rotation of the camera of a few degrees relative to the reflector would be negligible, as the beams point nearly perpendicular to the surface and, hence, cover an angular range of more than 20° in azimuth. From these considerations, the systematic uncertainty in calculating the boresight axes of the beams is conservatively estimated to be 0.5°. The average values of the three pointing parameters are given in Tab. 5.5.

*Flying C band emitter*

Using an airborne microwave emitter, the boresight axes of several beams have been scanned at radial distances of 250 m to 300 m. During flight, the position of the emitter has been measured using the same differential GPS receiver as was

TAB. 5.3 • Centres of the CROME C band reflectors in the WGS 84 reference system. Altitudes are referenced to the ellipsoid. Uncertainties are discussed in the text.

| Antenna | Configuration | Latitude | Longitude | Altitude [m] |
|---|---|---|---|---|
| 1 | all | 49°5′52.3665″ | 8°26′1.8984″ | 160.08 |
| 2 | high pole, vertical | 49°5′52.2472″ | 8°26′1.6457″ | 161.40 |
| | high pole, tilted | 49°5′52.2556″ | 8°26′1.6472″ | 161.37 |
| | short pole, tilted | 49°5′52.2556″ | 8°26′1.6472″ | 160.03 |
| 3 | all | 49°5′52.0435″ | 8°26′1.5496″ | 160.17 |

TAB. 5.4 • Centres of the CROME C band reflectors in the KASCADE-Grande coordinate system. Uncertainties are discussed in the text.

| Antenna | Configuration | X [m] | Y [m] | Z [m] |
|---|---|---|---|---|
| 1 | all | −209.50 | −234.79 | 2.21 |
| 2 | high pole, vertical | −213.48 | −239.69 | 3.52 |
| | high pole, tilted | −213.52 | −239.43 | 3.49 |
| | short pole, tilted | −213.52 | −239.43 | 2.15 |
| 3 | all | −213.71 | −246.27 | 2.29 |

TAB. 5.5 • Antenna geometries from differential GPS measurements. Uncertainties are discussed in the text.

| Antenna | Configuration | $\phi_c$ | $\theta_a$ | $\phi_a$ |
|---|---|---|---|---|
| 1 | initial | 16.3° | 0.1° | 146.3° |
| | realigned | 358.0° | 0.5° | 53.7° |
| 2 | high pole, vertical | 35.4° | 0.3° | 117.2° |
| | short pole, tilted | 83.8° | 13.9° | 83.1° |
| 3 | initial | 87.4° | 14.0° | 266.0° |

TAB. 5.6 • Antenna geometries from measurements with the flying C band emitter. Uncertainties are discussed in the text.

| Antenna | Configuration | $\phi_c$ | $\theta_a$ | $\phi_a$ |
|---|---|---|---|---|
| 1 | initial | 14.40° | 0.33° | 117.29° |
| | realigned | 356.84° | 0.42° | 58.37° |
| 2 | high pole, tilted | 36.54° | 14.72° | 84.91° |
| 3 | initial | 86.63° | 13.79° | 265.75° |

used for the surveys. In an offline analysis, the emitter positions are transformed to the LTP of the antenna and merged with the microwave measurements. The mainlobes simulated with GRASP are fitted to the data to find the direction with the highest gain. The measurements and the analysis are described in detail in App. B. The fitted antenna geometries are listed in Tab. 5.6. The angular uncertainty is expected to be 0.1° (see the discussion in § B.4 for details). The beam directions calculated from these measurements are within 0.3° of those calculated from the differential GPS measurements and, hence, compatible within the uncertainties of both methods.

In further analyses, the beam directions calculated from the measurements with the flying C band emitter are used where available.

## 5.3 STABILITY AND EXTERNAL INTERFERENCE

The average power measured with each receiver of the CROME setup has been observed to change by several dB over time scales of hours. As will be shown, these fluctuations can primarily be attributed to the change of temperature of the housing of an LNB. At the same time, artificial external radio frequency interference (RFI) has been observed to contaminate traces over time scales of a few minutes. The main sources of transients have been identified as the nearby Ångströmquelle Karlsruhe (ANKA) [100], a synchrotron facility with an electron storage ring, and C band altimeter radars of aircrafts crossing the field of view of a receiver.

### 5.3.1 *Temperature Effects and Baseline Stability*

In the following analyses, the temperature measurements of the sensor mounted 2 m above ground on the KIT Campus North weather mast [101], located within 1 km of the antennas, are used.[p] During the operating time of CROME, the ambient temperature ranged from −15 °C to 35 °C, with a mean of about 14 °C. While the detection electronics is housed in an air-conditioned container, the LNBs are subject to the daily and seasonal variations of the outside temperature. Since the average noise power measured with each receiver was found to correlate with the outside temperature, the temperature dependence of the LNB electronics was investigated in a laboratory setup, see § 5.1.5. The temperature coefficient of the conversion gain was found to be of the order of $-0.1\,\mathrm{dB\,K^{-1}}$ which translates to gain changes of −3 dB to +2 dB with respect to the mean operating temperature throughout a year.

[p] *The data was kindly provided by the Institute for Meteorology and Climate Research (IMK/KIT).*

To investigate this effect and smaller effects hidden by the temperature fluctuations, the correlation is analysed for each receiver. For this purpose, data taken during night, between sunset and sunrise, was selected to exclude periods in which the LNBs were heated significantly above ambient temperature by sunlight. Furthermore, periods of precipitation were excluded based on the data from the Campus North weather mast. The correlation of the average noise voltage and the ambient temperature is shown for one channel in Fig. 5.17. A linear model is fitted to the profile of the correlation to obtain the temperature coefficient, typically in the range of $-0.08\,\mathrm{dB\,K^{-1}}$ to $-0.10\,\mathrm{dB\,K^{-1}}$. Excluding

traces contaminated by RFI (see § 5.3.3), the residuals are normally distributed around the model predictions with a standard deviation of about 0.5 dB. This spread is dominated by short-term gain fluctuations and the statistical uncertainty in determining the average voltages from the short traces. No drift of the average noise level relative to the model predictions could be observed. This indicates that the system (noise) temperature of the detector has been stable during the selected periods.

Including also the data taken during daytime and periods of precipitation, tails of the residuals to higher noise powers emerge. The following effects have been observed: 1) On sunny days, the LNBs are heated by the sunlight. The observed noise levels are fully compatible with the expected increase in temperature. 2) For cloudy sky and periods of light rain, the noise levels are typically increased by a few tenths of dB. 3) During periods of heavy rainfall or snowfall, noise levels up to 6 dB higher than usual have been observed. An example for this effect is shown in Fig. 5.18, in which the average noise level of a single receiver is shown as a function of time during December 2011 together with the model prediction. During a period of heavy snowfall on 21$^{st}$ December, the noise level increased by ~ 1.5 mV (6 dB) relative to the model prediction. For further analyses, periods with significantly increased noise levels like these are excluded (see § 5.3.3).

### 5.3.2 *Transient Background*

The frequency band from 4.2 GHz to 4.4 GHz is reserved for radio altimeters, typically used in larger aircrafts in the form of frequency-modulated continuous-wave (FM-CW) radars [102]. This frequency range partly overlaps with the sensitivity range of the Norsat LNBs (cf. § 5.1.5). Since these radars operate at relatively low power levels, their signals are only detected when an altimeter equipped aircraft crosses the field of view of a receiver within a few degrees. The passage typically lasts several minutes and can be identified by an increased average noise level. To suppress the interference, a high-pass filter was added to the detection electronics, see § 5.1.4. The effect of the filter is illustrated in Fig. 5.19, in which the average trace voltage is shown for one channel as a function of time before and after the installation of the filter. With the high-pass filter, the amplitudes of the interferences (visible as spikes in the baseline) have been significantly reduced. As a result, the interference is attenuated below the thermal noise level of the detector most of the time and, if detectable, contaminates fewer channels at a time.

RFI with a signature very different to radio altimeters was found to correlate with the beam injection periods of the ANKA synchrotron facility [100], which is located at a distance of about 400 m to the CROME site. In Fig. 5.20, an example of a trace contaminated with transients of microsecond duration visible in several channels is shown. At the time the traces were recorded, particles were being injected into the storage ring of ANKA. Also the Grande detectors next to the facility are frequently triggered by the injections and also during normal operation of the accelerator [103]. Several methods to identify events induced by ANKA have been developed and included in the Grande reconstruction

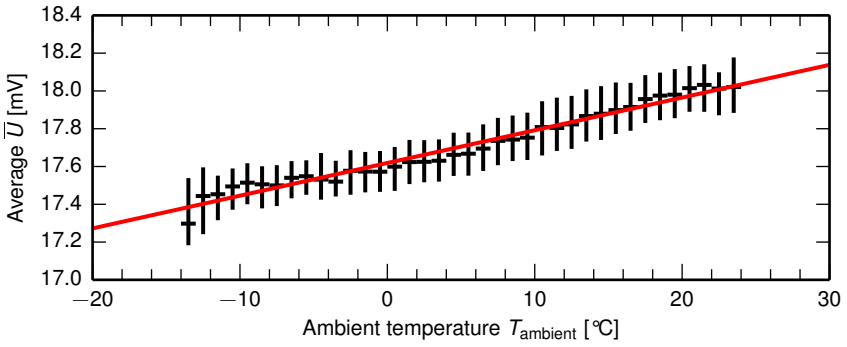


FIG. 5.17 • Profile plot of the average noise level as a function of ambient temperature for one receiver (black crosses) during 358 nights of operation without precipitation. The 68 % intervals around the median values are indicated by error bars. A line, shown in red, is fitted to the profile to determine the temperature coefficient of the conversion gain of the receiver.

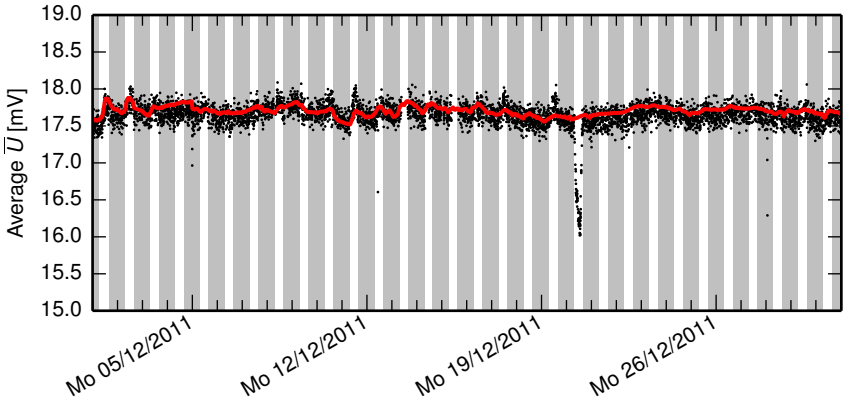


FIG. 5.18 • Average noise level as a function of time for one receiver in December 2011 (black points). Nights are indicated by grey shaded regions. The noise level predicted by the linear model shown in Fig. 5.17 is shown as red line. On 21st December, the noise level was increased significantly during heavy snowfall.

procedure, see e. g. Ref. [104]. Applying the same methods, artificial air shower events are efficiently discarded also from the CROME dataset. However, a handful of microwave signals which apparently did not trigger the Grande detectors remain in the dataset.

### 5.3.3 *Identification of Contaminated Events*

To identify and remove the remaining events taken in periods of heavy precipitation or traces contaminated with RFI we exploit the observation that, during normal operating conditions, the average $\overline{U}$ and the standard deviation $\sigma_U$ of a fast envelope trace are linearly correlated. For a fixed temperature and no external interference the two trace statistics are approximately distributed as a bivariate normal, with a spread due to the randomness of the thermal background and measurement uncertainties. For a given temperature, events contaminated with RFI can therefore be identified as outliers from the observed distribution. Taking changing temperatures and therefore LNB gains into account, events without external interference are located within an elongated ellipse in the $(\overline{U}, \sigma_U)$ space, see Fig. 5.21.

To calculate a measure for the likelihood of an event being contaminated by RFI, the covariance matrix in the three-dimensional space of $(\overline{U}, \sigma_U, T_{\text{ambient}})$ is calculated.[q] For this, the FastMCD algorithm [105] is applied to the complete dataset of each receiver configuration, yielding a robust estimate of the location vector $\boldsymbol{\mu}$ and covariance matrix $\boldsymbol{\Sigma}$, unaffected by outliers. The Mahalanobis distance

$$D = (\mathbf{x} - \boldsymbol{\mu})^{\top} \boldsymbol{\Sigma}^{-1} (\mathbf{x} - \boldsymbol{\mu}), \tag{5–29}$$

of an event with the vector $\mathbf{x}$ is then used to identify and remove outliers from the dataset. Events which are not affected by RFI or heavy rainfall are assumed to be located within the ellipsoid defined by $D = 14.16$, the equivalent of $3\,\sigma$ for a univariate Gaussian distribution.[r] In Fig. 5.21, the projection of the ellipsoid is indicated by a black line. About 3 % of the traces are removed due to this cut.

[q] *$\overline{U}$ and $\sigma_U$ are calculated outside the time window in which a signal from an air shower would be expected (see § 6.1.2).*

[r] *The cut value is calculated from the cumulative distribution function of the $\chi^2(k = 3)$ distribution.*

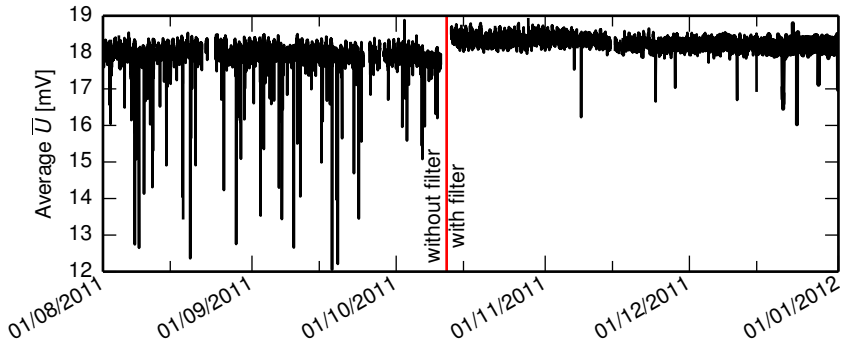


FIG. 5.19 • Average noise level of one channel over a period of five months. External interferences, which are mainly attributed to radio altimeters, are visible as negative spikes due to the negative slope of the transfer function of the logamp. The amplitudes of the altimeter signals could be significantly reduced with the installation of a high-pass filter, the installation date being indicated by a red line. The average noise power decreases due to the reduction of the detector bandwidth from 955 MHz to 660 MHz, see § 5.1.5.

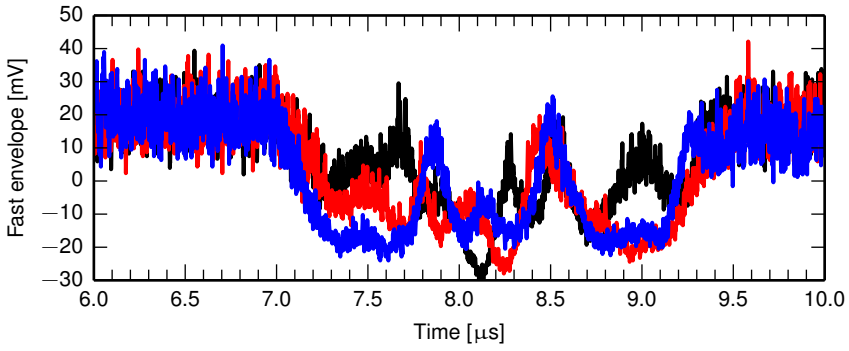


FIG. 5.20 • Detail of a fast envelope trace contaminated with a transient visible in several channels. Events with this signature are correlated with the operation times of the nearby ANKA synchrotron facility.

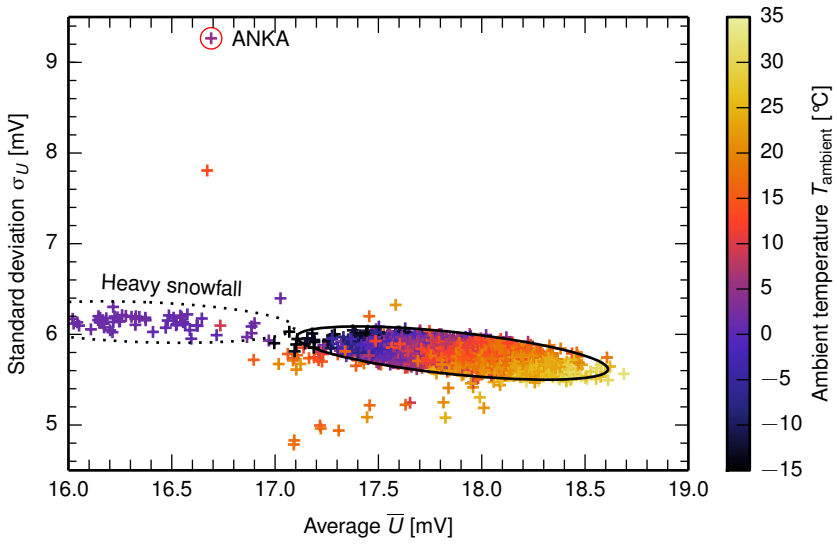


FIG. 5.21 • Correlation of the standard deviation and the average of a sample of the fast envelope traces collected with one receiver. The ambient temperature during data taking is indicated by a colour code. The decrease in noise power (increase in average voltage) with increasing temperature is due the temperature-dependent LNB gain. In normal operating conditions, the standard deviation and the average are linearly correlated. The projection of the fitted error ellipsoid in the $(\overline{U}, \sigma_U, T_{ambient})$ space is shown as black line. Events located outside the ellipsoid are regarded as contaminated with RFI or otherwise taken under bad conditions. The trace of the event marked by a red circle is shown in Fig. 5.20. The outliers in the region marked by the dotted ellipse are the result of the heavy snowfall on 21$^{st}$ December 2011, see also Fig. 5.18. Events with abnormally low averages and standard deviations are typically caused by narrow band noise.

# 6 DATA ANALYSIS AND SIMULATION

For an efficient analysis of the measurements, selection criteria have to be developed to discriminate potential event candidates from background fluctuations. In the first section of this chapter, the selection criteria used in the analysis of the CROME measurements are introduced together with a study of the expected number of background events. For the following analyses, an event selection with a high purity is devised. The properties of the air shower events for which signals have been measured are presented and the event distributions and detected amplitudes are compared to expectations from two models for the emission mechanism.

## 6.1 EVENT SELECTION

The following analyses are based on the data of about 10 000 hours of operation between 4$^{th}$ May 2011—after the last upgrade of the data acquisition electronics—and 10$^{th}$ August 2012.[a] The trigger configuration, a coincidence of the 12 stations forming the three inner Grande hexagons, already applies a preselection biased towards higher energy air showers. In this section, the selection criteria applied in the offline processing of the data are discussed.

[a] *The remaining three months of data until the shutdown of Grande were missing the calibration for Grande events until recently and are yet to be analysed.*

### 6.1.1 *KASCADE-Grande Selection*

The GPS-derived timestamps for each trigger are matched to KASCADE-Grande events and the corresponding CROME voltage traces, detector description, and KASCADE-Grande reconstruction variables are merged into a ROOT-based [106] data storage tree. Selection 8 of the KASCADE-Grande reconstruction, containing all events with at least one 7/7 station trigger, based on KRETA v1.18/05 is used. For further analyses, the cuts listed in Tab. 6.1 are applied to select air showers with a high data and reconstruction quality.

In the data period spanning 464 days, the common operation time of CROME and KASCADE-Grande amounts to about 10 000 hours. The down-time of 10 % was mainly due to restarting the KASCADE-Grande and CROME DAQs, maintenance work, calibration measurements, and the installation of upgrades. The time evolution of the monthly trigger rate is shown as a black histogram in Fig. 6.1. Except for May 2011, in which the Grande trigger was not configured for full efficiency for inclined air showers, the trigger rate was stable at 20 000 to 25 000 per month. A total of 334 929 Grande triggers have been recorded, corresponding to an average of 722 triggers per day or one every two minutes. The fraction of events successfully merged with KASCADE-Grande data and passing the KASCADE-Grande quality cuts, indicated by red circles in Fig. 6.1, is about 22 %.

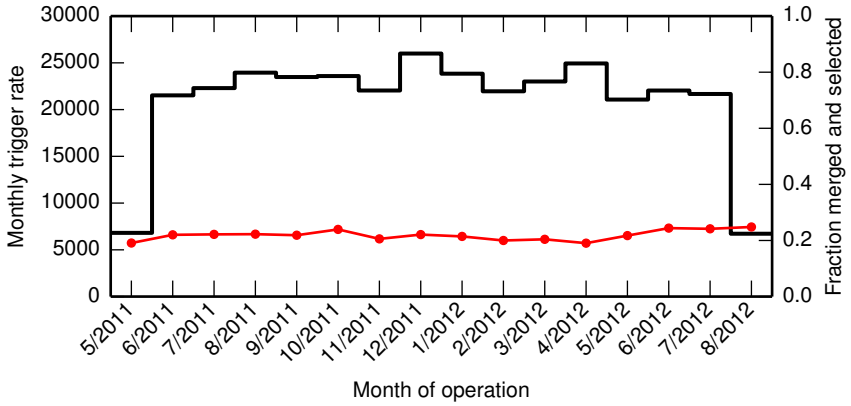


FIG. 6.1 • Monthly trigger rate (black histogram, left scale) as a function of time from 4$^{th}$ May 2011 to 10$^{th}$ August 2012. The fraction of events successfully merged with KASCADE-Grande showers and passing the quality cuts (see Tab. 6.1) is indicated by red dots (right scale). The sharp increase of the Grande trigger rate between May and June 2011 is due to extending the coincidence time window of the trigger to increase the efficiency for inclined showers. The fraction of high-quality events was not affected by the change.

TAB. 6.1 • List of KASCADE-Grande quality cuts used in the event analysis (based on the work of F. Cossavella [77] and D. Kang [107] with an additional energy threshold).

| Description | Condition |
|---|---|
| Rejection of ANKA induced events | $\texttt{FANKA} < 4$ |
| KASCADE data present | $(\texttt{IACT} \,\&\, 1) == 1$ |
| 7/7 stations trigger | $\texttt{HIT7} > 0$ |
| Station with max. deposit within array | $\texttt{IDMX} > 0$ |
| Successful reconstruction | $\texttt{NFLG} > 0$ |
| | $\texttt{NDTG} > 11$ |
| Valid shower parameters | $-0.385 < \texttt{AGE} < 1.485$ |
| | $\texttt{SIZMG} > 1111$ |
| | $\texttt{SIZEG} > 11111$ |
| | $\log_{10}(\frac{\texttt{NCTOT}}{8.5}) > \frac{2.9\log_{10}(\texttt{SIZEG})-8.4}{4.2}$ |
| Energy threshold | $E_0 > 10^{16.0}$ eV |
| Zenith angle limit | $\theta < 40°$ |
| Fiducial area | $-440\,\text{m} < X_{cg} < -50\,\text{m}$ |
| | $-550\,\text{m} < Y_{cg} < -30\,\text{m}$ |

### 6.1.2 *Timing Calculation*

To efficiently separate event candidates from the noise background, the expected time of arrival of the microwave signal is calculated relative to the trigger time of the CROME DAQ (called CROME time frame in the following). This is particularly important since, depending on the shower geometry, a signal can be as short as a few nanoseconds in a trace of 20 µs length. The calculation takes into account the geometry of an air shower relative to the field of view of the individual microwave receivers and the time delays of the signal propagation in the atmosphere and in the electronic components. Considering uncertainties of the shower and detector geometries, the extended field of view of a receiver and unknown production height of a signal, and uncertainties in the propagation delays, the expected time of arrival of a microwave signal is expanded to a time window with a width of several tens of nanoseconds.

The KASCADE-Grande and CROME DAQs were not synchronised directly and the shower reconstruction does not provide an absolute timestamp for the arrival of the shower particles with the required precision. Therefore, two steps are required for each event before calculating the signal time window in the CROME time frame: 1) calculation of the time of the core impact in the KASCADE-Grande time frame, and 2) synchronisation of the KASCADE-Grande time frame with the CROME time frame.

*Time of impact in KASCADE-Grande time frame*

The arrival time of the logic trigger of each Grande station is recorded relative to the first 4/7 station coincidence in an air shower event. To calculate the time of impact of the shower core $t_{impact,KG}$, a thin, plane shower front of ultra-relativistic particles is assumed. In this model, the trigger time of the $i^{th}$ Grande station $t_{i,KG}$ is given by

$$t_{i,KG} = t_{impact,KG} + \frac{(\mathbf{r}_{core} - \mathbf{r}_i) \cdot \hat{\mathbf{n}}_{shower}}{c_0} \tag{6–1}$$

with $\mathbf{r}_{core}$ being the reconstructed position of the shower core, $\mathbf{r}_i$ the position of the $i^{th}$ Grande station, and $\hat{\mathbf{n}}_{shower}$ the reconstructed arrival direction of the shower.

The assumption of a thin, plane shower front is best satisfied near the shower core, i. e. for the station with the highest energy deposit, commonly called hottest station. To estimate the uncertainty of deriving $t_{impact,KG}$ from the hottest station alone, showers with core positions equidistant, within the core uncertainty, to two stations in the shower plane were selected. The distribution of the differences of the impact times calculated for the two stations are shown in Fig. 6.2. The distribution is peaked at 0, with 95 % of the time differences being less than ±13 ns. The distribution exhibits outliers up to ±1.5 µs, mainly due to multiple hits in a scintillator within the coincidence time window. Assuming an equal contribution of each station to the errors, the $95^{th}$ percentile of the uncertainty on $t_{impact,KG}$ is $\sigma^{95}_{impact,KG} = {}^{13\,ns}/_{\sqrt{2}} \approx 9$ ns.

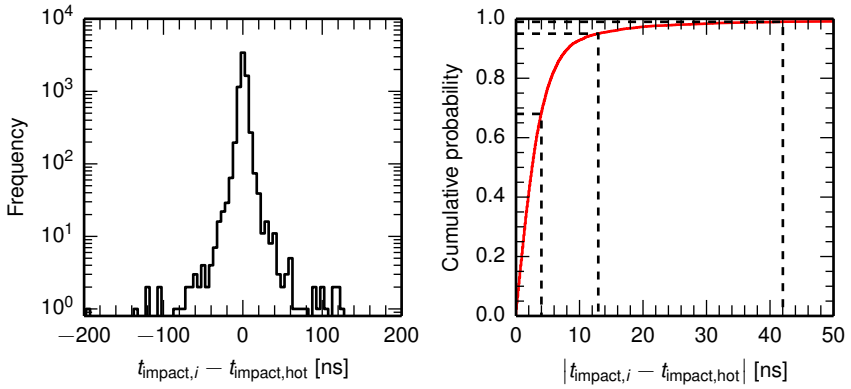


FIG. 6.2 · Distribution of the difference between the time of impact of the shower core derived from the hottest station and a second Grande station equidistant to the shower core (within the core uncertainty). Note the logarithmic scale in the left panel. The cumulative probability distribution is shown in the right panel, with the $68^{\mathrm{th}}$, $95^{\mathrm{th}}$ and $99^{\mathrm{th}}$ percentiles, 4 ns, 13 ns, and 42 ns, respectively, marked by dashed lines.

*Synchronisation of the time frames*

The time frames of KASCADE-Grande and CROME are synchronised using the common measurement of the trigger signal of Grande station 19. For this, the logic signal of the station was routed to the CROME DAQ and digitised for each trigger. With the arrival of the rising edge of the logic signal of station 19 in the CROME time frame $t_{19,\mathrm{CROME}}$, the time of impact of the shower core is

$$t_{\mathrm{impact,CROME}} = t_{\mathrm{impact,KG}} - t_{19,\mathrm{KG}} + t_{19,\mathrm{CROME}} - \tau_{19}. \tag{6–2}$$

The additional delay $\tau_{19}$ between the arrival of a particle in the scintillators of the station and the detection of the rising edge of the logic signal in the CROME DAQ is taken into account. The components contributing to $\tau_{19}$ are listed in Tab. 6.2 along with estimated uncertainties. The event-to-event fluctuations are expected to be about $\sigma_{\tau_{19}} = 9$ ns (see Tab. 6.2).

*Calculation of the signal time window*

The time $t_{\mathrm{signal,CROME}}(h)$ at which a microwave signal emitted by an air shower at height $h$ is expected to be visible in a digitised trace is calculated via

$$t_{\mathrm{signal,CROME}}(h) = \tau_{\mathrm{signal}}(h) - \tau_{\mathrm{core}}(h) + t_{\mathrm{impact,CROME}} + \tau_{\mathrm{RF}}, \tag{6–3}$$

with:

- $\tau_{\mathrm{signal}}(h)$: time of flight of the microwave signal from the shower at height $h$ to the microwave detector,

$$\tau_{\mathrm{signal}}(h) = \left| \mathbf{r}_{\mathrm{core}} + \frac{h}{\cos\theta} \cdot \hat{\mathbf{n}}_{\mathrm{shower}} - \mathbf{r}_{\mathrm{det}} \right| \cdot \frac{n_{\mathrm{eff}}(h, h_{\mathrm{det}})}{c_0}, \tag{6–4}$$

TAB. 6.2 • Contributions to the time delay $\tau_{19}$ between the arrival of a particle in the scintillators of a Grande station and detection of the rising edge of the logic signal in the CROME DAQ before and after installation of an additional discriminator on 2nd August 2011. Conservative estimates for the event-by-event and systematic uncertainties are given.

| | Delay [ns] | | Uncertainty [ns] | |
|---|---|---|---|---|
| Component | Before 2/8/11 | Since 2/8/11 | Stat. | Syst. |
| Scintillator and PMT* | 44 | 44 | 5 | 10 |
| Station electronics* | 47 | 47 | 5 | 5 |
| Trigger cable | 3075 | 3075 | 5 | 5 |
| DAQ electronics | 0 | 104 | 2 | 5 |
| Edge detection | 38 | 3 | 1 | 2 |
| Total | 3204 | 3273 | 9 | 13 |

* Estimated from datasheets.

with $\theta$ being the zenith angle of the shower, $n_{\text{eff}}$ the effective refractive index between the height $h$ and the detector height $h_{\text{det}}$, and $c_0$ the speed of light in vacuum. The refractive index $n$ at height $h$ is taken from Ref. [108],

$$n(h) = 1 + 2726.43 \times 10^{-7} \cdot \frac{p(h)}{p(0)}, \tag{6–5}$$

with the atmospheric pressure profile $p(h)$ of the U.S. Standard Atmosphere calculated from Linsley's parametrisation [21].[b] The effective refractive index is calculated from

$$n_{\text{eff}}(h, h_{\text{det}}) = \frac{1}{h - h_{\text{det}}} \int_{h_{\text{det}}}^{h} dh' \, n(h') \tag{6–6}$$

[b] *Using this approximation, the fractional part of $n$ is within 1 % of current models for the microwave refractive index, see e. g. Ref. [109], for a dry and isothermal atmosphere.*

- $\tau_{\text{core}}(h)$: time of flight of the shower core from height $h$ to ground:

$$\tau_{\text{core}}(h) = \left| \mathbf{r}_{\text{core}} + \frac{h}{\cos\theta} \cdot \hat{\mathbf{n}}_{\text{shower}} \right| \cdot \frac{1}{c_0} \tag{6–7}$$

- $\tau_{\text{RF}}$: delay of the microwave signal due to cable and electronics delays in the CROME DAQ

A signal is expected for the time span in which the shower is in the field of view of a receiver channel. To obtain an upper estimate for the time window in which a signal could be expected, the field of view of a receiver is approximated by a cone with 4° (full) opening angle and the intersection points between the shower axis and the cone define the signal time window. For showers starting within the field of view of a receiver, the expected signal time at 10 km height is used.

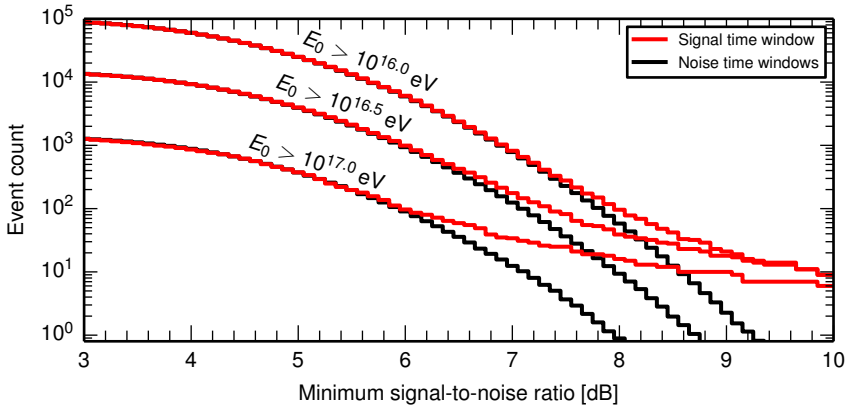


FIG. 6.3 • Number of traces exceeding the minimum signal-to-noise ratio in the expected signal time window (red lines) and in the shifted time windows used for the background estimate (black lines, averages) for three thresholds on the shower energy. A clear excess of the number of events relative to the background is observed for large signal-to-noise ratios. The relative excess increases with shower energy, which is expected for microwave signals emitted by air showers.

*Propagation of uncertainties*

For a conservative search for a microwave signal the time windows are extended to include 95 % of the expected event-by-event fluctuations. The event-by-event uncertainty is dominated by the uncertainty in deriving the impact time, the expected fluctuations of the electronics delay, and the uncertainty of the air shower geometry relative to the position and pointing of the receiver. For calculating the latter, geometrical uncertainties are propagated using a Monte Carlo simulation fluctuating the core position, arrival direction, and beam axis within the respective uncertainties. The lower and upper edges of the signal time window are then chosen to contain 95 % of the fluctuated time windows and extended by $\sqrt{(\sigma^{95}_{\mathrm{impact,KG}})^2 + 4\sigma^2_{\tau_{19}}} = 20\,\mathrm{ns}$. The resulting signal time windows are typically between 40 ns and 60 ns long, depending mainly on the impact parameter of the air shower.

In addition to the broadening of the signal time windows due to the event-by-event uncertainties, microwave signals can be systematically shifted within the systematic uncertainties of the time delays $\tau_{19}$ (13 ns) and $\tau_{\mathrm{RF}}$ (~ 5 ns).

### 6.1.3 *CROME Quality Cuts and Event Rates*

The signal time window for each receiver channel is calculated for all showers passing the KASCADE-Grande quality cuts. For this, the shower is required to pass the field of view of the microwave receiver within an observation angle of $\theta_{\mathrm{obs}} < 2°$. The cut is softened by the propagation of the geometric uncertainties discussed above: the trace is selected when more than 10 % of 1000 fluctuated shower geometries cross the field of view of the receiver within 2°. Each trace is additionally classified in terms of the RFI contamination and the stability of the operating conditions. For this, the Mahalanobis distance D of the vector

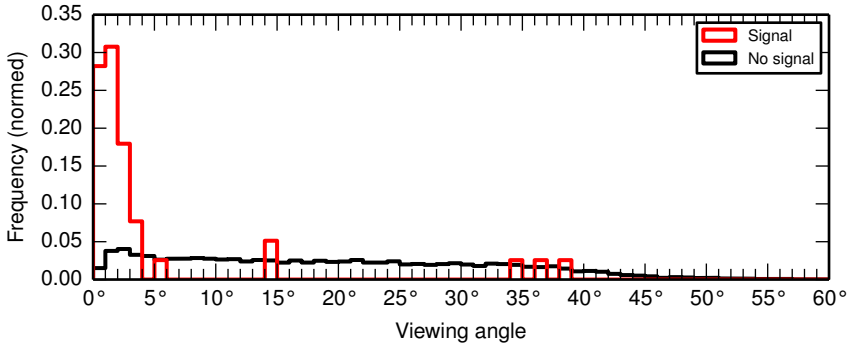


FIG. 6.4 • Distribution of the viewing angles for showers with energies greater than $10^{16.5}$ eV. Events with a microwave signal greater than 8 dB in the expected signal time window are contained in the red histogram, all other events in the black histogram. To increase the selection purity for the analyses of the event properties, events with viewing angles greater than 4° are later rejected in the analysis.

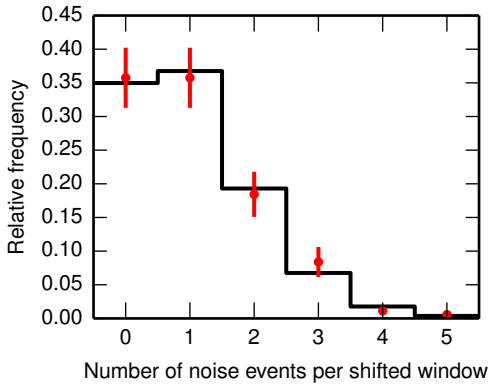


FIG. 6.5 • Distribution of the noise rate for the 179 time windows adjacent to the time window in which a signal from an air shower would be expected (red points, error bars are calculated from Poisson statistics). A signal-to-noise threshold of 8 dB is applied. The distribution is well described by a binomial distribution with the proportion p = 1.05, shown as black line.

TAB. 6.3 • List of CROME quality cuts for the high-purity selection. For each cut, the number of air shower events and the total number of active microwave receivers after applying the cut are given.

| Description | Condition | Showers | Channels |
|---|---|---|---|
| KASCADE-Grande cuts | see Tab. 6.1 | 73 188 | 1 624 942 |
| Stable operation with no RFI | $D < 14.16$ | 72 852 | 1 577 220 |
| Shower passes field of view | $\theta_{obs} < 2°$ | 19 341 | 101 066 |
| Energy threshold | $E_0 > 10^{16.5}$ eV | 2888 | 15 119 |
| Viewing angle limit | $\theta_{view} < 4°$ | 1024 | 1936 |
| Signal-to-noise threshold | SNR > 8 dB | 31 | 33 |

$(\overline{U}, \sigma_U, T_{ambient})$ is required to be less than 14.16. This cut removes periods of heavy rain, RFI from aircraft altimeter radars, and signals induced by the ANKA synchrotron light source (see § 5.3.3 for details). A total of 100 906 traces for 19 312 air shower events are selected by these cuts.

To select traces containing a signal emitted by an air shower, a cut on the signal-to-noise ratio, $SNR_{min}$, is applied. The signal-to-noise ratio is calculated by dividing the peak power in the expected signal time window by the average power outside the signal time window and is expressed in dB due to the logarithmic detector curve. Counting the number of traces with a signal-to-noise ratio greater than $SNR_{min}$ yields the number of event candidates.

To estimate the significance of an observed number of event candidates, the background rate is calculated by applying the same analysis to time windows of the same length as the expected signal time window, but with a systematic *shift*. For 179 shifted time windows with offsets[c] of $n \cdot 100\,\text{ns}$ ($n = -40 \ldots 139$) with respect to the signal time window, the probability of observing a signal-to-noise ratio greater than $SNR_{min}$, the binomial proportion, is calculated. The 68 % confidence interval for the binomial proportion is estimated using the method proposed by Clopper and Pearson [110].

[c] *100 ns is the minimum time offset to avoid overlapping windows. The limits are given by the earliest and latest signal time window within the 20 µs traces.*

In Fig. 6.3, the number of candidate events (red line) is plotted as a function of $SNR_{min}$ along with the background rate (black line) for three energy thresholds. For all energy thresholds, a deviation of the event rate from the expected background rate is observed above a certain signal-to-noise ratio. As expected for signals emitted by air showers that increase in signal strength with energy, the deviation is observed at lower signal-to-noise ratios for increasing shower energies. The maximum observed signal-to-noise ratio outside the signal time window is 10.7 dB. A total of nine events exceeding this signal-to-noise ratio in the signal time window have been observed.

To obtain a dataset with relatively large statistics and purity, the minimum required signal-to-noise ratio is selected as $SNR_{min} > 8\,\text{dB}$ for an energy threshold of $E_0 > 10^{16.5}\,\text{eV}$. In total, 39 receiver channels from 37 air shower events satisfy these selection criteria with an expected background of $9.4 \pm 0.2$ channels.

To improve the purity of the selection, an additional cut on the viewing angle—the angle between the boresight axis of the microwave receiver and the air shower axis—is applied. It stems from the observation that most (all) of the air showers with signal-to-noise ratios greater than 8 dB (9 dB) are nearly parallel to the boresight axis of the detecting receiver, see Fig. 6.4. The interpretation of this observation is discussed below in detail. Selecting only showers with viewing angles less than 4°, the event count decreases to 33 channels in 31 air shower events. At the same time, the expected background drops significantly to $1.05 \pm 0.08$ channels.

To crosscheck the estimate of the expected number of background events, it was additionally calculated separately for each offset of the time window. The distribution of the number of background events in the 179 offset windows is compatible with a binomial distribution with the proportion $1.05 \pm 0.08$, see Fig. 6.5. Hence, the same underlying distribution is assumed for the actual signal time window and less than 2 (4) background events are expected with 68 % (95 %) confidence level (CL). This high-purity event selection, summarised also

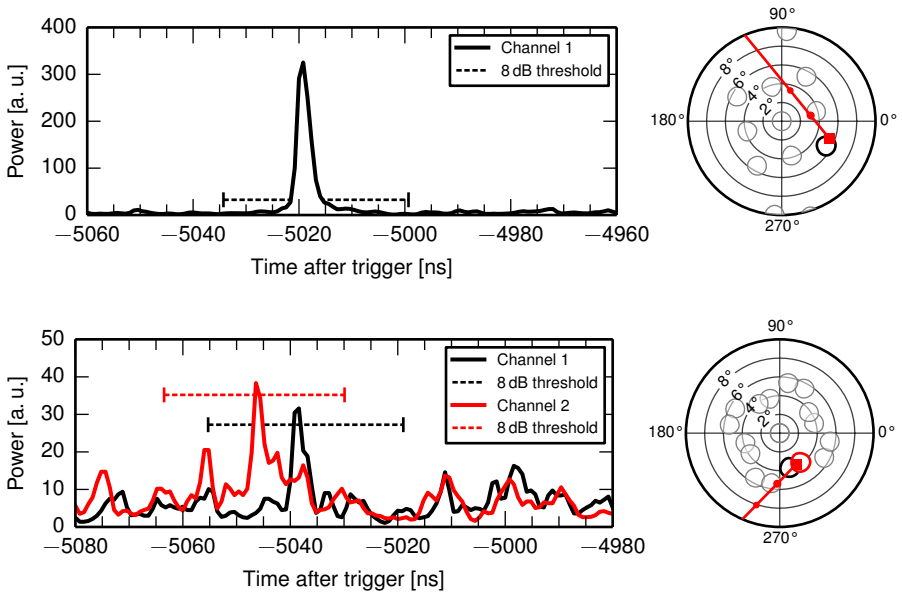


FIG. 6.6 • Power traces (left) and geometry (right, geographic coordinates) of two air shower events: the event with the highest observed signal-to-noise ratio of 17.7 dB (top panels), and one of the stereo observations (lower panels). The thresholds on the signal amplitude within the signal time window are indicated by dashed lines in the left panels. The geometry of each event is shown as polar plot, with the shower track (red line), the fields of view of the receivers with signal (circles with the same colour code as in the left panel), and the fields of view of the receivers without a signal (grey circles). The start of the shower track at 20 km, and two additional altitudes, 2 km and 1 km, are marked with a square and circles, respectively.

in Tab. 6.3, is used for the following analyses of the properties of the observed air shower events.

## 6.2 EVENT PROPERTIES

For the selection presented in the previous section, microwave signals have been found for 31 air showers. In most of the air shower events a signal was detected only in one receiver although the shower axis typically crossed the fields of view of two to three receivers. Consistently, the receivers viewing the air shower at high altitudes, usually above 2 km and near the expected shower maximum, detected a signal. Only two air showers were each detected in two independent receivers. The signal traces of the event with the highest signal and for one of the stereo events are shown in Fig. 6.6. The absolute timing is well within the expected time window and, for the stereo events, the relative delay between the pulses is in good agreement with the expected geometric delays. The detected pulses are typically less than 10 ns long. An overview of all detected events is given in App. C.

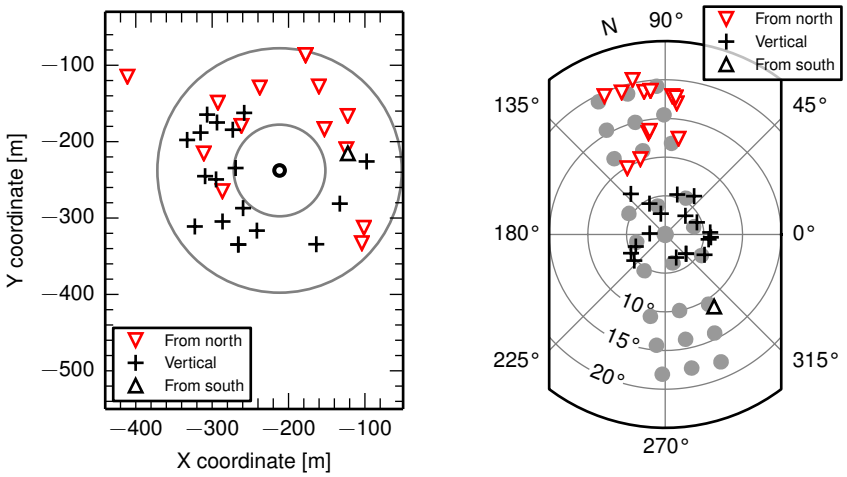


(A) Location of the CROME antennas (black circle) and core positions of the air showers with microwave signals (crosses and triangles) in the fiducial area of the KASCADE-Grande reconstruction. Showers detected with the north pointing, vertical, and south pointing antenna are marked individually. Most of the core positions are distributed on a ring around the antennas, indicated by grey circles (see text).

(B) Arrival directions of the showers with microwave signals (KASCADE-Grande coordinates with geographic north at 105°). The fields of view of the three antennas in their final alignment are indicated by grey circles. The same symbols as in the left panel are used.

FIG. 6.7 • Distribution of the core positions (A) and the arrival directions (B) of the air showers with microwave signals from the high-purity event selection. Both graphs are shown in KASCADE-Grande coordinates.

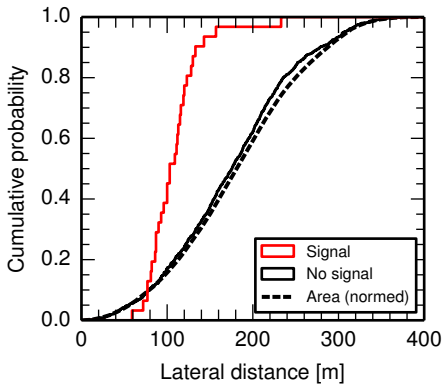


FIG. 6.8 • Cumulative distribution of the lateral distance of the shower core to the antenna position. While the number of showers without a microwave signal (black histogram) is approximately proportional to the fiducial area (dashed line), the showers with microwave signals (red histogram) are distributed on a ring around the detectors.

TAB. 6.4 • Detection rates for air showers with cores within 160 m of the antennas and passing all selection criteria listed in Tab. 6.3. The detection rates are broken down into arrival directions and core locations, see also Fig. 6.7.

| Arrival direction | West of antenna | East of antenna | Total |
|---|---|---|---|
| From north | 4/66 | 8/73 | 12/139 |
| Vertical | 14/127 | 3/109 | 17/236 |
| From south | 0/30 | 1/39 | 1/69 |
| Total | 18/222 | 12/221 | 30/443 |

*Ring structure*

The core positions of the air showers passing all cuts up to the signal threshold are uniformly distributed within the fiducial area of KASCADE-Grande. In contrast, the core positions of the air showers that were detected in the C band are mainly distributed on a ring around the CROME antennas, see Fig. 6.7a. Notably, the core positions of 30 of the 31 detected air showers lie on a ring of 60 m inner and 160 m outer radius. There is a significant deficit of detected air showers outside and inside this ring. To illustrate this further, the cumulative distribution of the lateral distance between the shower core and the antennas is shown for detected and undetected showers in Fig. 6.8. The fraction of showers within 60 m of the antennas relative to the number of showers within 160 m is 14 %. The binomial probability of detecting zero out of 30 showers within 60 m is 1 %.

*East-west asymmetry and geometry dependence*

The detection rates also exhibit two notable asymmetries when calculated for the showers with core locations within 160 m of the antennas, for which the fiducial area is symmetric. First, for the vertically pointing antenna, $11.0\,\%^{+6.8\,\%}_{-4.9\,\%}$ of the showers (14 out of 127) were detected west of the antenna, while only $2.8\,\%^{+5.1\,\%}_{-2.2\,\%}$ (three out of 109) were detected east of the antenna. At the same time, no significant east-west asymmetry can be observed for the showers detected by the antenna pointed north. Second, the rate of detected air showers differs between the three antennas. Specifically, $1.4\,\%^{+6.4\,\%}_{-1.4\,\%}$, $7.2\,\%^{+4.1\,\%}_{-3.0\,\%}$, and $8.6\,\%^{+6.0\,\%}_{-4.1\,\%}$ of the showers within 160 m were detected in the C band with the south, vertical, and north oriented antenna, respectively. This is an indication that the detection probability depends on the shower geometry relative to the local geomagnetic field. The detection rates are tabulated in Tab. 6.4, broken down into arrival directions and core locations.

*Polarisation*

Due to the small exposure collected with the dual-polarised channels, only three of the air shower events were detected while crossing dual-polarised beams. In these events, the signals of only one of the polarisation directions

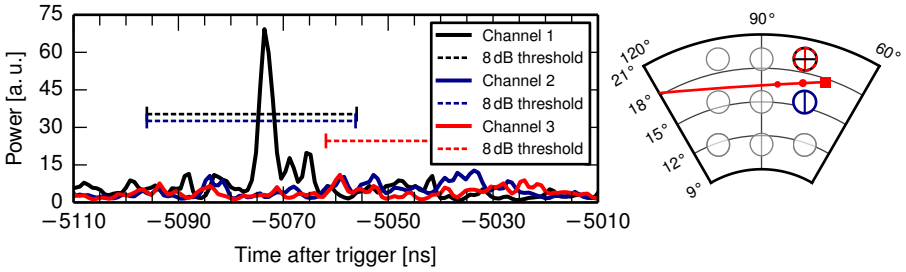


FIG. 6.9 • Power traces (left) and geometry (right, geographic coordinates) of one of the events observed in one polarisation of a dual-polarised receiver. The geometry of the event is shown as polar plot, with the shower track (red line), the field of view of the receiver with signal (black circle), and the fields of view of two cross-polarised receivers viewing the air shower at the same altitude but showing no signal (red dashed and blue circles). The polarisation of each receiver is indicated by a horizontal line (east-west polarised) or a vertical line (north-south polarised). The traces are shown in the same colour code together with the thresholds on the signal amplitude within the signal time windows (dashed lines).

exceed the detection threshold. The most significant of these observations, shown in Fig. 6.9, has a signal-to-noise ratio of 11 dB, while the signal in the same time window of the trace of the cross-polarised channel is at least 6 dB weaker. It is therefore unlikely that the detected radiation was unpolarised.

## 6.3 SIMULATION OF DIFFERENT EMISSION MODELS

In the following, the observations described above will be compared with predictions by two emission models: molecular bremsstrahlung from the low energy electrons of the air shower plasma, and radio emission of the high-energy electrons and positrons in the shower front.

### 6.3.1 *Molecular Bremsstrahlung*

Molecular bremsstrahlung is emitted during the cooling of low energy electrons in a weakly ionised plasma [49]. For the simulation of the radiation, an intensity proportional to the energy deposit in the atmosphere is assumed with a flat frequency spectrum in the C band. The radiation is propagated to the detectors taking into account the effects of the changing index of refraction of the atmosphere.

The atmospheric depth profile $X(h)$ and pressure profile $p(h)$ are calculated using Linsley's parametrisation [21] of the U.S. Standard Atmosphere. Starting at an altitude of 50 km, the shower track is split into segments of 1 m length. For each segment $i$ spanning the shower development from depth $X_i - {}^{\Delta X_i}/_2$ to $X_i + {}^{\Delta X_i}/_2$, the total energy deposit $E^{tot}_{dep,i}$ is calculated using

$$E^{tot}_{dep,i} = \Delta X_i \, N_{ch}(X_i) \, \alpha_{eff}(X_i), \tag{6–8}$$

with the parametrisation of the mean ionisation loss rate $\alpha_{\text{eff}}$ proposed by Nerling *et al.* [111]. A Gaisser-Hillas profile

$$N_{\text{ch}}(X) = N_{\text{max}} \left( \frac{X - X_0 - X_1}{X_{\text{max}} - X_0} \right)^{\frac{X_{\text{max}} - X_0}{\lambda}} e^{\frac{X_{\text{max}} - X + X_1}{\lambda}}, \tag{6–9}$$

is used to describe the longitudinal development of the number of charged particles in the shower. The depth of the first interaction $X_1$, the depth of the maximum of the shower development $X_{\text{max}}$, the maximum number of particles $N_{\text{max}}$, and the shape parameters $\lambda$ and $X_0$ are sampled from distributions obtained from CORSIKA simulations and parametrised by Perrone *et al.* [112]. The total energy $E_{\text{MW},i}$ emitted in microwaves in the bandwidth $\Delta\nu$ is assumed to be proportional to the energy deposit,

$$E_{\text{MW},i} = Y_{\text{MW}} \, E^{\text{tot}}_{\text{dep},i} \, \Delta\nu, \tag{6–10}$$

with the proportionality factor $Y_{\text{MW}}$ [$\text{Hz}^{-1}$] called the *microwave yield* in analogy to the fluorescence yield used for the simulation of the fluorescence emission of air showers. The value of $Y_{\text{MW}}$ is derived below.

The energy is distributed uniformly among $N_{\text{LDF}}$ parallel tracks with radial distances to the shower core drawn from the lateral distribution function proposed by Góra *et al.* [113] using inverse transform sampling. A rotationally symmetric, flat shower disc is assumed. The energy $E_{\text{MW},i}/N_{\text{LDF}}$ is emitted in the time interval $\Delta t_{\text{em}} = 1\,\text{m}/c_0$ in which the shower disc moves along the track. An additional time delay drawn from an exponential distribution with scale parameter $\tau_{\text{plasma}} = 7$ ns is added to the emission times to reproduce the exponential decay of the plasma found in the beam test experiments [48]. The time interval $\Delta t_{\text{det}}$ in which the radiation is received at the location of the detector is calculated by adding the propagation delays $\tau_{\text{signal}}$, see Eq. (6–4), for radiation from the upper and lower edge of the segment, respectively. It is important to note that a realistic refractive index $n > 1$ is used. This leads to a reversal of the time structure of the detected signal if the detector is located inside the Cherenkov cone and a compression of the signal duration, $\Delta t_{\text{det}} < \Delta t_{\text{em}}$, when the detector is located near the edge of the Cherenkov cone. The detected power then becomes

$$P_i = A_{\text{eff}}(\theta_{\text{em}}, \phi_{\text{em}}) \frac{E_{\text{MW},i}}{\Delta t_{\text{det}} \cdot N_{\text{LDF}}} \frac{1}{4\pi R^2}, \tag{6–11}$$

with $R$ being the distance between the detector and the centre of the track, and $A_{\text{eff}}(\theta_{\text{em}}, \phi_{\text{em}})$ the effective area of the detector for radiation originating at the centre of the track. This relation is only valid in the far-field of both the detector and the source. Since the details in the near-field are not known, radiation emitted within 300 m of a detector, the approximate distance to the far-field of the antennas, is not considered.

Finally, the microwave yield $Y_{\text{MW}}$ is derived by simulating the trial shower given in Ref. [48], a vertical $3.36 \times 10^{17}$ eV shower at an observation distance of 10 km, for which the spectral energy flux

$$I_{\text{MBR}} = 2.77 \times 10^{-24}\,\text{W}\,\text{m}^{-2}\,\text{Hz}^{-1} \tag{6–12}$$

TAB. 6.5 · List of parameters for the simulation of conventional radio emission using CoREAS [115].

| Parameter | Value |
|---|---|
| Hadronic interaction models | QGSJet-II.04 [23], FLUKA [19] |
| Thinning level | $10^{-7}$ |
| Atmospheric profile | U.S. Standard |
| Refractive index at ground | $n = 1.000\,292$ |
| Geomagnetic field | $\mathbf{B} = (20.40\,\mu T,\ 0,\ -43.23\,\mu T)$ |
| Time resolution | 0.05 ns ($f_{nyq} = 10\,GHz$) |
| Resolution reduction scale | 0 |

is given. A microwave yield of

$$Y_{MW} = 1.17 \times 10^{-18}\,Hz^{-1} \tag{6–13}$$

reproduces the given spectral energy flux [114].

### 6.3.2 *Conventional Radio Emission*

The dominant part of the radiation emitted by the high-energy charged particles of the shower front arises from the separation of the particles of opposite charge in the geomagnetic field and the resulting induction of a transverse current [34]. The emission due to the variation of the net charge excess, the Askaryan effect, provides an additional component [36]. The resulting radio emission due to these processes was found to be coherent, polarised and forward beamed in the ~ 100 MHz range. After the announcement of the detection of microwave signals from air showers, simulation codes which had been developed to calculate the radio emission in the MHz frequency range have been used to study the emission properties also at microwave frequencies. The CORSIKA-based Radio Emission from Air Showers (CoREAS) simulation code [115] is used for comparisons with the observations. In CoREAS, the motion of each electron tracked by CORSIKA is split into a series of discrete and instantaneous acceleration events, also called *endpoints* [116]. The radiation emitted at each of the endpoints is propagated to the location of the detector and summed coherently, resulting in time traces for each component of the electric field. The relevant parameters chosen for the simulation are listed in Tab. 6.5.

In the following, the radiation of the high-energy charged particles calculated this way will be referred to as *conventional* radio emission.

## 6.4 COMPARISON OF DATA WITH MODEL PREDICTIONS

*Ring structure*

Since the experiment operates at the detection threshold, the distribution of the core positions of detected air showers can be interpreted as an indirect observa-

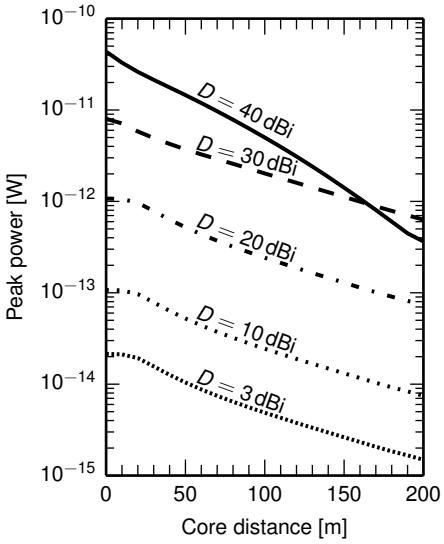


FIG. 6.10 • Expected peak power due to molecular bremsstrahlung as a function of lateral distance for a vertical air shower induced by a $10^{17}$ eV iron primary. The detection with vertically oriented antennas with gains from 3 dBi, observing the whole sky, to 40 dBi, similar to the CROME antennas, and ideal pencil beams was simulated. The received flux is symmetric around the shower axis and decreases monotonically with distance to the shower core. The received power increases linearly with the antenna gain up to about 20 dBi, beyond which large parts of the emitting regions are located outside the field of view.

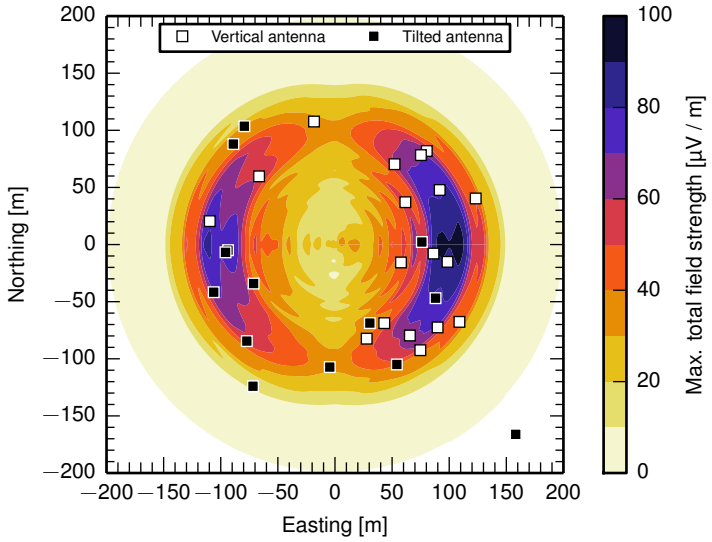


FIG. 6.11 • Ground pattern of the maximum total field strengths between 3.4 GHz and 4.0 GHz predicted by CoREAS for a $10^{17}$ eV iron primary (geographic coordinates). The air shower hits ground vertically at $(0, 0)$. The colour map is overlaid with squares indicating the positions of the CROME antennas relative to the cores of the detected showers.

tion of the flux distribution produced by the dominant emission mechanism at ground. While varying primary energies, primary masses, shower-to-shower fluctuations, and shower geometries together with geometry dependent detector efficiencies complicate the interpretation, broad features like the observed ring structure can still be used to draw conclusions.

The isotropic emission of molecular bremsstrahlung results in a flux distribution at ground that monotonically decreases with increasing distance to the shower axis. This is shown in Fig. 6.10 for a vertical air shower induced by a $10^{17}$ eV iron primary and detected by ideal, vertically-pointing antennas of various gains.[d] Although a boost in signal strength is expected near the Cherenkov angle due to the observation of larger parts of the shower in a small time interval (time compression), the inverse-square law effectively suppresses this effect. Therefore, the deficit of events with core positions close to the antennas cannot be explained with the current understanding of the molecular bremsstrahlung process.

[d] *The monotonically decreasing flux has also been observed in microscopic simulations, see Ref. [49].*

To study the ground pattern of conventional radio emission at GHz frequencies, air showers were simulated using CoREAS with a dense antenna array at ground level. The time traces of the electric fields at each antenna position were filtered to 3.4 GHz to 4.0 GHz to calculate the peak electric field strength in this band. In Fig. 6.11, the results are shown as a colour map for a vertical $10^{17}$ eV shower. The lateral distribution produced by the shower exhibits a clear ring structure with gaps north and south of the shower core. The size of the ring is directly related to the geometric height of the shower maximum above ground and the Cherenkov angle at this altitude [115, 117].[e] Antennas located on this ring observe a large part of the shower in a small time interval which shortens the pulse and therefore extends the coherence of the shower emission to higher frequencies. Note that only the recent inclusion of a realistic refractive index of air in the radio simulations allowed studies of these time compression effects [118].

[e] *The depth of the maximum for the shower shown in Fig. 6.11, 658 g cm$^{-2}$, lies between the average depths of proton and iron induced showers at this energy.*

For a qualitative comparison, the positions of the CROME antennas relative to the core positions of the detected showers are shown as squares in Fig. 6.11. The positions strongly correlate with the regions of large field strengths in the broken ring pattern. The distribution of the detected air showers and the deficit of detected air showers close to the antennas are well reproduced by the predictions of conventional radio emission.

### *Geometry dependent detection rate*

A difference in the event rate between antennas observing different parts of the sky can be linked to an emission mechanism which depends on the shower geometry. The maximum zenith angle of the detected showers is 20°. Therefore, the variations of the emission strength of molecular bremsstrahlung are expected to be small. Moreover, the variations would be symmetric with respect to the vertical axis and therefore could not explain the difference in the detection rate of the south and north pointed antennas.

The intensity of geomagnetic radio emission is proportional to $\sin^2(\alpha)$, with $\alpha$ being the angle between the shower propagation direction and the geomagnetic field, often called geomagnetic angle in this context. At the location of

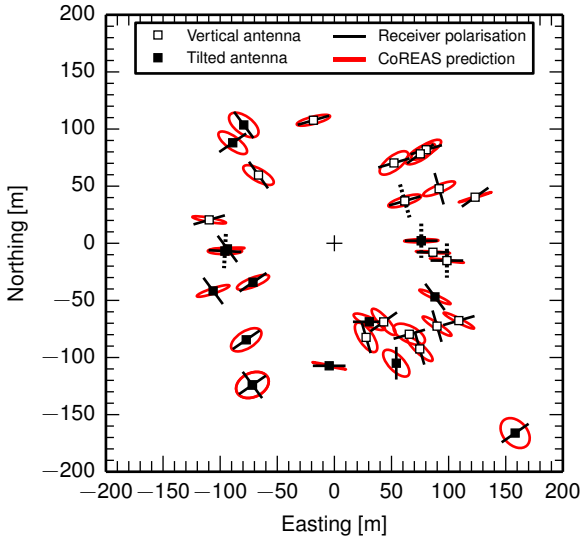


FIG. 6.12 • Positions of the CROME antennas (squares) relative to the core positions of the showers detected in the C band. The polarisation direction of each receiver that detected a signal is indicated by a black line. Additionally, the polarisation axes of the channels of dual-polarised receivers which did not measure a signal are shown as dashed lines. The ellipses drawn by the electric field vector simulated with CoREAS for iron primaries are outlined in red.

CROME, the magnetic inclination is 65°. The central axes of the south, vertical, and north pointing antennas are aligned with an angle of 10°, 25°, and 40° to the geomagnetic field, resulting in $\sin^2(\alpha)$ factors of 0.03, 0.18, and 0.42, respectively. Therefore, the observed differences of the detection rates can be explained naturally within the geomagnetic emission model.

*East-west asymmetry*

A distinct feature predicted for the lateral distribution of conventional radio emission is the higher field strength east of the shower axis, see Fig. 6.11. It arises from the superposition of the geomagnetic and charge excess components of the radiation which add up constructively on the eastern side and destructively on the western side. Since the strength of only the geomagnetic emission depends on the geomagnetic angle, the size of the east-west asymmetry also depends on this angle. It is maximal when the two contributions have similar amplitudes and cancel west of the shower axis. This fits well to the observation that the core positions of the air showers detected with the vertically oriented antenna show a significant east-west asymmetry, while those of the air showers detected with the north pointed antenna do not (see Tab. 6.4).

For molecular bremsstrahlung, a symmetric ground pattern would be expected.

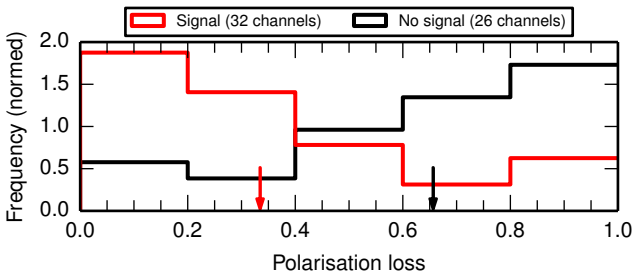


FIG. 6.13 • Fraction of power lost due to the linear polarisation of the receivers when simulating the detection of radio pulses predicted by CoREAS for the air showers detected with CROME. The histogram of the polarisation loss is shown for the receivers that measured a signal (red line) and those without a signal (black line). The mean values of the distributions are indicated by arrows.

*Polarisation*

As noted above, the observation of three air showers in only one polarisation of dual-polarised beams indicates an (at least partially) polarised source signal. The CoREAS simulation code was used to quantify the correlation of the polarisation axes of the receivers with microwave signals and the prediction for conventional radio emission. Each of the detected air showers was simulated using the geometry and energy reconstructed by KASCADE-Grande assuming iron primary particles and the simulated time traces of the electric fields were filtered to the effective detector band. In Fig. 6.12, the positions of the CROME antennas relative to the core positions of the showers are shown (squares) together with the polarisation directions of the receivers which detected a signal (black lines). The ellipses drawn by the simulated electric field vector are outlined in red. Note that the polarisation predicted by CoREAS is not purely linear and has a significant circular component for showers north or south of the antennas. In most of the events, the polarisation axes of the receivers and the simulated polarisation ellipses are well correlated.

To study the correlation further, the polarisation losses—the fraction of power lost due to the linear polarisation of the receivers, see Eq. (3–4)—were calculated for the simulated showers and all receivers, including those without signals. In Fig. 6.13, a histogram of the polarisation loss is shown for the air showers that were detected in the C band for the receivers with a signal (red line) and those without (black dashed line). Note that all selection criteria up to the signal threshold were also applied to the receivers without a signal. The average polarisation loss is 34 % for the channels with a signal and 67 % for the channels without a signal. The detected events are characterised by a much smaller polarisation loss, corresponding to a higher detection efficiency. The separation of the two distributions indicates a correlation of the polarisation of the receivers with the predictions of CoREAS. This is also confirmed by the three observations in dual-polarised beams: the polarisation loss is <10 % for the receivers with and >90 % for the receivers without a significant signal. The polarisation axes of the latter are marked by dashed lines in Fig. 6.12.

TAB. 6.6 • List of parameters for the detector simulation (see § 5.1 for details).

| Parameter | Value |
|---|---|
| System noise temperature | $T_{sys} = 90\,K$ |
| Sampling time | $\Delta t_{sim} = 0.8\,ps$ |
| Logamp slope | $V_{slope} = 24.5\,mV\,dB^{-1}$ |
| Logamp intercept | $P_0 = 21.0\,dBm$ |
| Logamp video filter | $\tau = 2.7\,ns$ |
| Post-detection filter | $H_{AC} = 0.106$, $H_{DC} = 0.0098$ |
| Oscilloscope noise | $\sigma_U = 0.4$ LSB (157.5 µV) |
| Conversion gain | $G_{LNB} = 64.5\,dB$ |

We can now calculate the probability of this observation for an unpolarised radio emission. In this case, an average polarisation loss of 50 % would be expected with a statistical deviation due to the finite sample. The expected size of the statistical fluctuation was calculated by simulating the detection of the same number of pulses with a similar pulse shape as predicted by CoREAS in the detection band, but comprised of white noise with random polarisation for each time sample. The number of independent polarisation samples is then $n_{samples} = \tau_{pulse}\nu_{det}$ for a pulse of effective length $\tau_{pulse}$, given by CoREAS, which is detected with a receiver of effective bandwidth $\nu_{det}$. For an unpolarised pulse, the polarisation loss factor for each sample is $PLF = \cos^2\alpha$, with $\alpha$ drawn from a uniform distribution $[0, 2\pi)$. For a detector bandwidth of $\nu_{det} = 660\,MHz$, the average polarisation loss for the 32 channels which detected a signal is approximately normal-distributed around 50 % with a standard deviation of 3.5 %. The average polarisation loss of 34 % found for the CoREAS simulations for the channels with microwave signals is therefore 4.5 σ off the expectation for an unpolarised source signal. Within this model, the hypothesis that the observed radio emission is unpolarised is, therefore, rejected with a significance of 4.5 σ.

Molecular bremsstrahlung is assumed to be unpolarised and is, therefore, disfavoured as the dominant emission process.

### 6.4.1 *Amplitude comparison*

In addition to the comparisons discussed in the previous sections, a comparison of the measured pulse amplitudes with the predictions of the simulations give an independent handle on discriminating the two emission models. For this, the predictions of the molecular bremsstrahlung simulation and the CoREAS simulation code are used as an input for the detector simulation presented in § 5.1. Since a full end-to-end calibration of all detectors is still in progress, a set of average parameters based on the measurements and calibration of individual components are used, see Tab. 6.6.

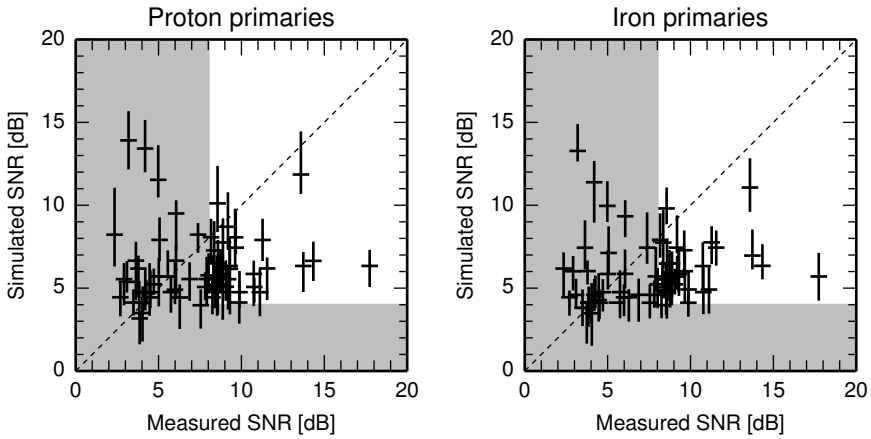


FIG. 6.14 • Correlation of the simulated signal-to-noise ratios with the measured signal-to-noise ratios for molecular bremsstrahlung simulations of proton primaries (left panel) and iron primaries (right panel). Note the logarithmic scales. For the simulated signals, the median of 25 shower simulations is shown with the corresponding 68 % region. The regions below the 8 dB threshold for the event selection and the average noise level of the simulations are marked in grey. The one-to-one correlation is indicated by a dashed line. For many channels with signals that have been detected very clearly, the simulations do not predict a signal significantly above the noise level. Furthermore, for several channels without a significant signal, large signal strengths are predicted.

*Comparison with simulations of molecular bremsstrahlung*

For each of the 31 air shower events with at least one channel with a signal, the expected power due to molecular bremsstrahlung was simulated for 25 proton-induced and 25 iron-induced showers. The shower geometries were fluctuated within the uncertainties of the KASCADE-Grande reconstruction and the parameters for the longitudinal profiles were sampled from the corresponding distributions (see § 6.3.1). The electronics response was simulated for each channel with a viewing angle of less than 4° to calculate the signal-to-noise ratios in the corresponding time windows of the same duration as for the actual signal search. The correlation of the simulated signal-to-noise ratios with the measured signal-to-noise ratios is shown in Fig. 6.14 for the two types of primary particles. The simulated signal amplitudes are poorly correlated with the measurements. For many channels with clear signals in the data, no significant signal would have been expected from molecular bremsstrahlung. Similarly, large signal amplitudes are predicted for several channels for which no significant signals have been observed. This is also shown in Fig. 6.15 in more detail for the air shower with the largest measured signal-to-noise ratio. For this event, a significant signal has been detected only in the channel with the smallest viewing angle and observing the air shower at its earliest stage of development. In the lower left panel, the median power traces expected due to molecular bremsstrahlung are shown as thick lines, with the shower-to-shower fluctuations indicated by light bands. For the channel with signal, a signal-to-noise ratio of 3 dB is predicted—less than the average fluctuations of about 5 dB due to thermal noise. However, for a second channel viewing the air shower

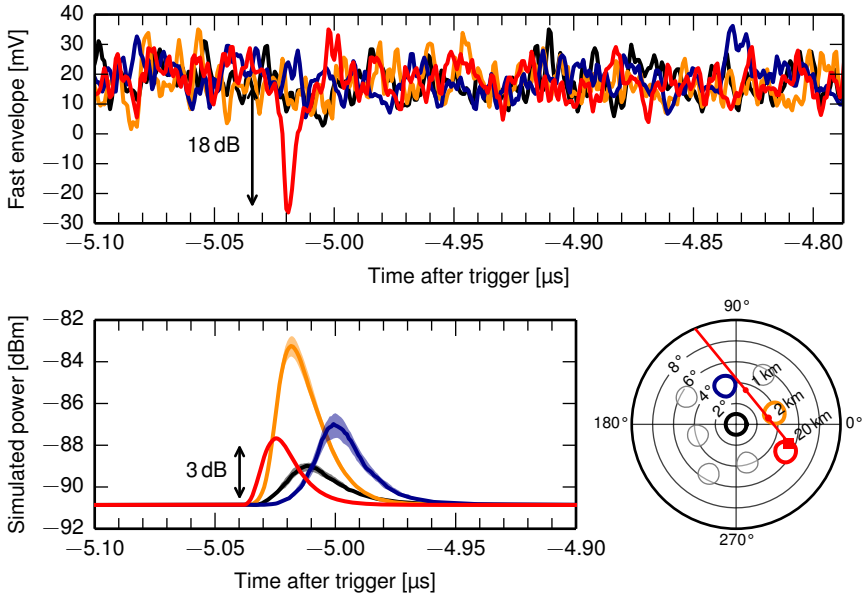


FIG. 6.15 • Comparison of measurements with the predictions for molecular bremsstrahlung for the air shower event with the largest signal measured with CROME of about 18 dB above the noise level. The geometry of the event is shown in the lower right panel, with the shower track (red line) through the fields of view of individual receivers (thick, coloured circles). The measured fast envelope traces are shown in the top panel for four channels viewing the air shower at different altitudes. A significant signal was detected only in the channel with the smallest viewing angle and observing the air shower at its earliest stage of development (red lines). In the lower left panel, the median power traces expected due to molecular bremsstrahlung are shown as thick lines, with 68 % of the shower-to-shower fluctuations indicated by light bands.

near its maximum of development, a significantly larger signal of about 8 dB is predicted, but no significant signal has been observed.

From these observations, isotropic, unpolarised radiation is disfavoured as the dominant emission process. However, a sub-leading contribution to the observed signals cannot be excluded. For deriving an upper limit on the isotropic, unpolarised microwave flux of extensive air showers, a statistical analysis of showers with large viewing angles is planned.

*Comparison with CoREAS simulations*

The values of the relevant parameters of the CoREAS simulations are listed in Tab. 6.5. For each event, one proton-induced and one iron-induced shower were simulated. For each type of primary particle, a set of 100 CONEX simulations [119] was generated and the shower with its depth of maximum, $X_{max}$, closest to the average depth of maximum was fully simulated using CORSIKA and CoREAS. The electric field vectors produced by CoREAS are preprocessed in two steps to obtain the voltage traces required for simulating the electronics response: First, the time trace of each component of the electric field is upsampled to match the sampling time of the detector simulation using the Fourier method, i. e. by extending its spectrum with the required number of zeros. Second, the detection process is simulated by calculating the voltage at the antenna terminals according to Eq. (3–1), also taking into account the polarisation loss. The antenna effective length $\mathbf{l}_{eff}$ is taken from the GRASP simulation of the radiation pattern in boresight direction. Hence, the results should be regarded as upper limits. Note that the direction dependence of the antenna gain could only be treated correctly within the CoREAS simulation, which is currently not implemented.

In Fig. 6.16, the input spectra, the voltage at the input of the logamp, and the corresponding output traces are shown for one event. For each simulated shower, 25 noise and detector simulations are run and the signal-to-noise ratios are calculated in a time window with the same length as for the event. In Fig. 6.17, the correlation of the simulated with measured signal-to-noise ratio is shown for proton primaries (left panel) and iron primaries (right panel). The one-to-one correlation is indicated by a dashed line. The signal amplitudes predicted by CoREAS are generally within the same order of magnitude as the measurements. Furthermore, a correlation, albeit with a large scatter, is observed for both types of primary particles. For about half of the events, the predicted signal amplitudes are greater than and, therefore, compatible with the measurements assuming an overestimation of the signal strength by a few dB due to neglecting the directional dependence of the antenna gain. However, the signal power for some of the events is underestimated by up to a factor of 4 (equivalent to a factor of 2 in field strength).

For further investigations, a number of shortcomings in the current analysis have to be addressed: 1) For each event and type of primary particle, only one shower with a typical depth of the shower maximum has been used. However, the detection method is sensitive to the geometrical distance to the shower maximum and, hence, showers with average $X_{max}$ might not be representative of the detected showers. To consider the shower-to-shower fluctuations,

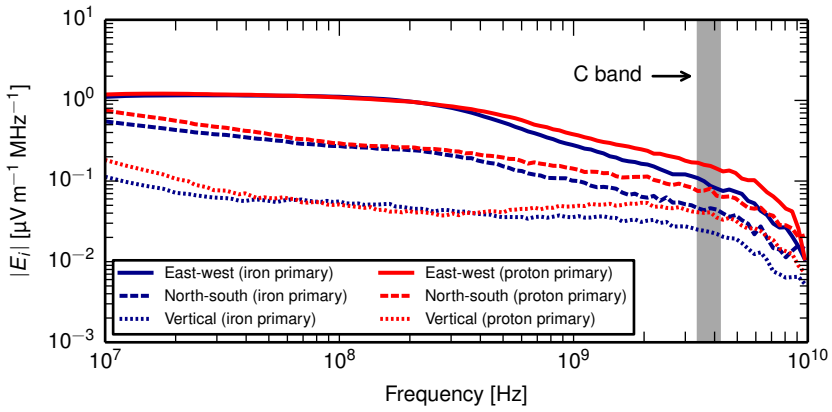


(A) Simulated field strength spectra for the three polarisation components. The C band is marked in grey. The gradual fall-off of the field strength with frequency is typical for antennas located on the Cherenkov ring.

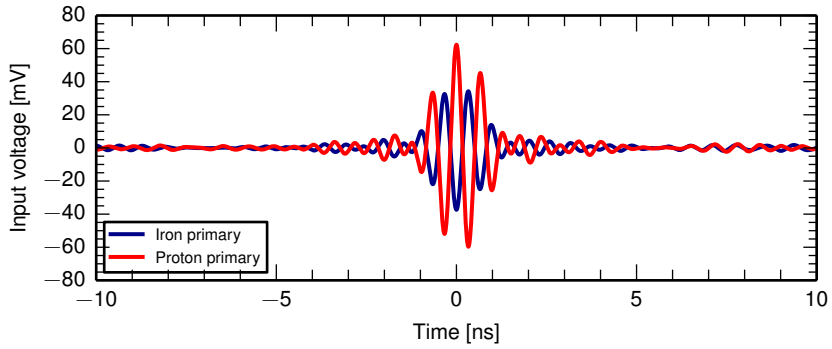


(B) Simulated voltage (re. 50 Ω) as a function of time at the input of the logamp after addition of thermal noise and the simulation of the antenna response and passive components of the electronics chain. The thermal noise power is about two orders of magnitude lower than the signal and, hence, barely visible on the linear scale (cf. panel (C)).

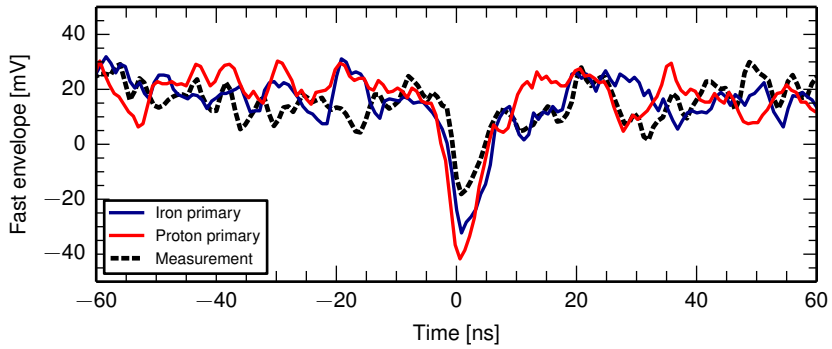


(C) Measured (black dashed line) and simulated fast envelope voltage. The shape and duration of the simulated pulses are compatible with the measurement. The amplitudes of the simulated pulses are 5 dB (iron primary) and 8 dB (proton primary) greater than the measurement, which is expected since the antenna gain is overestimated in the simulation (see text for details).

FIG. 6.16 • CoREAS simulations of one iron primary (blue lines) and one proton primary (red lines) with average depths of the shower maximum (see text) for one event. The input spectra to the detector simulation (top panel) are shown along with the simulated intermediate voltage at the input of the logamp (middle panel) and the sampled voltage trace (lower panel).

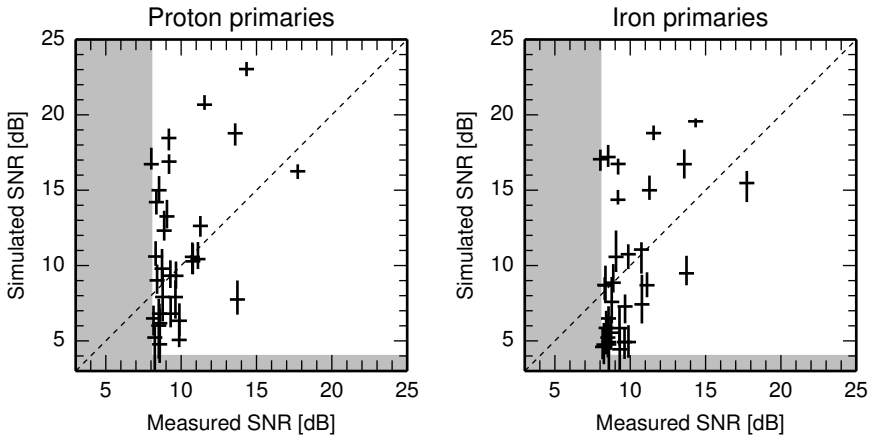


FIG. 6.17 • Correlation of the simulated signal-to-noise ratios with the measured signal-to-noise ratios for CoREAS simulations of proton primaries (left panel) and iron primaries (right panel). Note the logarithmic scales. For the simulated signals, the median of 25 noise and detector simulations is shown with the corresponding 68 % region. The regions below the 8 dB threshold for the event selection and the average noise level of the simulations are marked in grey. The signal amplitudes predicted by CoREAS are of the same order of magnitude as the measurements. Due to the overestimation of the antenna gain in the simulation, the simulated signal-to-noise ratios are expected to be located above the one-to-one correlation (dashed line). This is observed for about half of the events, which mostly crossed the field of view at large observation angles.

more air showers need to be simulated and, additionally, the uncertainties of the KASCADE-Grande reconstruction have to be considered. 2) The observed discrepancies between measurement and simulation might be related to shortcomings of the simulation of radio emission at GHz frequencies and, correspondingly, small distance scales in showers. In particular, the influence of the time resolution, thinning factor, and track length need to be investigated. Furthermore, the measurements should be compared to the predictions of other well-tested simulation codes for radio emission of air showers, e. g. ZHAireS [120]. 3) The direction dependence of the radiation patterns of the detectors are currently not considered within the simulation codes. Until this issue is resolved, the estimates could be improved by, for example, calculating the average gain for the emitting regions given by the time delay model presented in Ref. [117]. 4) In the current analysis, average values have been chosen for the parameters of the detector simulation. The values have to be verified for all components and systematic uncertainties have to be propagated to the results.

# 7 CONCLUSIONS AND OUTLOOK

The aim of this thesis was to search for microwave radio signals of extensive air showers and investigate the application of this measurement technique to the study of ultra-high energy cosmic rays. In the limited time frame of KASCADE-Grande, three multibeam reflector antennas were constructed and operated in the extended C band (3.4 GHz to 4.2 GHz). Using high-gain antennas in the forward region of air showers in coincidence with a ground array provides a complementary approach to other experiments studying the microwave emission of air showers. It was shown that, based on readily available off-the-shelf microwave components, a microwave antenna array with the sensitivity required for the detection of signals from air showers can be built.

To understand the detector response and the expected signals, the following methods were applied:

- A full detector simulation reproducing all characteristics relevant for the detection of short transients as expected for air showers was developed on the basis of numerous measurements.
- A new technique for studying the radiation patterns of antennas was developed and successfully applied in the form of an autonomous airborne radio emitter.[1]
- The timing of the detector relative to KASCADE-Grande was carefully analysed to determine tight time windows in which signals from air showers are expected.

The results of the data analysis of 10 000 hours of common operation with KASCADE-Grande are:

- The microwave signals of 31 air showers were detected, with 33 microwave receivers showing signals compared to an expected background rate of less than two (four) at 68 % CL (95 % CL).
- The radiation was found to be forward beamed. It originates at altitudes near the expected shower maximum and exhibits a ring-like structure similar to Cherenkov light emission.
- A comparison with CoREAS simulations shows that the observations are consistent with the geomagnetic and charge excess effects being the dominant emission mechanisms when taking into account the compression of the signal duration near the Cherenkov angle.

1 It is worthwhile to note that, meanwhile, this method has been adopted by several other radio experiments, notably the radio extension of the Pierre Auger Observatory AERA, the low-frequency radio astronomy telescope LOFAR, and the Murchison Widefield Array (MWA).

- The polarisation axes of the detecting receivers are strongly correlated with the polarisation predicted by CoREAS. The hypothesis of unpolarised radiation is rejected with a significance of 4.5 σ.
- In a first comparison of the pulse amplitudes with simulations, the measurements are inconsistent with an isotropic, unpolarised radiation like molecular bremsstrahlung, independent of scaling factors. On the other hand, a correlation with CoREAS simulations is observed.

Overall, it can be concluded that, in the forward region, extensive air showers emit microwave radiation with an intensity detectable with common microwave technology. The dominant production process is most likely geomagnetic and charge excess radiation of the high-energy shower particles (in contrast to the low-energy electrons in the ionised air). Due to the forward pointed emission pattern, the observation of this radiation is only applicable in the lower energy range of $\sim 10^{16}$ eV to $10^{18}$ eV, similar to Cherenkov light. Given an appropriate detector, the strong geometric dependence of the GHz signal on the distance to shower maximum could be used to infer the type and mass of the primary particle. On the other hand, this process is most likely not suited for studying cosmic rays at ultra-high energies.

Nevertheless, a sub-leading contribution of an isotropic emission mechanism cannot be excluded, and deriving a limit on the isotropic flux with the data collected with the CROME detectors is the natural next step. At the same time, the microwave radiation of compact electromagnetic showers is being investigated in a new generation of beam test experiments [55, 56]. Preliminary results indicate that the isotropic flux is significantly lower than the original estimates [56]. However, the scaling to extensive air showers is still somewhat uncertain. Therefore, an experiment at the electron light source (ELS)—a linear accelerator located at the site of Telescope Array injecting an electron beam into the atmosphere [57]—studies the transverse emission of a fully developed electromagnetic air shower [58]. In first measurements, no evidence for a signal has been found.

*It is an old maxim of mine that when you have excluded the impossible, whatever remains, however improbable, must be the truth.*

— Sherlock Holmes in "The Adventure of the Beryl Coronet."

## ACKNOWLEDGMENTS

I would like to express my gratitude to everyone who made this thesis possible with their assistance and their support. First, I would like to thank Prof. Johannes Blümer for giving me the opportunity to work on this subject and acting as referee, and Prof. Günter Quast for acting as co-referee.

I am deeply indebted to Ralph Engel, my advisor, for his support and guidance, for sharing his broad and deep knowledge of physics, and for always knowing what to do next. This work would also not have been possible without the dedication of Radomír Šmída. The close collaboration with both of you throughout the project was inspiring. During the last years, when we were uncovering hints on the emission mechanism, piece by piece, it felt a bit like an adventure of Sherlock Holmes. (Still, I would never state anything as bold as Mr. Holmes above.)

Many people have contributed to the success of this work. I am grateful to: Michael Riegel, for all the mechanical works, for providing assistance during the many measurements and maintenance jobs, and for many good pieces of advice. Oliver Krömer, for making and providing outstanding support for the CROME electronics and, above all, for being patient in answering all my questions about microwave engineering and measurement techniques. Michael Unger and Francesco Salamida, for creating a solid and professional analysis and simulation framework for CROME (and certainly for wrestling ROOT). Martin Will, for his short but fruitful work on CROME (and his colleagueship over the past years). Patrick Neunteufel, for insights on molecular bremsstrahlung (and for being such a pleasant officemate). Tim Huege and Marianne Ludwig, for setting up the CoREAS simulations and for many discussions on their interpretation. Hermann-Josef Mathes, for sharing his experience with DAQ systems and ham radio. Kai Daumiller, for many good ideas regarding the octocopter. The KASCADE-Grande collaboration as a whole, but especially to Jürgen Wochele for his support. Dietmar Bormann, for setting up the LOPES* DAQ, and Lars Petzold for his contributions to the L band setup (sadly, these parts of CROME did not make it into my thesis). The members of the GHz groups of the Pierre Auger Collaboration, for many fruitful discussions and sharing their experience (and, sometimes, even equipment).

For proofreading this thesis, I am grateful to Ralph Engel (especially for the last-minute stream of corrections), Benjamin Fuchs (for the constant stream of corrections), Radomir Šmída, and Daniel Huber. I am also deeply grateful to Benjamin Fuchs for his constant effort on cheering me up, despite the demanding times. Furthermore, the cosmic ray group provided a friendly working environment which has been inspiring and motivating. I especially thank all the other doctoral candidates for sharing all the worries.

Last but not least, I would like to thank my family for the continuous support they have given me. Nicole, thank you for your patience, love, comfort, and support throughout the last years. Still, the best is yet to come.

# APPENDIX

# A

# SELECTED TOPICS IN MICROWAVE ENGINEERING

In this chapter, selected concepts from the field of RF and microwave engineering are discussed. If no specific references are given, the material can be found in any introductory text book, e. g. [59].

## A.1 DOWN-CONVERSION

Down-converting receivers, also known as superheterodyne receivers, convert an incoming frequency or block of frequencies (radio frequency (RF) domain) to a lower frequency (intermediate frequency (IF) domain). The main reason for their frequent application in commercial reception systems is the less complex and therefore less expensive analogue and digital signal processing, e. g. amplification, filtering, or sampling, at lower frequencies. Also, low-frequency signals are generally less attenuated in transmission lines. For example, LNBs used for the reception of satellite TV convert the radiation received in the C or K band to a fixed IF block starting at 950 MHz—hence, less expensive and longer coaxial cables can be used for home installations.

Mathematically, down-conversion of a single frequency $f_{RF}$ is achieved by multiplying with a waveform of another frequency $f_{LO}$,

$$\cos\left(2\pi f_{RF}\cdot t\right)\cdot\cos\left(2\pi f_{LO}\cdot t\right)=\frac{1}{2}\Big[\cos\left(2\pi\left(f_{RF}-f_{LO}\right)\cdot t\right)+\cos\left(2\pi\left(f_{RF}+f_{LO}\right)\cdot t\right)\Big]. \tag{A–1}$$

The multiplication results in *two* IF frequencies, the difference frequency $f_{RF} - f_{LO}$ and the additive frequency $f_{RF} + f_{LO}$, the latter generally being an undesirable product to be removed in the IF stage. Since only the *absolute value* of the difference between $f_{RF}$ and $f_{LO}$ determines the observable IF frequency, for a fixed local oscillator (LO) frequency, *two* RF frequencies will be down-

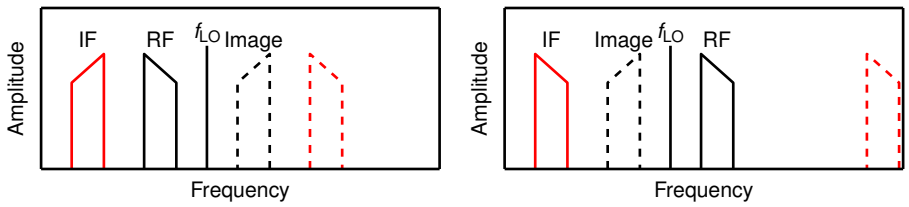


FIG. A.1 • Frequency spectra before (black) and after (red) low-side (left panel) and high-side (right panel) down-conversion. Note that for low-side conversion, the IF spectrum is mirrored with respect to the RF spectrum. After down-conversion, image frequencies (black dashed lines) also appear in the IF range and are therefore indistinguishable from the desired signals. The additive frequency components from the mixing process are shown as red dashed lines.

converted to the same IF frequency: $f_{LO} - f_{IF}$ and $f_{LO} + f_{IF}$. Since these input frequencies can not be distinguished in the IF band, the undesired input frequency—the so-called image frequency— is typically filtered using a high-order bandpass upstream of the mixer. For fixed RF and IF frequencies, two modes of down-conversion can be used: high-side conversion ($f_{LO} < f_{RF}$) and low-side conversion ($f_{LO} > f_{RF}$). For a single frequency, the two modes are equivalent. However, a band of frequencies will be mirrored when using a low-side converter, cf. Fig. A.1.

Superheterodyne receivers are realised with a non-linear device, typically a transistor or diode [59], mixing the input signal with the output of an oscillator, e. g. a dielectric resonator. Along with the additive frequencies, realistic mixers will also inject harmonics of the input frequencies and other intermodulation products, making proper filtering of the input and output necessary.

## A.2 CHARACTERISTIC IMPEDANCE OF A TRANSMISSION LINE

The characteristic impedance Z of a transmission line is the ratio of the voltage amplitude and current amplitude of a wave travelling on the line. For a transmission line terminated with a load impedance $Z_L \neq Z$, a reflected wave with relative voltage amplitude

$$\frac{V_0^r}{V_0^i} = \Gamma = \frac{Z_L - Z}{Z_L + Z}, \tag{A–2}$$

is excited, with $V_0^i$ ($V_0^r$) being the amplitude of the incident (reflected) voltage wave and $\Gamma$ the voltage reflection coefficient. Only part of the power of the incident wave $P_i = |V_0^i|^2/2Z$ will be delivered to the load,

$$P_L = P_i(1 - |\Gamma|^2). \tag{A–3}$$

It is often convenient to give the fraction of power lost due to the reflected wave in dB, the return loss

$$RL = -20\log_{10}(|\Gamma|)\,\mathrm{dB}. \tag{A–4}$$

For a load matched to the transmission line, $Z_L = Z$, no reflection of the incident wave occurs ($\Gamma = 0$), and the maximum power is delivered to the load ($RL = \infty$ dB).

Note that the equations above are only valid if the generator is matched to the transmission line. If both the generator *and* the load are not perfectly matched to the transmission line, conjugate matching of the generator impedance to the input impedance of the line, $Z_g = Z_{in}^*$, is required for maximum power transfer. See Ref. [59] for a discussion.

# B

# AIRBORNE RF EMITTER

For the analysis of the measurements with the C band reflectors, a proper description of the secondary radiation patterns—which is intrinsically tied to the pointing directions—of the reflectors is essential. Therefore, the simulations presented in § 5.1.6 and the pointing directions of the individual beams have been verified by direct measurements of the radiation patterns. A number of techniques are available for studying the far-field radiation patterns of antennas, including direct measurements in anechoic chambers, outdoor ranges, or compact antenna test ranges, and near-field scanning techniques [60]. However, all of these measurement techniques have the drawback, aside from typically being prohibitively expensive for an R&D project, that a reflector has to be dismantled to transport it to the measurement range. Since the geometries of the antennas were of particular interest for the event selection and analysis, we opted for an alternative, non-intrusive method of studying the radiation patterns. For this, a small and lightweight C band emitter was developed and attached to a flying platform to scan the fields of view of the individual receivers at distances of several hundred metres. In this chapter, the flying platform is briefly introduced. The design and calibration of the C band emitter are discussed, and the analyses of the measured data are presented.

## B.1 FLYING PLATFORM

An electronically controlled multirotor—specifically, an octocopter—was selected as flying platform. These platforms have become increasingly popular and sophisticated in the past few years, mainly due to advances in sensor and battery technology. The principle of operation is explained in Fig. B.1 for the most basic configuration of a quadrotor. The design of a multicopter can be tailored to specific needs for geometry, payload, redundancy, flight time and cost. A variety of platforms are currently available which differ mainly in the available support and the availability of pre-built hardware, open source schematics, and software. In previous work [121], an *Oktokopter* construction kit based on the Mikrokopter platform [122] was found to provide a stable flying platform which

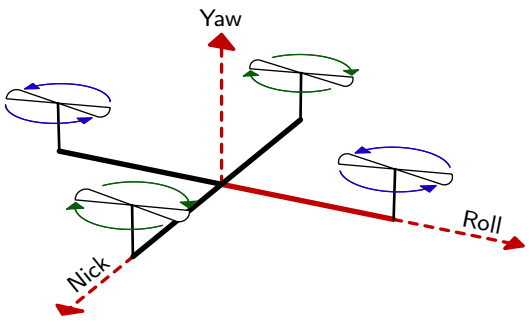


FIG. B.1 · The four engines of a quadrotor are arranged coplanarly. By using both clockwise and counter-clockwise rotating motors, the net angular momentum can be balanced. By changing the relative rotation speeds of the engines, the quadrotor can be tilted around the nick, roll, or yaw axes, using part of the thrust for lateral movements.

FIG. B.2 • Octocopter with the C band emitter (black case with white, downward-pointing spiral antenna) attached to the front arm (coloured red for identification during flight). The eight rotors are arranged coplanarly on a circle with a diameter of about 80 cm. The sensors and electronics are protected by a cover made of polyester. A lithium-ion polymer battery with an energy content of 150 W h (white) is attached to the baseplate between the landing gear.

is also well-supported by the developers and a broad user community. A photograph of a fully equipped octocopter with attached C band emitter is shown in Fig. B.2. Its eight rotors are arranged coplanarly on a circle and, therefore, provide redundant operation (the failure of any two motors can be counterbalanced). The platform is self-stabilising based on the continuous measurement of the attitude and angular velocities with a three-axis accelerometer and three gyroscopes. An additional GPS receiver and three-axis magnetic field sensor are used for autonomous positioning. For this purpose, a list of lateral waypoints is typically supplied with a laptop computer via a radio telemetry link along with optional target altitudes, waiting periods, and pointing directions for each target position. With an octocopter without significant payload, flight times of up to 30 minutes can be achieved using high-capacity lithium-ion polymer batteries. Payloads up to ~ 3 kg can be lifted, but the flight time and manoeuvrability of the platform are significantly affected for payloads heavier than about 1 kg.

A radio telemetry link operating in the Short Range Devices (SRD) band from 868 MHz to 870 MHz is used for bi-directional communication with the octocopter. The vendor supplies a graphical PC software for the parametrisation, monitoring, and programming of Mikrokopter-based multicopters. Before a flight, the octocopter is programmed with a list of target coordinates calculated from the positions of the CROME antennas and the supposed pointing directions of the receivers. During flight, diagnostic and navigational data including the position, attitude, and orientation of the platform are transmitted by the platform at a rate of 5 Hz and logged to disk along with NTP-derived timestamps.

*Positioning performance and differential GPS*

For a well calibrated octocopter flying in calm conditions, the target position is kept within few tens of centimetres. For wind speeds up to ~ 10 m s$^{-1}$ the positioning error is typically less than 1 m. An error of this size is generally tolerable, since it can be traced with the GPS positions from the navigational data and accounted for in the data analysis. On days of higher gust speeds however, flights had to be aborted at times because the octocopter could not be placed reliably in the field of view of the target receiver.

Even despite the good positioning of the octocopter, it can still be located several metres away from the real target position due to the uncertainty of the GPS-derived position. The horizontal uncertainty of the GPS is of the order of 4 m, the vertical uncertainty is typically 50 % larger [123]. The largest contribution is due to signal propagation delays introduced by the passage of the signals through the inhomogeneous and time-varying ionosphere. The uncertainty can be reduced significantly by employing a differential GPS setup, i. e. using the measurements of a static antenna—preferably, but not necessarily at a known position—to correct the measurements from a nearby roving antenna. However, the GPS module used in the octocopter setup is not capable of differential operation except for Satellite Based Augmentation System (SBAS).[a] Therefore, a handheld differential GPS receiver of the Magellan ProMark 3 series was additionally mounted on the octocopter for the flights targeting the measurement of the geometries of the CROME antennas. A small and light external antenna for the L1 frequency band, an AeroAntenna AT575-142, was installed on the bifurcation of the rear arm. The complete differential GPS, including antenna, antenna cable, and battery, weighs about 800 g and thus increases the total weight of the flying platform to more than 3 kg. The flight time is reduced to less than 15 minutes. With this setup however, measurements with higher position accuracy could be achieved and the performance of the octocopter GPS could be cross checked.

[a] *The European SBAS, EGNOS, typically improves the lateral uncertainty to below one metre.*

*Coordinate transformation*

The position of the differential GPS antenna is measured in flight with a precision significantly smaller than the distance between the antenna of the microwave emitter and the differential GPS antenna (~ 20 cm vs. ~ 50 cm). Therefore, the position of the emitting antenna has to be calculated from the position of the GPS antenna and the attitude of the octocopter. The vector from the phase centre of the GPS antenna to the phase centre of the antenna of the microwave emitter has been measured in the body frame of the octocopter (the right-handed coordinate system in which $\boldsymbol{e}_x$ points in forward direction and $\boldsymbol{e}_z$ in thrust direction). The telemetry data contains three angles defining the orientation of the octocopter:

- `heading`: rotation around the $\boldsymbol{e}_z$ axis (0°: $\boldsymbol{e}_x$ points towards geomagnetic north, 90°: $\boldsymbol{e}_x$ points east)
- `roll`: rotation around the forward axis (positive for flying left)

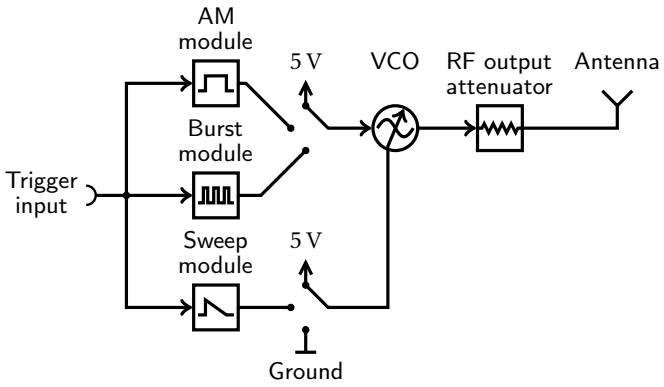


FIG. B.3 • Block diagram of the RF emitter used for calibration. The operating mode can be selected with a rotary switch: the VCO is powered either continuously, by an AM module, or a burst module, and its frequency can be set to fixed values or swept within the valid range. An attenuator of at least 6 dB is required at the output to avoid feeding back reflections from the antenna port into the VCO.

- `nick`: rotation around the axis perpendicular to the forward axis (positive for flying forward)

Note that `nick` and `roll` describe rotations around body fixed axes. The rotation matrix to transform vectors measured in the body frame to the LTP can be written as

$$R = \begin{pmatrix} \cos\Theta\cos\Psi & \sin\Phi\sin\Theta\cos\Psi - \cos\Phi\sin\Psi & \cos\Phi\sin\Theta\cos\Psi + \sin\Phi\sin\Psi \\ \cos\Theta\sin\Psi & \sin\Phi\sin\Theta\sin\Psi + \cos\Phi\cos\Psi & \cos\Phi\sin\Theta\sin\Psi - \sin\Phi\cos\Psi \\ -\sin\Theta & \sin\Phi\cos\Theta & \cos\Phi\cos\Theta \end{pmatrix}, \tag{B–1}$$

with the three Euler angles commonly used in aeronautics [124]:

- yaw angle $\Psi = \frac{\pi}{2} - (\texttt{heading} + \varphi_B)$,
- pitch angle $\Theta = \texttt{nick}$, and
- roll angle $\Phi = -\texttt{roll}$.

The geomagnetic declination at the CROME site is $\varphi_B \approx 1.4°$ (i. e., magnetic north points slightly towards geographic east).

## B.2 C BAND EMITTER

The microwave emitter is built around a Mini-Circuits ZX95-3760+ voltage controlled oscillator (VCO). The frequency of the VCO can be tuned in the nominal range of 2970 MHz to 3950 MHz by applying a voltage $V_{tune}$ of 0 V to 15 V to a control port. The output power is specified as 8.5 dBm at the lowest frequency and 6.9 dBm at the highest frequency for a 50 Ω system. The VCO is small and lightweight and therefore perfectly suited to be used on a flying platform.

To simplify the use of the VCO as a calibration source, an analogue circuit and casing were designed by O. Krömer (IPE/KIT). A block diagram of the emitter is shown in Fig. B.3. The circuit is powered by a single 9 V battery through a linear voltage regulator. The following operating modes can be selected with a rotary switch:

- *Continuous wave (CW) modes.* A continuous signal of fixed frequency is emitted. The frequency can be selected as either 2987 MHz or 3341 MHz.
- *Triggered pulse modes.* On detection of a trigger signal, an RF pulse with a duration of 180 ms is emitted. The frequency can either be fixed to 3341 MHz or swept over the full range of the VCO.
- *Triggered burst mode.* On detection of a trigger signal, an RF pulse with a duration of 180 ms is emitted. The amplitude is modulated by a 10 kHz square wave. The frequency can either be fixed to 3341 MHz or swept over the full range of the VCO.

The pulse and burst modes can be triggered either by an internal 3 Hz clock or by an external source. When attached to the octocopter, the pulse-per-second (PPS) signal of its GPS module is used to trigger the emitter, allowing convenient synchronisation with the CROME DAQ.

### B.2.1 *Calibration of the RF Emitter*

Since the RF emitter is used as a calibration source, the frequency and temperature dependences of the output power were measured in laboratory setups. Special care was taken to understand and parametrise the temperature dependence of the frequency sweeps, as this operating mode has been used during most of the calibration flights. The calibration of the emitting antenna is discussed in the next section.

Depending on the altitude and the part of the dynamic range of the detector to probe during a measurement flight, the RF emitter is equipped with coaxial SMA attenuators of the Radiall R4118 series. Three configurations with nominal attenuations of 6 dB, 12 dB, and 18 dB have been used. The power available after the attenuation, at the antenna terminal of the RF emitter, was measured using an Agilent N9912A RF analyser. The antenna terminal was connected to the spectrum analyser using an SMA(f)–N(m) adaptor. During test measurements, no significant difference between powering the emitter using a battery or an external power supply could be observed. Also, changing the input voltage in the range of 7 V to 10 V—typical for a discharging nine-volt battery—had no effect on the output power or frequency of the emitter. A regulated power supply set to 9 V was used for all following measurements.

#### *Calibration of the triggered frequency sweep mode*

Lacking a synchronisation between the frequency sweeps of the spectrum analyser and the RF emitter, the "maximum hold" measurement mode, displaying the maximum measured power for each frequency bin, was used to measure the

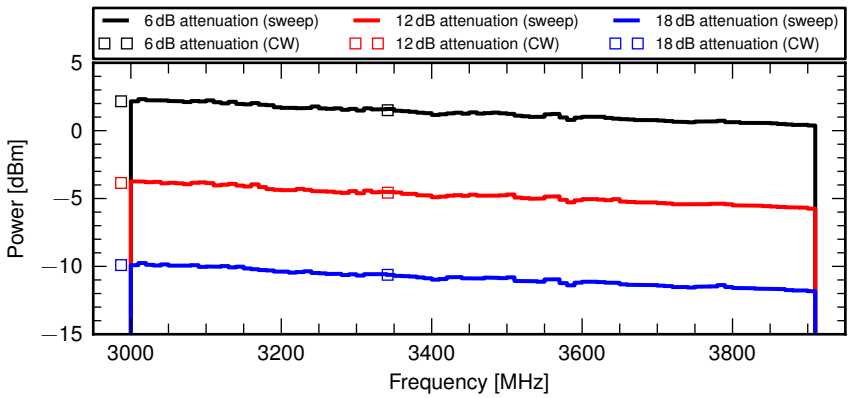


FIG. B.4 • Output power at the antenna terminal of the RF emitter as a function of frequency for different configurations in the frequency sweep mode (lines) and the two CW modes (squares).

frequency dependence of the output power. To avoid partially filled frequency bins, the resolution bandwidth of the spectrum analyser was set to a relatively large value of 1 MHz, resulting in sweep times per frequency bin faster than the sweep speed of the emitter times the bin width. The dynamic range of the spectrum analyser was chosen such that all configurations of the RF emitter could be measured without changing the input attenuation or mixer level. The settings of the spectrum analyser are summarised in Tab. B.1.

The spectral output power was measured several times for each configuration of the RF emitter. Each dataset was divided in frequency in 10 MHz bins and the maximum measured power for each bin, the power envelope, was determined. Averaging the envelopes of the measurements of each configuration of the RF emitter, mean values and the associated statistical uncertainties were calculated.

The obtained spectra are shown in Fig. B.4. The observable decrease in power is well described by a line in logarithmic space within the frequency range of 3010 MHz to 3900 MHz,

$$P_{\mathrm{out}}(f_t) = \begin{cases} p_0(T) + s \cdot (f_t - 3\,\mathrm{GHz}) & \text{for } 3010\,\mathrm{MHz} < f_t < 3900\,\mathrm{MHz}, \\ 0\,\mathrm{W} & \text{otherwise.} \end{cases} \tag{B–2}$$

The parameters obtained by fitting the spectrum of each emitter configuration are shown in Tab. B.2. The residuals have a standard deviation of 0.1 dB and contain a common structure arising from the frequency dependence of the VCO output power and the ripple of the frequency response of the spectrum analyser. The ripple induced by the spectrum analyser seems to be the dominant contribution, as spectra obtained with a Tektronix RSA 3408A benchtop spectrum analyser show residuals with similar size but different structure.

Since no direct information on the received frequency can be obtained from the measurements with the C band antennas, the time structure of the frequency sweep of the emitter has to be known. In the datasheet of the VCO, the output frequency is tabulated as a function of the tuning voltage for three

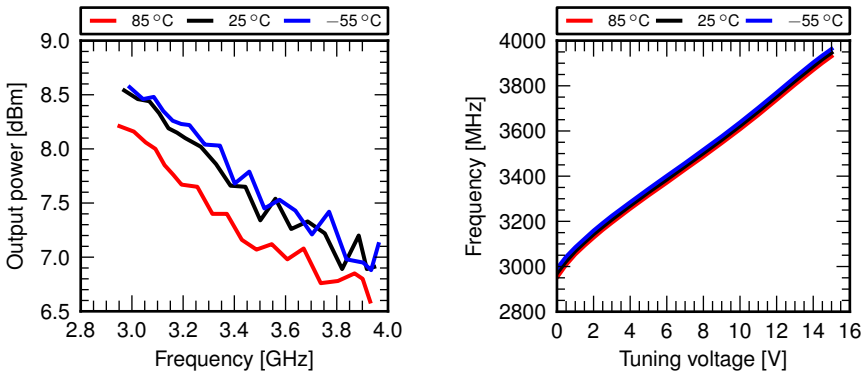


(A) Output power of the VCO as a function of frequency for three temperatures.

(B) Frequency of the VCO as a function of tuning voltage for three temperatures.

FIG. B.5 • Characteristics of the VCO used in the RF emitter as given in the datasheet.

temperatures, see Fig. B.5b for a graphical representation. The dependence was measured using a PicoScope 6402 oscilloscope to digitise the tuning voltage and a spectrum analyser to measure the output frequency. The measurements, performed at an ambient temperature of 22 °C, are well described by the values given in the datasheet for a temperature of 25 °C with an additional offset of −208 mV. The temperature dependence of both the output power and the output frequency are discussed below.

*Calibration of the CW modes*

The output power in both CW modes was measured using the same amplitude and bandwidth settings as presented in Tab. B.1. The results are tabulated in Tab. B.3 and shown as symbols in Fig. B.4. The measured output powers at 3341 MHz in frequency sweep mode and CW mode are compatible. No significant bias due to the binning and peak detection for the frequency sweep measurements could be observed.

*Temperature dependences*

The capacity determining the length of the tuning voltage sweep is temperature dependent. The effects of changing temperature were measured in a temperature chamber from 30 °C down to −5 °C in steps of 5 K. The voltages at the tuning port $V_{tune}$ and the power input $V_{cc}$ of the VCO were measured using a PicoScope 6402, located outside of the chamber, with voltage probes. The actual temperature of the VCO was monitored using an external Newport 202A-RC module with a Pt100 probe mounted on the chassis of the VCO. The output voltage of the module is proportional to the temperature and was also digitised by the oscilloscope. Throughout the measurement, the emitter and oscilloscope were continuously triggered by an external 1 Hz clock to resemble the operating conditions during a measurement flight.

TAB. B.1 • Configuration of the Agilent N9912A RF analyser for the calibration of the RF emitter in the frequency sweep mode. Differing settings used for the calibration of the CW modes are listed in parentheses.

| Option | Value |
|---|---|
| Resolution bandwidth | 1 MHz |
| Video bandwidth | 1 MHz |
| Sweep type | Step |
| Reference level | 5 dBm |
| RF attenuator | 15 dB |
| Trace type | Maximum hold (average) |
| Detector type | Positive peak (automatic) |

TAB. B.2 • Fit parameters of the spectral output power $P_{out}$ of the RF emitter in frequency sweep mode for its different configurations. $p_0$ is the output power at 3 GHz, s the spectral slope. Statistical uncertainties are given.

| Configuration | $p_0$ [dBm] | s [dB GHz$^{-1}$] |
|---|---|---|
| −6 dB | 2.25 ± 0.02 | −2.10 ± 0.04 |
| −12 dB | −3.80 ± 0.02 | −2.13 ± 0.04 |
| −18 dB | −9.87 ± 0.02 | −2.17 ± 0.04 |

TAB. B.3 • Measured output power of the RF emitter in two CW modes at 2987 MHz and 3341 MHz for its different configurations. Statistical uncertainties are given.

| Configuration | 2987 MHz [dBm] | 3341 MHz [dBm] |
|---|---|---|
| −6 dB | 2.17 ± 0.03 | 1.51 ± 0.03 |
| −12 dB | −3.85 ± 0.04 | −4.57 ± 0.05 |
| −18 dB | −9.90 ± 0.05 | −10.62 ± 0.05 |

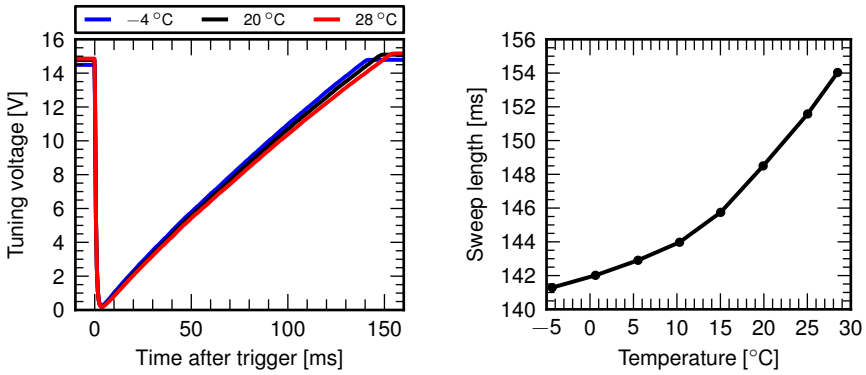


(A) Tuning voltage as a function of time during a frequency sweep of the emitter for three temperatures.

(B) Length of a frequency sweep of the emitter as a function of temperature.

FIG. B.6 • Temperature dependence of the tuning voltage during the frequency sweep of the C band emitter.

For each temperature step, the VCO reached thermal equilibrium after 20 min and the following 10 min were used for data analysis. The voltage sweeps for three temperatures are shown in Fig. B.6a. The duration of the sweep increases with temperature and changes slightly in scale. The voltage sweep measured at 20 °C was used as reference for the model

$$V_{\text{tune}}(t) = s_V \cdot V_{\text{tune}}^{20\,^\circ\text{C}}(s_t \cdot t) + V_{\text{offset}} \tag{B–3}$$

to fit the voltage scaling factors $s_V$, time compression factors $s_t$, and voltage offsets $V_{\text{offset}}$ to the sweeps obtained at different temperatures. The resulting fit parameters are tabulated in Tab. B.4. The temperature dependence of the sweep length, calculated from $s_t$, is shown in Fig. B.6b.

To study the temperature dependence of the relationship between the tuning voltage and the frequency of the emitter, the measurement setup described above was extended by a spectrum analyser measuring the output spectrum of the emitter in pulsed CW mode at 3341 MHz. The spectrum analyser was triggered with the same 1 Hz clock as the emitter and oscilloscope. The temperature was varied within −5 °C to 30 °C to determine the temperature drift of the tuning voltage, output frequency, and output power. The tuning voltage was found to be constant over the whole temperature range. However, both the output frequency and the output power decrease with temperature, an effect which is also described in the datasheet of the VCO, see Fig. B.5. The temperature dependence of the output frequency is well described by a linear temperature coefficient,

$$\frac{\mathrm{d}f}{\mathrm{d}T} = (-0.27 \pm 0.02)\,\text{MHz}\,\text{K}^{-1}. \tag{B–4}$$

Similarly, a linear temperature dependence of the output power in dBm with a slope of

$$\frac{\mathrm{d}P_{\text{out}}}{\mathrm{d}T} = (-0.020 \pm 0.006)\,\text{dB}\,\text{K}^{-1} \tag{B–5}$$

TAB. B.4 • Measured output power of the RF emitter in two CW modes at 2987 MHz and 3341 MHz for its different configurations.

| T [°C] | $s_t$ | $s_V$ | $V_{offset}$ [mV] |
|---|---|---|---|
| −4.4 | 1.051 | 0.974 | 88.1 |
| 0.6 | 1.046 | 0.980 | 56.7 |
| 5.5 | 1.039 | 0.986 | 27.4 |
| 10.3 | 1.031 | 0.991 | 10.7 |
| 15.0 | 1.019 | 0.995 | 2.1 |
| 19.9 | 1.000 | 1.000 | 0.0 |
| 25.0 | 0.980 | 1.002 | −0.3 |
| 28.5 | 0.964 | 1.004 | 1.5 |

has been observed. Note that these drifts also apply to the frequency sweep modes.

*Uncertainty estimates*

All measurements were done in an air-conditioned lab at 22 °C and a warmup period of 90 minutes was used for the measurement devices. Under these conditions, the absolute amplitude accuracy of the Agilent N9912A RF analyser is given as ±0.6 dB. The frequency accuracy is limited by the 10 MHz bins. The spectra and frequency measurements were compared to independent measurements with a Tektronix RSA 3408A spectrum analyser and found to be compatible well within the systematic uncertainties of the two devices.

During calibration flights the VCO was operated in a temperature range of about 0 °C to 30 °C. The ambient temperatures were recorded for each flight and the related corrections are applied in the analysis. The remaining uncertainties in the output power of the emitter due to the slightly higher temperature inside the casing of the emitter are estimated to be about 0.1 dB. The uncertainty in frequency is expected to be negligible compared to the width of the frequency bins used in the analysis.

### B.2.2 *Emitting Antenna*

The RF emitter was equipped with a cavity backed spiral antenna of type QSPCP2-18SLH manufactured by Q-par Angus Ltd. A spiral antenna was chosen for two reasons. First, it emits circularly polarised waves. Therefore, the polarisation loss for the linearly polarised C band receivers is a constant factor of −3 dB, independent of the rotation of the octocopter. Second, broadband spiral antennas are well matched and have a nearly constant gain over a wide bandwidth. Additionally, the cavity backing has the advantage of a large front-to-back ratio, i.e., most of the power is radiated in the forward direction. When the antenna is mounted at an appropriate position, the power reflected on parts of the octocopter is negligible. With a diameter of 8 cm and a weight of

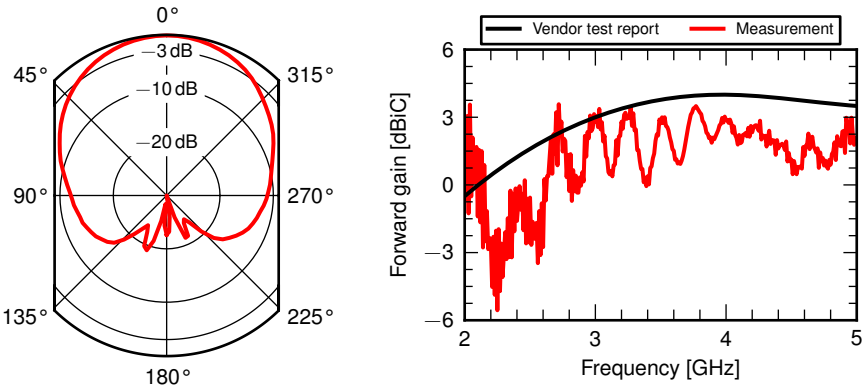


(A) Normalised radiation pattern of the calibration antenna averaged from measurements in an antenna test chamber between 3 GHz and 4 GHz.

(B) Boresight gain of the calibration antenna taken from the test report of the vendor and as measured in an antenna test chamber. The systematic ripple is believed to be an artifact of the measurement. The measured data is not used in the analysis.

FIG. B.7 • Characteristics of the wideband spiral antenna used for the calibration flights.

126 g it is compact, lightweight, and thus only has a small impact on the flight time of the octocopter. The vendor provides a test report including plots of the antenna gain and half-power beamwidth over the frequency. However, the radiation pattern in C band—required for the calculating the power radiated in the direction of the reflectors—is not given.

To cross-check and supplement the data provided by the vendor, the radiation pattern of the spiral antenna was measured in an anechoic antenna test chamber at the IHE, KIT. The antenna was mounted on a rotary platform and the power transfer to a linearly polarised horn antenna was measured with a vector network analyser for $f = 2\,\text{GHz} \ldots 5\,\text{GHz}$ ($\Delta f = 10\,\text{MHz}$) and $\theta_{em} = -180° \ldots 180°$ ($\Delta\theta = 4°$). The average relative gain in the frequency range of 3 GHz to 4 GHz is shown in Fig. B.7a. The half-power beamwidth is 75° and fits well to the width given by the vendor. The front-to-back ratio is better than 20 dB.

In Fig. B.7b, the measured gain in boresight direction is plotted over frequency along with the data provided by the vendor. Since the receiving horn antenna was linearly polarised, the measured data was scaled by a factor of two (3 dB) to account for the polarisation loss. The measurements show a ripple of unreasonable structure and amplitude compared with the vendor data. Similar artifacts were observed during calibration measurements of L band antennas with the same equipment and found to be a problem of the measurement setup [81]. The measurements of the direction dependence of the gain, however, are unaffected. Therefore, the boresight gain as specified by the vendor will be used in the following analyses along with the normalised radiation patterns from the measurements. The power radiated by the antenna is then

$$P_{rad}(f, \theta_{em}) = G_0(f)\, \hat{G}(f, \theta_{em})\, P_{out}(f), \tag{B–6}$$

with the emission angle $\theta_{em}$ with respect to the boresight axis[b], the boresight

[b] *According to the vendor test report, no significant rotational asymmetry is expected.*

TAB. B.5 • Sources of systematic uncertainties of the power radiated by the RF emitter.

| Source | Uncertainty [dB] |
|---|---|
| Boresight gain | 0.8 |
| Amplitude accuracy of spectrum analyser | 0.6 |
| Influence of mechanical structures on gain | 0.2 |
| Fit to emitter spectra | 0.1 |
| Temperature dependence | 0.1 |
| Total | 1.0 |

gain $G_0$, the normalised radiation pattern $\hat{G}$, and the power at the antenna terminal of the emitter $P_{out}$.

The boresight gain is given by the manufacturer for a 50 Ω source and is quoted with a systematic uncertainty of 0.8 dB. Because of the large front-to-back ratio of the antenna, the power emitted in the direction of the reflectors is not expected to change significantly due to the mechanical structures of the octocopter. However, since this cannot be determined with measurements in the anechoic chamber, an additional uncertainty of 0.2 dB is estimated. The return loss of the antenna is better than −10 dB. Since well-matched attenuators are installed between the VCO and the antenna, the power reflected at the antenna terminal is not expected to change the properties of the VCO significantly and is also not expected to excite standing waves of significant amplitude. Similarly, the emitter can be treated as a 50 Ω source to good approximation. In total, the systematic uncertainty on the power radiated by the flying emitter is expected to be of the order 1.0 dB (−20 % to 25 %). The individual sources are tabulated in Tab. B.5.

## B.3 MEASUREMENT SETUP AND ANALYSIS

### *Measurement setup and flight plans*

To synchronise the CROME data acquisition with the pulses from the C band emitter, the PicoScopes are triggered with the PPS signal of the Meinberg GPS clock which usually provides event timestamps. The oscilloscope inputs are configured with 1 MΩ input impedance. 200 ms long traces are captured with a sampling time of 10 µs. 20 ms of each trace are used for estimating the noise level, 10 ms before the PPS trigger and 10 ms after the end of a pulse.

The C band emitter is mounted on the bifurcation of the front arm of the octocopter. The spiral antenna is kept in a fixed location pointing along the negative yaw axis (i. e., downwards when the octocopter is leveled). The handheld differential GPS is fixed below the baseplate of the octocopter, with the antenna attached to the bifurcation of the rear arm. In survey measurements with the differential GPS, a lengthy initialisation period and stop and go measurements with at least one minute of observation at single survey points are required to obtain the highest precision. For the octocopter measurements, a more suitable

mode of measurement is used: the handheld unit is configured to measure in kinematic mode, in which satellite data is recorded with a rate of 1 Hz. Furthermore, the differential GPS receivers are initialised dynamically to avoid additional initialisation time. The successful post-processing of the data requires a common observation of at least four satellites for several tens of minutes by both units. Therefore, care has to be taken not to obstruct the GPS antennas, e. g. while replacing the battery of the octocopter. The post-processing yields the differential vectors in the Cartesian Earth-Centred Earth-Fixed (ECEF) coordinate system and error estimates for each component, typically better than ±20 cm. To convert the vectors to the LTPs of the reflectors, reference positions on the first reflector are measured before and after each flight. With these measurements, the relative centre of the reflector is calculated and the accuracy of the differential vectors is cross-checked. In normal conditions, the reflector centres are within 2 cm between measurements and the observed fluctuations are covered by the error estimates. A loss of synchronisation between the two GPS receivers results in large jumps in the positions along with unusually large error estimates of > 30 cm.

Depending on the purpose of a measurement campaign, waypoints are calculated for a set of typically three to five flights. For the purpose of studying the geometry and calibration of a receiver, the waypoints are evenly distributed on a sphere around the target antenna to cover a specific angular region of the sky at a constant distance. To obtain detailed measurements for determining the antenna geometries, flight patterns covering angular regions of 2.5° × 2.5° around the presumed boresight directions at distances between 200 m and 300 m were programmed. With typical flight times of seven to ten minutes in the field of view of a receiver, between 400 and 600 frequency sweeps are recorded for each flight.

*Data processing*

In a preprocessing step, the voltage traces obtained for each channel are merged with the attitude information of the octocopter and the differential positions of the emitting antenna. In Fig. B.8, two voltage traces obtained from different parts of the field of view of one receiver are shown. The noise level is estimated by averaging the samples up to 1 ms before the trigger and beyond 180 ms after the trigger. From each voltage trace, the part in which the frequency sweep of the emitter is expected, is obtained. The time axis is converted to frequency, see the upper scale in Fig. B.8, and binned in steps of 10 MHz in the passband (3400 MHz < f < 3940 MHz, with the upper limit given by the frequency range of the emitter). For each frequency bin, the mean voltage and the error of the mean are calculated. In the following, the signals obtained for each frequency are treated separately.

To illustrate the result of a measurement flight, maps of the signal-to-noise ratios obtained for three receivers at midband frequency are shown in Fig. B.9. The flight pattern of the octocopter is visible from the spatial distribution of the data. The mainlobes of the receivers can be identified from the locations with the largest observed signal-to-noise ratios. It is worthwhile to note that no significant increase of the noise levels or the amount of RFI pulses could be

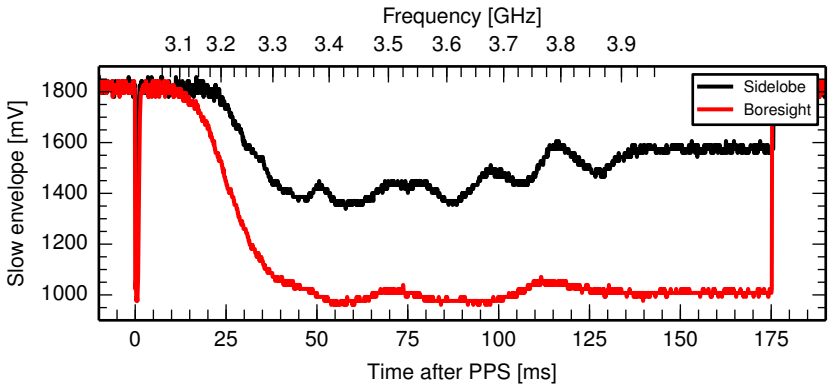


FIG. B.8 • Slow envelope voltage as a function of time for a receiver observing a frequency sweep of the flying C band emitter. The sweep starts at the pulse-per-second of the GPS clock. The initial drop of the tuning voltage at the VCO (see Fig. B.6a)—equivalent to a fast, inverse frequency sweep—is observed as a spike in the voltage trace. The frequency axis calculated from the timing is shown as upper scale. Note the non-linearity of the time-to-frequency conversion, particularly for low frequencies, and the constant frequency for the last ~ 30 ms. The signal-to-noise ratio and the ripple are strongly dependent on the position of the emitter in the field of view: in this flight, a signal-to-noise ratio of ~ 33 dB with a ripple of ~ 3 dB is observed when the emitter is located in boresight direction (black line). Since the angular separation and levels of the sidelobes are frequency-dependent, the ripple increases as the emitter moves outside of the mainlobe (red line).

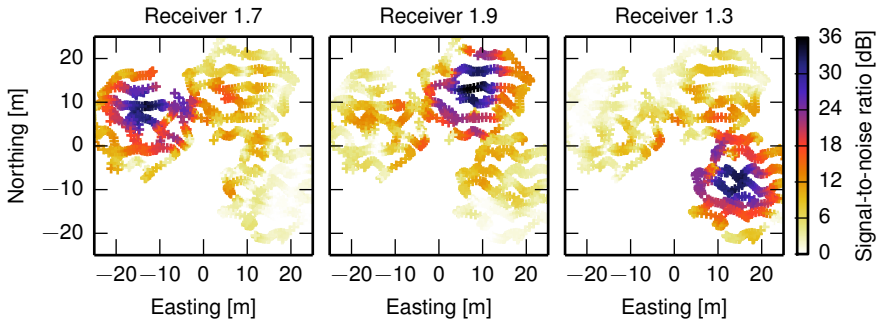


FIG. B.9 • Positions of the flying C band emitter relative to the antenna centre for three measurement flights in the fields-of-view of three receivers. For each flight, the octocopter was programmed to fly along a grid pattern covering a broad region of 7.5° × 7.5° centred at the presumed boresight axis of each receiver at a constant distance of 165 m to the antenna. The signal-to-noise ratios measured with each receiver are indicated by a common colour scale. The boresight axis of each receiver can be identified from the location with the largest measured signal-to-noise ratio.

observed with the C band receivers when operating the octocopter, including the remote control and the radio telemetry link, in the vicinity or in the field of view of the receivers.

*Fit model*

To obtain a good estimate of the direction of maximum gain and the corresponding peak voltage, the data points are fitted with a model based on the radiation patterns simulated using GRASP. Furthermore, a linear relation between the received power in dBm and the measured voltage is assumed, resulting in a total of five parameters:

- $\phi_a$, $\theta_a$: reflector azimuth and zenith angles
- $\phi_{feed}$: feed azimuth angle (only for offset feeds)
- $V_{slope}$ [V dB$^{-1}$]: slope of the calibration curve
- $V_{offset}$ [V]: offset of the calibration curve

The variables of each observation are the cartesian coordinates $\mathbf{r} = (x, y, z)$ and the orientation $\mathbf{R} = (\Psi, \Theta, \Phi)$ of the emitter antenna in the LTP of the reflector. For each observation, the power $P_r$ at the position of the receiver $(0, 0, 0)$ is calculated according to the Friis transmission equation,

$$P_r = \langle \mathrm{PLF} \rangle \cdot \hat{G}_r(\mathbf{r}, \theta_a, \phi_a, \phi_{feed}) \cdot P_{rad}(\lambda, \mathbf{r}, \mathbf{R}) \cdot \left( \frac{\lambda}{4\pi |\mathbf{r}|} \right)^2 , \tag{B–7}$$

with the following variables:

- $\langle \mathrm{PLF} \rangle$: polarisation loss factor for the wave at the receiver. Since a circularly polarised emitter and a linearly polarised receiver are used, $\langle \mathrm{PLF} \rangle = ½$.
- $\hat{G}_r$: normalised radiation pattern simulated with GRASP (§ 5.1.6). The pattern is transformed to the antenna coordinate system using the rotation matrix given in Eq. (5–28) (with $\phi_c = \phi_{feed}$). The gain is interpolated using a bivariate cubic spline to obtain residuals smoothly varying with the fit parameters.
- $P_{rad}$: power radiated by the emitter in the direction of the receiver (Eq. (B–6)). The angle to the boresight axis of the emitter antenna is calculated using the rotation matrix Eq. (B–1). As the gain of the emitting antenna is symmetric in azimuth, a one-dimensional cubic spline is sufficient for the interpolation.

The output voltage $V$ of the slow envelope is then calculated assuming an ideal transfer function for the logamp:

$$V = V_{slope} \cdot P_r\,[\mathrm{dBm}] - V_{offset}. \tag{B–8}$$

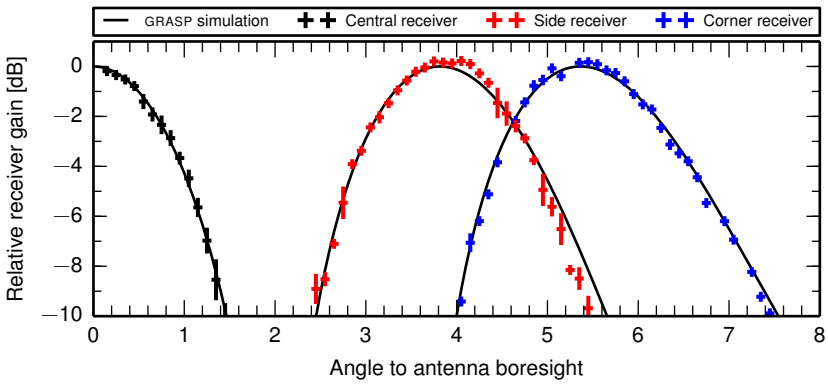


FIG. B.10 • Relative gain as a function of angle to the boresight axis of the central feed for three receivers (profiles), one for each scan distance in a nine-feed camera. The data was taken at a distance of about 265 m to the antenna. The respective far-field radiation patterns simulated with GRASP are shown as black lines. Each profile is calculated from the data points of one flight located within about 0.2° of a great circle through the field of view of the receiver. The shapes of the mainlobes are consistent with the simulated radiation patterns down to at least −10 dB.

### *Minimisation procedure*

To reduce the influence of side lobes which might not be described well by the simulated radiation patterns, only the data points within 1° of the point of maximum signal are regarded in the minimisation. When positions derived from the differential GPS are used, the points affected by a loss of synchronisation between the two differential GPS units are identified by uncertainties > 30 cm in the position and removed. Similarly, traces with an elevated or unstable noise level are discarded.

To find the optimal set of parameters, the sum of the squared residuals $\chi^2$ is minimised numerically. Errors in the position and orientation of the octocopter are considered in the minimisation by using the effective variance [125] as weights. It turns out that the $\chi^2$ function has numerous local minima owing to symmetries and periodicities of the radiation pattern. Hence, local minimisation algorithms cannot be applied realiably. The parameter space is therefore manually constrained and a global optimisation algorithm, the multi level single linkage method [126] implemented in the nlopt library [127], is used for the minimisation.

## B.4 RESULTS

### *Measured radiation patterns*

The measured shapes of the mainlobes are consistent with the GRASP simulations of the far-field radiation patterns down to at least −10 dB relative to the boresight gain. This is illustrated in Fig. B.10, in which profiles of the normalised signal-to-noise ratios from three flights are shown in comparison to the simulated radiation patterns. The angles between the boresight direction of the central receiver and the offset receivers are $(3.79 \pm 0.02)°$ for the edge posi-

tions (scan distance $\delta = 100.0\,\text{mm}$) and $(5.40 \pm 0.02)°$ for the corner positions ($\delta = 141.4\,\text{mm}$) of the nine-feed cameras.[c] These values are independent of frequency—only a random scatter within about 0.02° is observed—and consistent with the simulated offset angles of 3.82° and 5.37°, respectively. In azimuth, the mainlobes of the individual beams are found at multiples of 45° as expected from the camera mechanics.

[c] *Note that the boresight direction of the central feed is a free parameter when fitting offset feeds.*

*Determination of the antenna geometry*

The parameters required for a full description of the geometry of an antenna are the zenith angle $\theta_a$ and azimuth angle $\phi_a$ of the central beam, and the camera rotation angle $\phi_c$ (cf. § 5.2.2). The shapes of the minima of the fit statistics suggest angular uncertainties of about 0.02° for each fit. Since no systematic change with frequency is observed, the weighted mean of the boresight directions fitted for all frequencies is calculated for each measurement flight. The average boresight directions differ by up to 0.1° between individual flights which suggests a sufficient precision which is also significantly better than for the geometries calculated indirectly using differential GPS surveys of the reflectors. The observed scatter of 0.1° could be related to mechanical instabilities of the antennas and, hence, is assumed to correspond to the best precision that can be achieved without continuous monitoring of the reflector and camera orientations.

For each receiver, the average boresight direction is calculated from all measurement flights. After applying the inverse rotation $\mathsf{R}^\top$ from Eq. (5–28), the azimuth angles of the individual offset beams are calculated. The camera rotation angle is then calculated as the average of the azimuth angles modulo 45° with an uncertainty of about 0.1°. The average parameters are listed in § 5.2.2, Tab. 5.6.

# C

# EVENT TRACES AND GEOMETRIES

In this chapter, the signal traces and geometries of all events measured with CROME are shown. The event selection is discussed in § 6.1, with the corresponding cuts listed in Tab. 6.3. For each event, two panels are shown:

- *Left panel:* Uncalibrated power traces of the channels which measured a signal. The 8 dB threshold on the signal-to-noise ratio within the signal time window is indicated for each channel as a dashed line.
- *Right panel:* Geometry of the air shower and the receivers in polar representation relative to the antenna position (geographical coordinates). The fields of view of the receivers are shown as circles, with those of the signal channels marked in the same colour code as the corresponding traces. The fields of view of the channels without a signal are marked by grey circles. The shower track is indicated by a red line starting at an altitude of 20 km (square). The shower track is marked with dots at two additional altitudes, 2 km and 1 km.

Additional information on the events is given in the caption:

- *day/month/year hour:minute:* time of detection (UTC)
- E: primary energy estimated by KASCADE-Grande
- $\theta$, $\Phi$: zenith angle and azimuth angle of the arrival direction estimated by KASCADE-Grande
- R: distance between the shower core and the antenna location
- $SNR_i$: signal-to-noise ratio of channel $i$

The events are ordered by the time of detection.

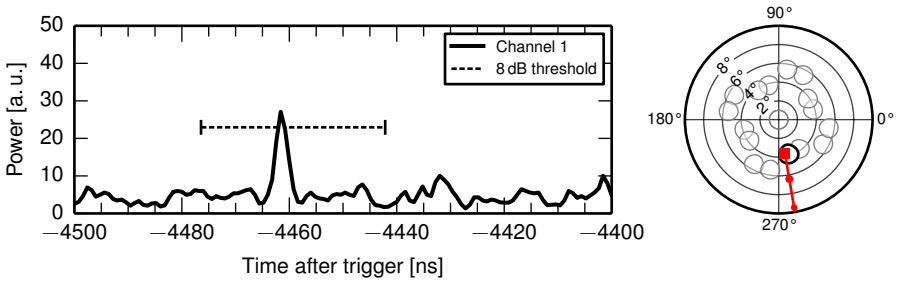


FIG. C.1 • 21/5/2011 0:41. $E = 7.2 \times 10^{16}$ eV, $\theta = 3.3°$, $\Phi = 295.5°$, $R = 109.6$ m, $SNR_1 = 8.6$ dB.

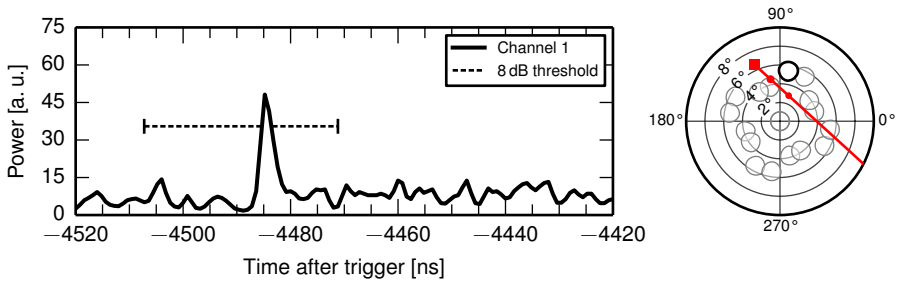


FIG. C.2 • 21/5/2011 11:18. E = 2.5 × $10^{17}$ eV, θ = 6.9°, Φ = 130.2°, R = 90.6 m, $SNR_1$ = 9.2 dB.

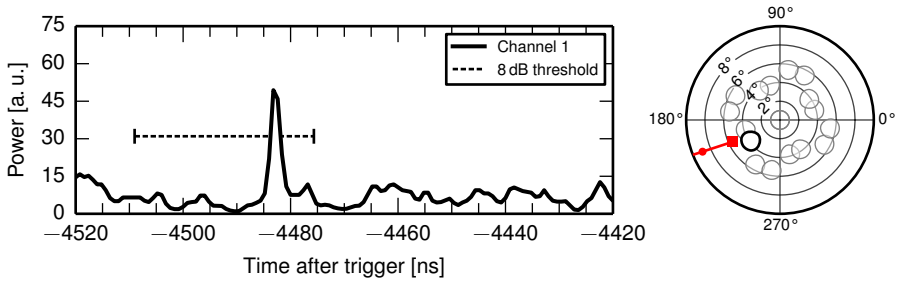


FIG. C.3 • 30/5/2011 20:39. E = 1.1 × $10^{17}$ eV, θ = 5.2°, Φ = 220.2°, R = 130.6 m, $SNR_1$ = 9.9 dB.

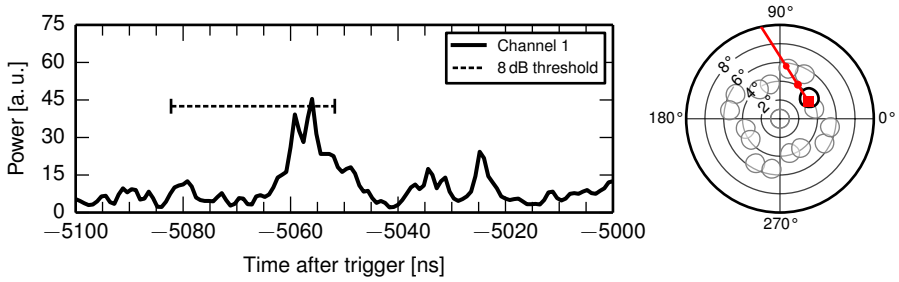


FIG. C.4 • 9/7/2011 3:16. E = 1 × $10^{17}$ eV, θ = 3.6°, Φ = 42.7°, R = 81.2 m, $SNR_1$ = 8.2 dB.

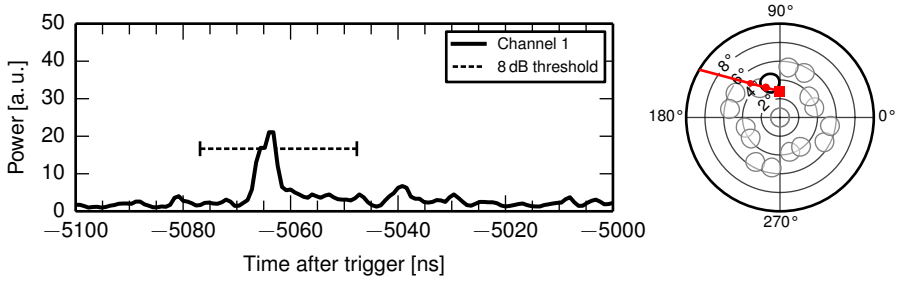


FIG. C.5 • 28/7/2011 14:21. E = 4.7 × $10^{16}$ eV, θ = 2.7°, Φ = 101.8°, R = 59.9 m, $SNR_1$ = 8.9 dB.

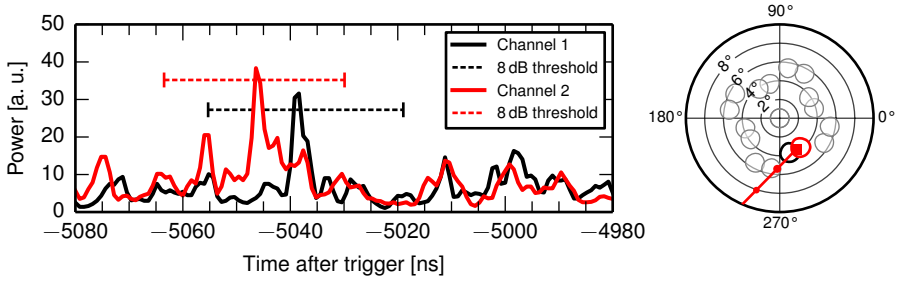


FIG. C.6 • 14/10/2011 15:25. E = 3.7 × $10^{16}$ eV, θ = 3.7°, Φ = 317.3°, R = 111.7 m, $SNR_1$ = 8.5 dB, $SNR_2$ = 8.3 dB.

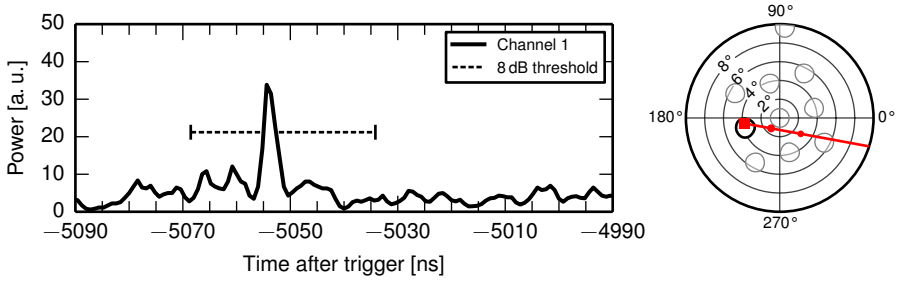


FIG. C.7 • 13/11/2011 7:42. E = 3.4 × $10^{16}$ eV, θ = 4.1°, Φ = 202.3°, R = 112.0 m, $SNR_1$ = 9.9 dB.

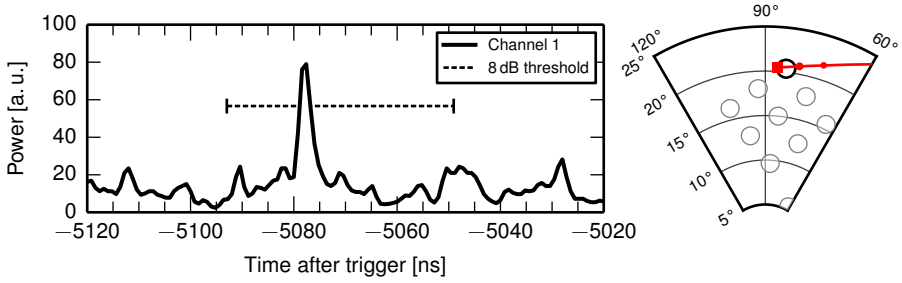


FIG. C.8 • 20/11/2011 15:05. E = 4.8 × $10^{16}$ eV, θ = 20.4°, Φ = 101.9°, R = 93.9 m, $SNR_1$ = 9.3 dB.

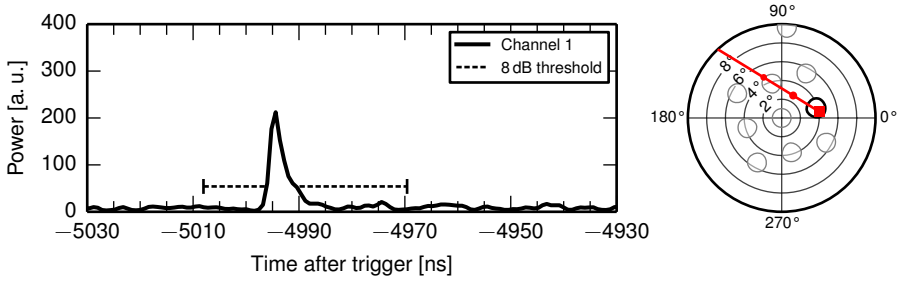


FIG. C.9 • 20/11/2011 22:07. E = 9.4 × $10^{16}$ eV, θ = 4.4°, Φ = 20.9°, R = 128.7 m, $SNR_1$ = 13.7 dB.

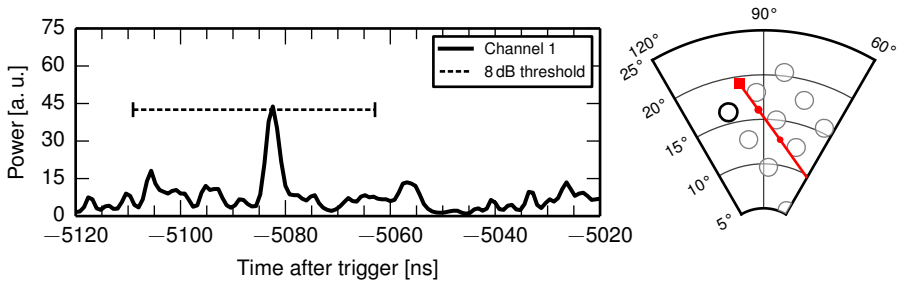


FIG. C.10 • 27/11/2011 17:43. $E = 2.4 \times 10^{17}$ eV, $\theta = 19.5°$, $\Phi = 113.7°$, $R = 143.8$ m, $SNR_1 = 8.0$ dB.

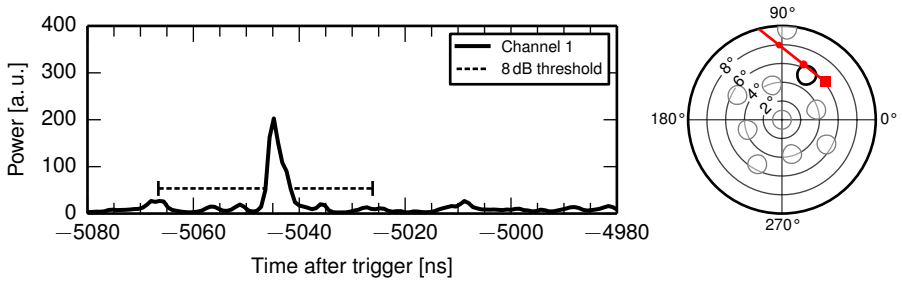


FIG. C.11 • 10/12/2011 13:06. $E = 2.3 \times 10^{17}$ eV, $\theta = 6.2°$, $\Phi = 53.0°$, $R = 115.6$ m, $SNR_1 = 13.6$ dB.

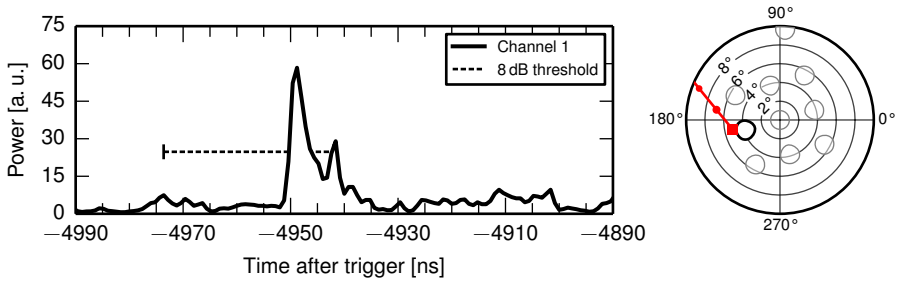


FIG. C.12 • 18/12/2011 10:57. $E = 5 \times 10^{17}$ eV, $\theta = 5.0°$, $\Phi = 208.7°$, $R = 103.3$ m, $SNR_1 = 11.6$ dB.

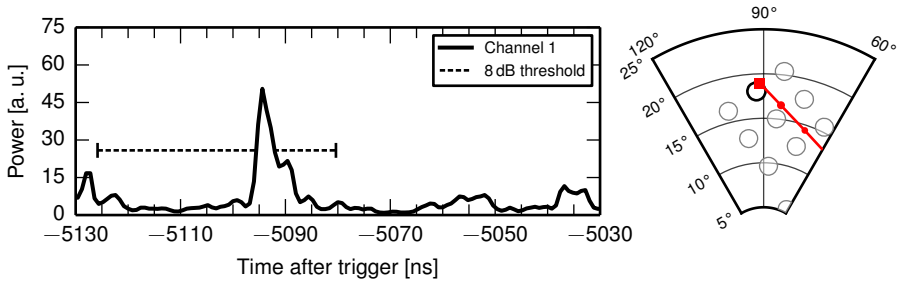


FIG. C.13 • 30/12/2011 8:57. $E = 1.6 \times 10^{17}$ eV, $\theta = 19.2°$, $\Phi = 107.0°$, $R = 133.9$ m, $SNR_1 = 10.7$ dB.

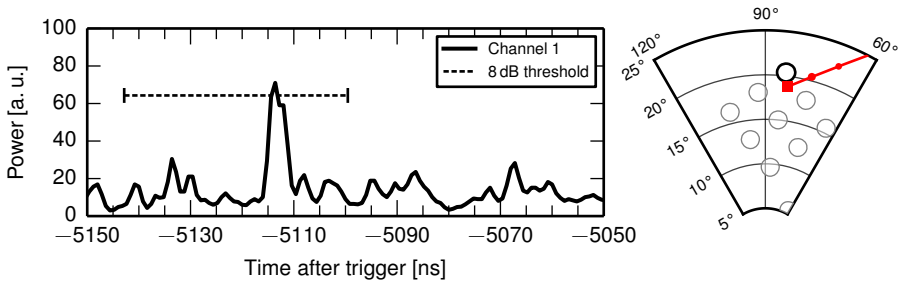


FIG. C.14 • 4/1/2012 1:12. E = 1.4 × $10^{17}$ eV, θ = 18.6°, Φ = 98.4°, R = 116.8 m, $SNR_1$ = 8.3 dB.

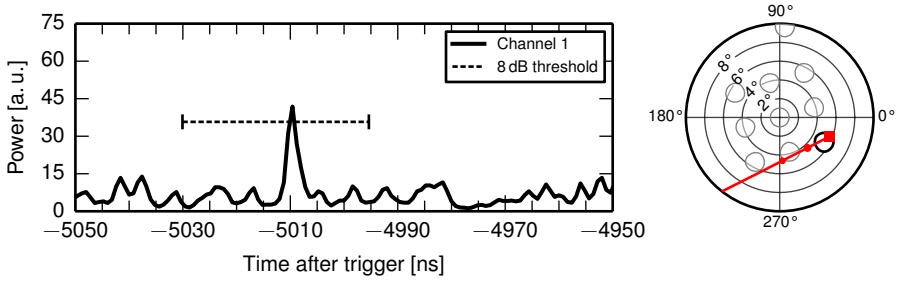


FIG. C.15 • 22/1/2012 16:39. E = 1.9 × $10^{17}$ eV, θ = 5.9°, Φ = 356.5°, R = 103.9 m, $SNR_1$ = 8.6 dB.

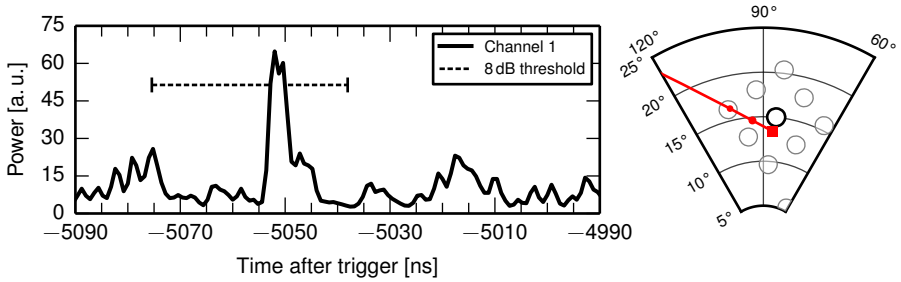


FIG. C.16 • 22/2/2012 23:09. E = 7.1 × $10^{16}$ eV, θ = 13.3°, Φ = 99.4°, R = 100.4 m, $SNR_1$ = 8.9 dB.

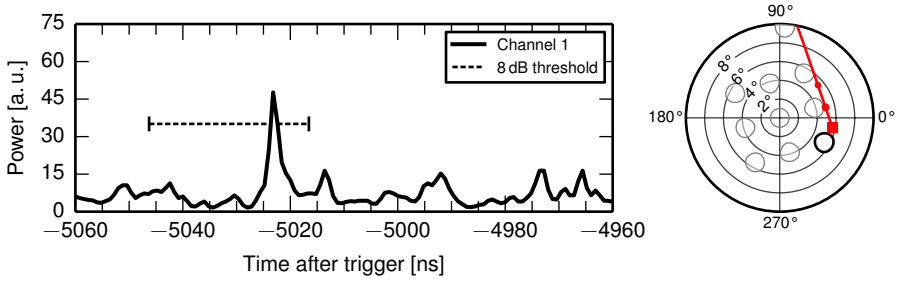


FIG. C.17 • 25/2/2012 11:15. E = 3.6 × $10^{17}$ eV, θ = 5.8°, Φ = 2.6°, R = 87.2 m, $SNR_1$ = 9.2 dB.

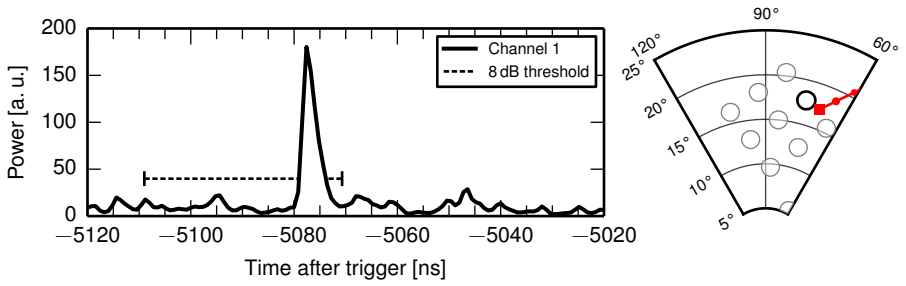


FIG. C.18 • 2/3/2012 4:37. $E = 3.4 \times 10^{17}$ eV, $\theta = 17.0°$, $\Phi = 85.0°$, $R = 82.5$ m, $SNR_1 = 14.3$ dB.

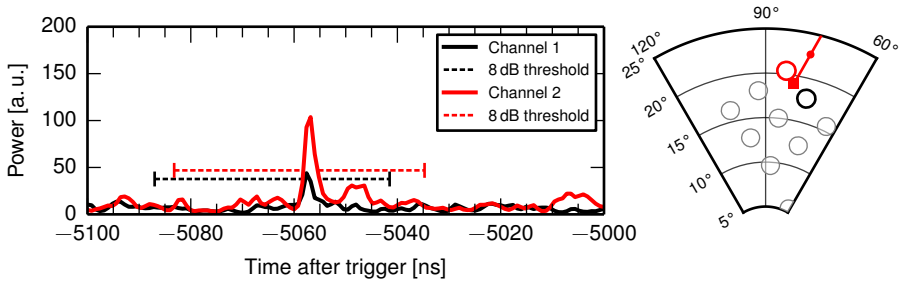


FIG. C.19 • 4/3/2012 4:26. $E = 5.1 \times 10^{17}$ eV, $\theta = 18.7°$, $\Phi = 95.8°$, $R = 157.1$ m, $SNR_1 = 8.5$ dB, $SNR_2 = 11.3$ dB.

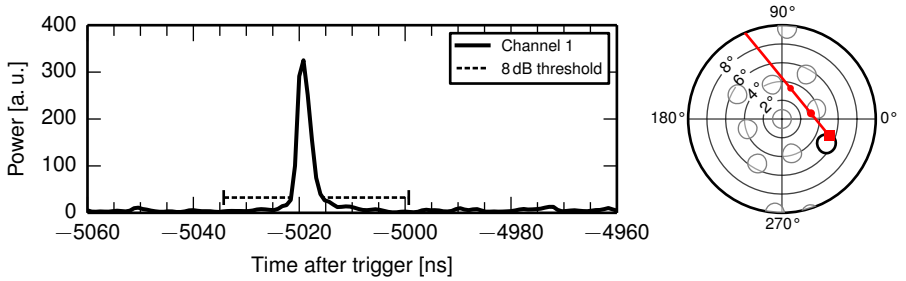


FIG. C.20 • 16/4/2012 23:39. $E = 2.5 \times 10^{17}$ eV, $\theta = 5.6°$, $\Phi = 353.6°$, $R = 119.8$ m, $SNR_1 = 17.7$ dB.

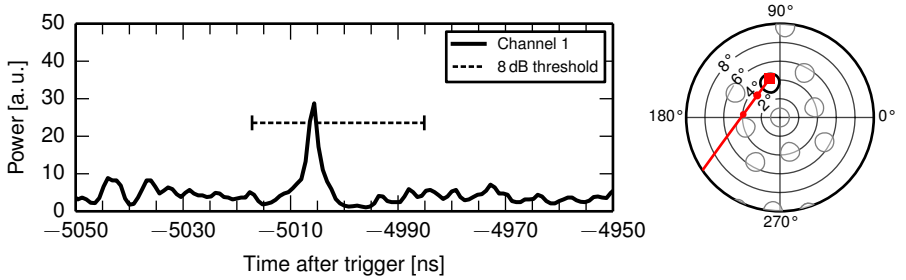


FIG. C.21 • 21/4/2012 11:25. $E = 5.3 \times 10^{16}$ eV, $\theta = 4.5°$, $\Phi = 117.0°$, $R = 87.8$ m, $SNR_1 = 8.7$ dB.

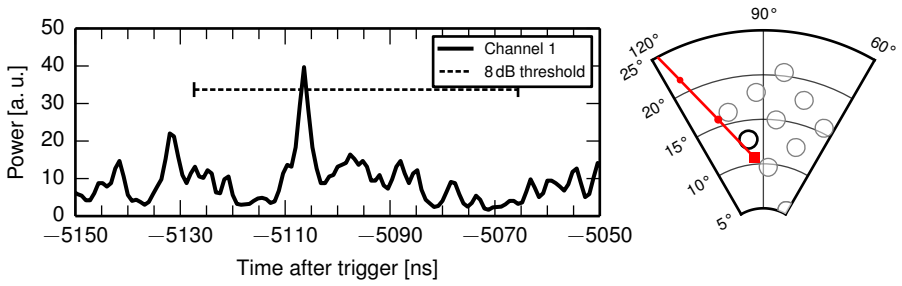


FIG. C.22 • 21/5/2012 21:24. E = $4.3 \times 10^{16}$ eV, θ = 10.3°, Φ = 108.2°, R = 233.6 m, $SNR_1$ = 8.6 dB.

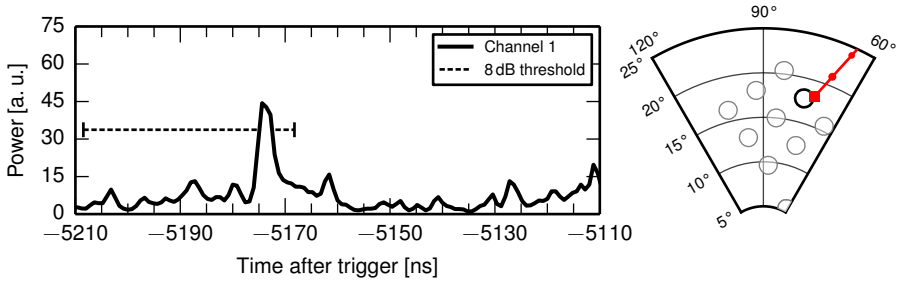


FIG. C.23 • 24/5/2012 20:08. E = $1 \times 10^{17}$ eV, θ = 17.9°, Φ = 87.1°, R = 123.9 m, $SNR_1$ = 9.1 dB.

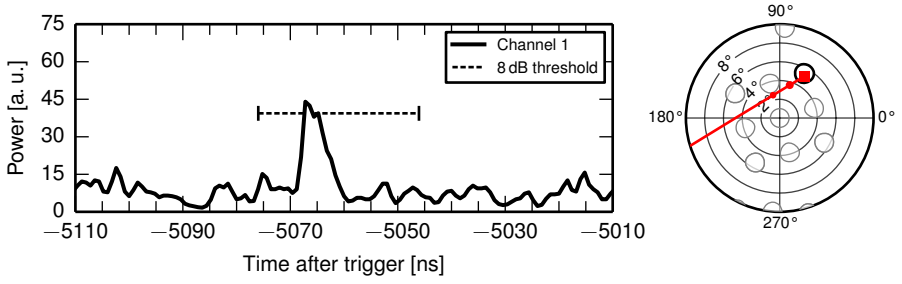


FIG. C.24 • 25/5/2012 15:12. E = $1 \times 10^{17}$ eV, θ = 5.4°, Φ = 73.2°, R = 72.4 m, $SNR_1$ = 8.4 dB.

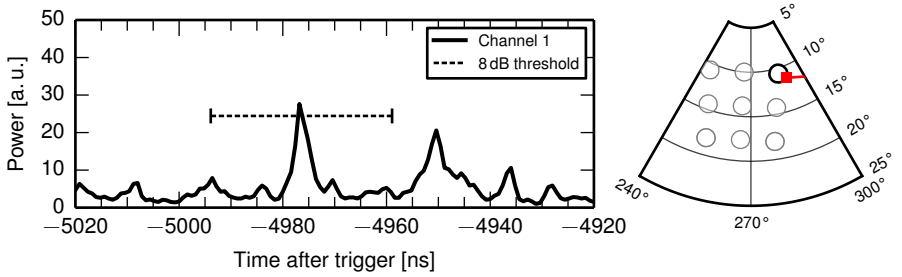


FIG. C.25 • 23/6/2012 14:11. E = $9.9 \times 10^{16}$ eV, θ = 11.3°, Φ = 304.2°, R = 96.3 m, $SNR_1$ = 8.4 dB.

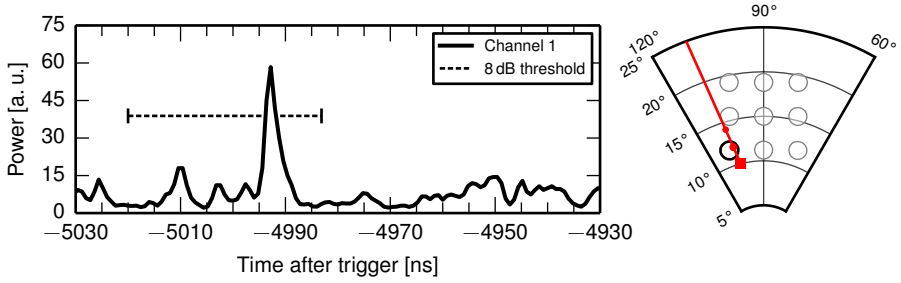


FIG. C.26 • 24/6/2012 9:06. $E = 7.7 \times 10^{16}$ eV, $\theta = 9.9°$, $\Phi = 119.8°$, $R = 77.2$ m, $SNR_1 = 9.6$ dB.

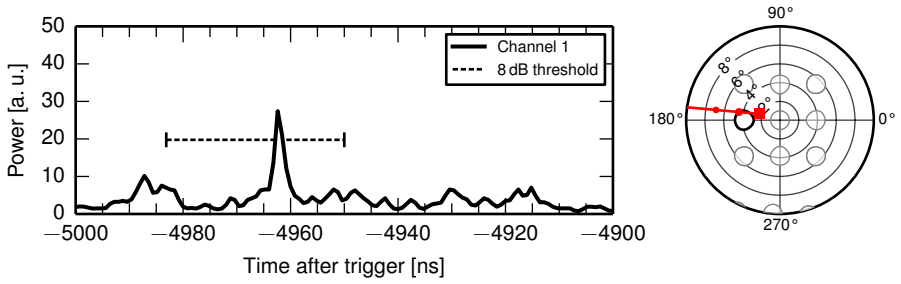


FIG. C.27 • 4/7/2012 22:02. $E = 4.1 \times 10^{16}$ eV, $\theta = 2.0°$, $\Phi = 176.3°$, $R = 86.7$ m, $SNR_1 = 9.3$ dB.

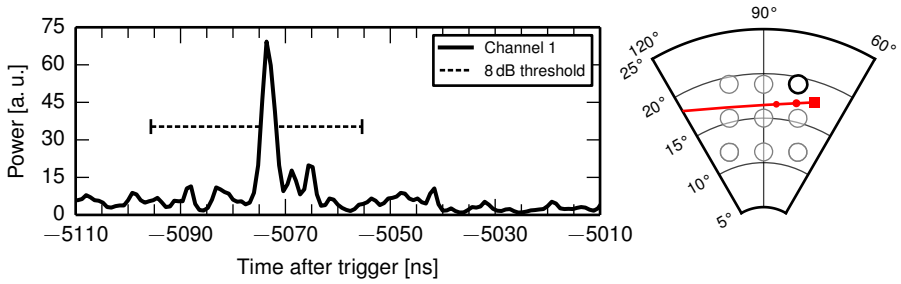


FIG. C.28 • 14/7/2012 22:03. $E = 5.5 \times 10^{16}$ eV, $\theta = 17.8°$, $\Phi = 85.6°$, $R = 77.4$ m, $SNR_1 = 10.8$ dB.

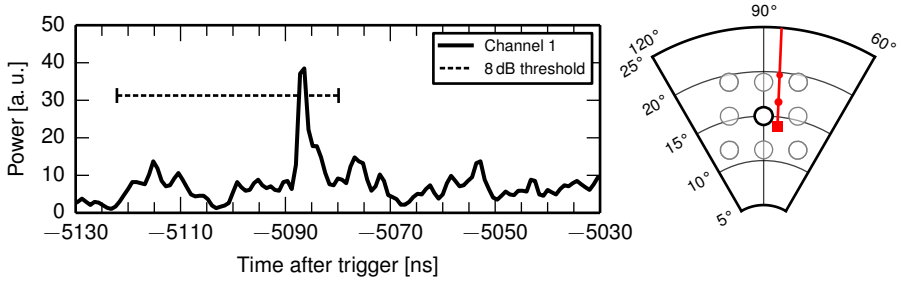


FIG. C.29 • 7/8/2012 13:56. $E = 7.4 \times 10^{16}$ eV, $\theta = 13.5°$, $\Phi = 98.5°$, $R = 113.2$ m, $SNR_1 = 8.8$ dB.

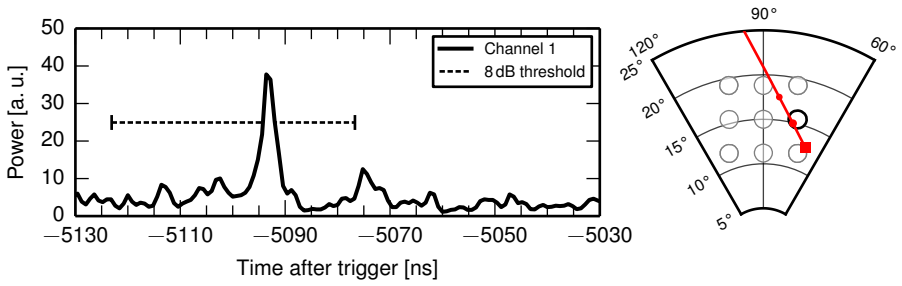


FIG. C.30 • 8/8/2012 17:38. $E = 6.6 \times 10^{16}$ eV, $\theta = 12.5°$, $\Phi = 82.1°$, $R = 120.3$ m, $SNR_1 = 9.7$ dB.

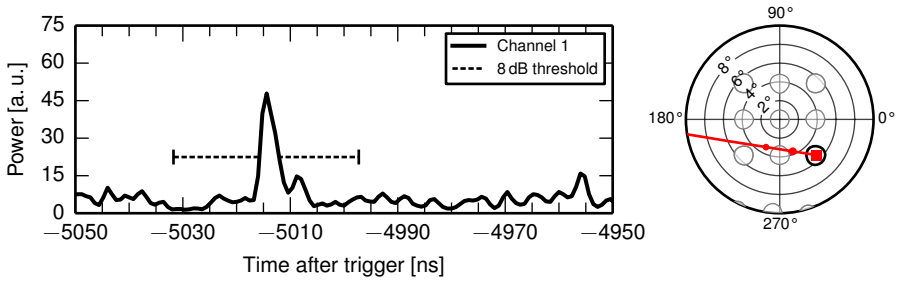


FIG. C.31 • 10/8/2012 1:31. $E = 7.5 \times 10^{16}$ eV, $\theta = 5.7°$, $\Phi = 332.7°$, $R = 100.4$ m, $SNR_1 = 11.1$ dB.

# REFERENCES


[1] R. Engel, D. Heck, and T. Pierog. Extensive air showers and hadronic interactions at high energy. *Ann. Rev. Nucl. Part. Sci.*, 61(1):467–489, 2011. doi: 10.1146/annurev.nucl.012809.104544. (Cited on pages 3, 4, 5, and 6.)

[2] J. Blümer, R. Engel, and J.R. Hörandel. Cosmic rays from the knee to the highest energies. *Prog. Part. Nucl. Phys.*, 63(2):293–338, 2009. (Cited on page 3.)

[3] K. Kotera and A.V. Olinto. The astrophysics of ultrahigh-energy cosmic rays. *Ann. Rev. Astron. Astrophys.*, 49(1):119–153, 2011. doi: 10.1146/annurev-astro-081710-102620. (Cited on page 4.)

[4] K.-H. Kampert and M. Unger. Measurements of the cosmic ray composition with air shower experiments. *Astroparticle Physics*, 35(10):660–678, 2012. doi: 10.1016/j.astropartphys.2012.02.004. (Cited on pages 3 and 6.)

[5] A. Schulz for the Pierre Auger Collaboration. The measurement of the cosmic ray spectrum above $3\times10^{17}$ eV with the Pierre Auger Observatory. *Proc. 33rd ICRC*, 2013. (Cited on page 4.)

[6] T. Abu-Zayyad, R. Aida, M. Allen, et al. [Telescope Array Collaboration]. The cosmic-ray energy spectrum observed with the surface detector of the Telescope Array experiment. *Astrophys. J. Lett.*, 768(1):L1, 2013. doi: 10.1088/2041-8205/768/1/L1.

[7] R. Abbasi, Y. Abdou, M. Ackermann, et al. [IceCube Collaboration]. Cosmic ray composition and energy spectrum from 1–30 PeV using the 40-string configuration of IceTop and IceCube. *Astroparticle Physics*, 42 (0):15–32, 2013. doi: 10.1016/j.astropartphys.2012.11.003.

[8] R. Abbasi, Y. Abdou, T. Abu-Zayyad, et al. [IceCube Collaboration]. All-particle cosmic ray energy spectrum measured with 26 IceTop stations. *Astroparticle Physics*, 44(0):40–58, 2013. doi: 10.1016/j.astropartphys.2013.01.016. (Cited on page 4.)

[9] V.F. Hess. Über Beobachtungen der durchdringenden Strahlung bei sieben Freiballonfahrten. *Physik. Zeitschr.*, 13:1084–1091, 1912. (Cited on page 3.)

[10] L.O'C. Drury. Origin of cosmic rays. *Astroparticle Physics*, 39–40(0): 52–60, 2012. doi: 10.1016/j.astropartphys.2012.02.006. (Cited on page 3.)

[11] W.D. Apel, J.C. Arteaga-Velázquez, K. Bekk, et al. [KASCADE-Grande Collaboration]. KASCADE-Grande measurements of energy spectra for elemental groups of cosmic rays. *Astroparticle Physics*, 47(0):54–66, 2013. doi: 10.1016/j.astropartphys.2013.06.004. (Cited on page 3.)

[12] J.R. Hörandel. Models of the knee in the energy spectrum of cosmic rays. *Astroparticle Physics*, 21(3):241–265, 2004. doi: 10.1016/j.astropartphys.2004.01.004. (Cited on page 3.)

[13] V.S. Berezinsky and S.I. Grigorieva. A bump in the ultra-high energy cosmic ray spectrum. *Astron. Astrophys.*, 199:1–12, 1988. (Cited on page 4.)

[14] V. Berezinsky, A.Z. Gazizov, and S.I. Grigorieva. Dip in UHECR spectrum as signature of proton interaction with CMB. *Phys. Lett. B*, 612(3–4):147–153, 2005. doi: 10.1016/j.physletb.2005.02.058. (Cited on page 4.)

[15] B. Sarkar, K.-H. Kampert, J. Kulbartz, et al. Ultra-high energy photon and neutrino fluxes in realistic astrophysical scenarios. *Proc. 32nd ICRC*, pages 198–201, 2011. (Cited on page 4.)

[16] G.T. Zatsepin and V.A. Kuzmin. Upper limit of the spectrum of cosmic rays. *J. Exp. Theor. Phys. Lett.*, 4:78–80, 1966. (Cited on page 4.)

[17] K. Greisen. End to the cosmic ray spectrum? *Phys. Rev. Lett.*, 16:748–750, 1966. (Cited on page 4.)

[18] A. Haungs, H. Rebel, and M. Roth. Energy spectrum and mass composition of high-energy cosmic rays. *Rep. Prog. Phys.*, 66(7):1145, 2003. doi: 10.1088/0034-4885/66/7/202. (Cited on page 5.)

[19] A. Ferrari, P.R. Sala, A. Fassò, and J. Ranft. FLUKA: A multi-particle transport code (program version 2005). *CERN-2005-010*, 2005. doi: 10.5170/CERN-2005-010. (Cited on pages 6 and 82.)

[20] W.R. Nelson, H. Hirayama, and D.W.O. Rogers. The EGS4 code system. *SLAC-R-265*, 1985. (Cited on page 6.)

[21] D. Heck, J. Knapp, J.N. Capdevielle, G. Schatz, and T. Thouw. CORSIKA: A monte carlo code to simulate extensive air showers. Report FZKA 6019, Forschungszentrum Karlsruhe, 1998. (Cited on pages 6, 25, 73, and 80.)

[22] S.J. Sciutto. AIRES: A system for air shower simulations. 1999. arXiv:astro-ph/9911331. (Cited on page 6.)

[23] S. Ostapchenko. QGSJet-II: towards reliable description of very high energy hadronic interactions. *Nucl. Phys. B—Proc. Supp.*, 151(1):143–146, 2006. doi: 10.1016/j.nuclphysbps.2005.07.026. (Cited on pages 6, 25, and 82.)

[24] E.-J. Ahn, R. Engel, T.K. Gaisser, P. Lipari, and T. Stanev. Cosmic ray interaction event generator SIBYLL 2.1. *Phys. Rev. D*, 80:094003, 2009. doi: 10.1103/PhysRevD.80.094003. (Cited on page 6.)

[25] J.W. Fowler, L.F. Fortson, C.C.H. Jui, et al. A measurement of the cosmic ray spectrum and composition at the knee. *Astroparticle Physics*, 15(1): 49–64, 2001. doi: 10.1016/S0927-6505(00)00139-0. (Cited on page 7.)

[26] S.F. Berezhnev, D. Besson, N.M. Budnev, et al. The Tunka-133 EAS Cherenkov light array: Status of 2011. *Nucl. Instrum. Meth. A*, 692(0):98–105, 2012. doi: 10.1016/j.nima.2011.12.091. (Cited on page 7.)

[27] J.A. Hinton for the HESS Collaboration. The status of the H.E.S.S. project. *New Astron. Rev.*, 48:331–337, 2004. (Cited on page 7.)

[28] J.V. Jelley, J.H. Fruin, N.A. Porter, et al. Radio pulses from extensive cosmic-ray air showers. *Nature*, 205(4969):327–328, 1965. (Cited on page 8.)

[29] D.J. Fegan. Detection of elusive radio and optical emission from cosmic-ray showers in the 1960s. *Nucl. Instrum. Meth. A*, 662, Supplement 1(0): S2–S11, 2012. doi: 10.1016/j.nima.2010.10.129. (Cited on page 8.)

[30] D.J. Fegan and P.J. Slevin. Radio pulses from extensive air showers at 520 MHz. *Nature*, 217(5127):440–441, 1968. doi: 10.1038/217440a0. (Cited on page 8.)

[31] R.E. Spencer. Radio pulses from cosmic ray air showers at 44, 105, 239 and 408 MHz. *Nature*, 222(5192):460–461, 1969. doi: 10.1038/222460a0. (Cited on page 8.)

[32] H. Falcke, W.D. Apel, A.F. Badea, et al. Detection and imaging of atmospheric radio flashes from cosmic ray air showers. *Nature*, 435(7040): 313–316, 2005. doi: 10.1038/nature03614. (Cited on page 8.)

[33] D. Ardouin, A. Bellétoile, D. Charrier, et al. Radioelectric field features of extensive air showers observed with CODALEMA. *Astroparticle Physics*, 26(4–5):341–350, 2006. doi: 10.1016/j.astropartphys.2006.07.002. (Cited on page 8.)

[34] F.D. Kahn and I. Lerche. Radiation from cosmic ray air showers. *Proc. Roy. Soc. A*, 289(1417):206–213, 1966. (Cited on pages 8 and 82.)

[35] T. Huege, M. Ludwig, O. Scholten, and K.D. de Vries. The convergence of EAS radio emission models and a detailed comparison of REAS3 and MGMR simulations. *Nucl. Instrum. Meth. A*, 662, Supplement 1(0): S179–S186, 2012. doi: 10.1016/j.nima.2010.11.041. (Cited on page 8.)

[36] G.A. Askaryan. Coherent radio emission from cosmic showers in air and in dense media. *J. Exp. Theor. Phys.*, 48:658–659, 1965. (Cited on pages 8 and 82.)

[37] S. Grebe. *Finger on the pulse of cosmic rays*. PhD thesis, Radboud University Nijmegen, 2013. (Cited on page 8.)

[38] F.G. Schröder. *Instruments and Methods for the Radio Detection of High Energy Cosmic Rays*. PhD thesis, Karlsruher Institut für Technologie (KIT), 2010. (Cited on page 8.)

[39] W. D. Apel, J. C. Arteaga, L. Bähren, et al. [LOPES Collaboration]. Experimental evidence for the sensitivity of the air-shower radio signal to the longitudinal shower development. *Phys. Rev. D*, 85:071101, 2012. doi: 10.1103/PhysRevD.85.071101. (Cited on page 8.)

[40] N. Palmieri for the LOPES collaboration. Investigation on the energy and mass composition of cosmic rays using LOPES radio data. *Proc. 33rd ICRC*, 2013. (Cited on page 8.)

[41] D. Ardouin, C. Cârloganu, D. Charrier, et al. First detection of extensive air showers by the TREND self-triggering radio experiment. *Astroparticle Physics*, 34(9):717–731, 2011. doi: 10.1016/j.astropartphys.2011.01.002. (Cited on page 8.)

[42] P. Abreu, M. Aglietta, M. Ahlers, et al. [Pierre Auger Collaboration]. Antennas for the detection of radio emission pulses from cosmic-ray induced air showers at the Pierre Auger Observatory. *JINST*, 7(10):P10011, 2012. doi: 10.1088/1748-0221/7/10/P10011. (Cited on page 9.)

[43] A. Corstanje, M. van den Akker, L. Bähren, et al. LOFAR: Detecting cosmic rays with a radio telescope. *Proc. 32nd ICRC*, 2011.

[44] F.G. Schröder, D. Besson, N.M. Budnev, et al. Tunka-Rex: A radio antenna array for the Tunka experiment. *AIP Conference Proceedings*, 1535(1):111–115, 2013. doi: 10.1063/1.4807531. (Cited on page 8.)

[45] W.D. Apel, J.C. Arteaga, L. Bähren, et al. LOPES-3D: An antenna array for full signal detection of air-shower radio emission. *Nucl. Instrum. Meth. A*, 696(0):100–109, 2012. doi: 10.1016/j.nima.2012.08.082. (Cited on page 8.)

[46] J. Abraham, M. Aglietta, I.C. Aguirre, et al. Properties and performance of the prototype instrument for the Pierre Auger Observatory. *Nucl. Instrum. Meth. A*, 523(1–2):50–95, 2004. doi: 10.1016/j.nima.2003.12.012. (Cited on page 9.)

[47] H. Kawai, S. Yoshida, H. Yoshii, et al. Telescope Array experiment. *Nucl. Phys. B*, 175–176(0):221–226, 2008. doi: 10.1016/j.nuclphysbps.2007.11.002. (Cited on page 9.)

[48] P.W. Gorham, N.G. Lehtinen, G.S. Varner, et al. Observations of microwave continuum emission from air shower plasmas. *Phys. Rev.*, D78: 032007, 2008. doi: 10.1103/PhysRevD.78.032007. (Cited on pages 9, 18, and 81.)

[49] P. Neunteufel, S. Baur, R. Engel, et al. Microwave emission due to molecular bremsstrahlung in non-thermal air shower plasmas. 2013. (Cited on pages 9, 80, and 84.)

[50] R. Gaïor for the Pierre Auger Collaboration. Detection of cosmic rays using microwave radiation at the Pierre Auger Observatory. *Proc. 33rd ICRC*, 2013. (Cited on page 10.)

[51] J. Alvarez-Muñiz, E. Amaral Soares, A. Berlin, et al. The MIDAS telescope for microwave detection of ultra-high energy cosmic rays. *Nucl. Instrum. Meth. A*, 719(0):70–80, 2013. doi: 10.1016/j.nima.2013.03.030. (Cited on page 10.)

[52] J. Alvarez-Muñiz, A. Berlin, M. Bogdan, et al. Search for microwave emission from ultrahigh energy cosmic rays. *Phys. Rev. D*, 86:051104, 2012. doi: 10.1103/PhysRevD.86.051104. (Cited on page 10.)

[53] P. Facal San Luis. Status of the program for microwave detection of cosmic rays at the Pierre Auger Observatory. *EPJ Web of Conferences*, 53: 08009, 2013. doi: 10.1051/epjconf/20135308009. (Cited on page 10.)

[54] S. Ogio, T. Yamamoto, K. Kuramoto, et al. Search for molecular bremsstrahlung radiation signals in Ku band with coincidental operations of radio telescopes with air shower detectors. *J. Phys. Conf. Ser.*, 409 (1):012091, 2013. doi: doi:10.1088/1742-6596/409/1/012091. (Cited on page 10.)

[55] J. Alvarez-Muñiz, M. Bohácová, G. Cataldi, et al. The air microwave yield (AMY) experiment to measure the GHz emission from air shower plasmas. *EPJ Web of Conferences*, 53:08011, 2013. doi: 10.1051/epjconf/20135308011. (Cited on pages 11 and 94.)

[56] C. Williams, M. Bohácová, C. Bonifazi, et al. First results from the microwave air yield beam experiment (MAYBE): Measurement of GHz radiation for ultra-high energy cosmic ray detection. *EPJ Web of Conferences*, 53:08008, 2013. doi: 10.1051/epjconf/20135308008. (Cited on pages 11 and 94.)

[57] T. Shibata, A. Enomoto, S. Fukuda, et al. Absolute energy calibration of FD by an electron linear accelerator for Telescope Array. *AIP Conf. Proc.*, 1367(1):44–49, 2011. doi: 10.1063/1.3628713. (Cited on pages 11 and 94.)

[58] J. Blümer, R. Engel, P. Facal, et al. Search for microwave signals from air showers with the Electron Light Source at Telescope Array. *Proc. 33rd ICRC*, 2013. (Cited on pages 11 and 94.)

[59] D.M. Pozar. *Microwave Engineering*. Wiley, 4th edition, 2011. ISBN 9780470631553. (Cited on pages 13, 99, and 100.)

[60] C.A. Balanis. *Modern Antenna Handbook*. Wiley, 2008. ISBN 9780470294147. (Cited on pages 13 and 101.)

[61] A.R. Kerr and J. Randa. Thermal noise and noise measurements—a 2010 update. *Microwave Magazine, IEEE*, 11(6):40–52, 2010. doi: 10.1109/MMM.2010.937732. (Cited on page 15.)

[62] H. Nyquist. Thermal agitation of electric charge in conductors. *Phys. Rev.*, 32:110–113, 1928. doi: 10.1103/PhysRev.32.110. (Cited on page 15.)

[63] R.H. Dicke. The measurement of thermal radiation at microwave frequencies. *Rev. Sci. Instrum.*, 17(7):268–275, 1946. doi: 10.1063/1.1770483. (Cited on page 15.)

[64] ITU-R. Radio noise. *ITU-R recommendation*, P.372-10, 2009. (Cited on page 17.)

[65] H.J. Liebe, G.A. Hufford, and M.G. Cotton. Propagation modeling of moist air and suspended water/ice particles at frequencies below 1000 GHz. *Proc. NATO/AGARD Wave Propagation Panel, 52nd meeting*, 3:1–10, 1993. (Cited on pages 16 and 17.)

[66] B.M. Oliver. Search strategies. In J. Billingham, editor, *Life in the Universe*, pages 351–376, 1981. (Cited on page 16.)

[67] A. Bucholtz. Rayleigh-scattering calculations for the terrestrial atmosphere. *Applied Optics*, 34(15):2765–2773, 1995. doi: 10.1364/AO.34.002765. (Cited on page 18.)

[68] P.J.B. Clarricoats and G.T. Poulton. High-efficiency microwave reflector antennas—a review. *Proc. IEEE*, 65(10):1470–1504, 1977. doi: 10.1109/PROC.1977.10750. (Cited on page 19.)

[69] R.C. Johnson and H. Jasik. *Antenna Engineering Handbook*. Electronics: Electrical engineering. McGraw-Hill Professional Publishing, 1993. ISBN 9780070323810. (Cited on page 19.)

[70] W.A. Imbriale, P. Ingerson, and W. Wong. Large lateral feed displacements in a parabolic reflector. *Antennas and Propagation, IEEE Transactions on*, 22(6):742–745, 1974. doi: 10.1109/TAP.1974.1140910. (Cited on page 19.)

[71] TICRA. GRASP9 technical description. URL `http://www.ticra.com/`. (Cited on pages 19 and 55.)

[72] Y. Lo. On the beam deviation factor of a parabolic reflector. *Antennas and Propagation, IRE Transactions on*, 8(3):347–349, 1960. doi: 10.1109/TAP.1960.1144854. (Cited on page 20.)

[73] T. Antoni, W.D. Apel, F. Badea, et al. [KASCADE Collaboration]. The cosmic-ray experiment KASCADE. *Nucl. Instrum. Meth. A*, 513(3):490–510, 2003. doi: 10.1016/S0168-9002(03)02076-X. (Cited on page 24.)

[74] W.D. Apel, J.C. Arteaga, A.F. Badea, et al. [KASCADE-Grande Collaboration]. The KASCADE-Grande experiment. *Nucl. Instrum. Meth. A*, 620 (2-3):202–216, 2010. doi: 10.1016/j.nima.2010.03.147. (Cited on pages 24 and 25.)

[75] M. Bertaina, W.D. Apel, J.C. Arteaga, et al. [KASCADE-Grande Collaboration]. The all particle energy spectrum of KASCADE-Grande in the energy region $10^{16}$–$10^{18}$ eV by means of the $N_{ch} - N_{\mu}$ technique. In *Proc. 31st ICRC*, number 323, 2009. (Cited on page 25.)

[76] M. Bertaina, W.D. Apel, J.C. Arteaga, et al. [KASCADE-Grande Collaboration]. The cosmic ray energy spectrum in the range $10^{16}$–$10^{18}$ eV measured by KASCADE-Grande. *Astrophys. Space Sci. Trans.*, 7:229–234, 2011. (Cited on page 25.)

[77] F. Cossavella. *Measurements of high energy cosmic rays above 10 PeV with KASCADE-Grande*. PhD thesis, Universität Karlsruhe (TH), 2009. (Cited on pages 25 and 70.)

[78] S. Mathys. Nachweis von Luftschauern mit einer Radioantenne im GHz-Bereich. Diploma thesis, Bergische Universität Wuppertal, 2011. (Cited on page 25.)

[79] P. Papenbreer. Analyse von Luftschauerdaten gemessen mit GHz Radioantennen. Master's thesis, Bergische Universität Wuppertal, 2013.

[80] S. Mathys, S. Baur, M.E. Bertaina, et al. [CROME Collaboration]. Extensive air shower detection with CROME in the L band. *AIP Conf. Proc.*, 1535(1):219–223, 2013. doi: 10.1063/1.4807552.

[81] L. Petzold. Konzeption, Realisierung und Kalibrierung einer 3.4 m Parabolantenne für das L-Band zum Nachweis der kosmischen Höhenstrahlung. Master's thesis, Hochschule Karlsruhe Technik und Wirtschaft, 2013. (Cited on pages 25 and 111.)

[82] M. Gérardin. Analysis of VLF radio measurements measured in the CROME experiment. Project report, Université de Nantes and Karlsruhe Institute of Technology (KIT), 2013. (Cited on page 25.)

[83] Boost C++ libraries. URL `http://www.boost.org/`. (Cited on page 32.)

[84] J. Seward. bzip2. URL `http://www.bzip.org/`. (Cited on page 32.)

[85] G. van Rossum et al. The Python language reference. URL `http://docs.python.org/release/2.7/reference/`. (Cited on page 32.)

[86] A. Tridgell and P. Mackerras. The rsync algorithm. *Joint Comp. Sci. Tech. Rep. Ser. of The Australian National University*, TR-CS-96-05, 1996. (Cited on page 33.)

[87] Riverbank Computing Limited. PyQt4: Python bindings for Qt 4. URL `http://www.riverbankcomputing.co.uk/software/pyqt/`. (Cited on page 33.)

[88] P.F. Dubois, K. Hinsen, and J. Hugunin. Numerical Python. *Computers in Physics*, 10(3), 1996. (Cited on page 33.)

[89] J.D. Hunter. Matplotlib: A 2d graphics environment. *Computing In Science & Engineering*, 9(3):90–95, 2007. (Cited on page 33.)

[90] jQuery. URL `http://www.jquery.com/`. (Cited on page 33.)

[91] Flot: Attractive JavaScript plotting for jQuery. URL http://www.flotcharts.org/. (Cited on page 33.)

[92] ZX47-60+ coaxial power detector. URL http://www.minicircuits.com/pdfs/ZX47-60+.pdf. (Cited on page 39.)

[93] AD8318 logarithmic amplifier, . URL http://www.analog.com/static/imported-files/data_sheets/AD8318.pdf. (Cited on pages 39 and 42.)

[94] AD8307 logarithmic amplifier, . URL http://www.analog.com/static/imported-files/data_sheets/AD8307.pdf. (Cited on pages 41 and 42.)

[95] E. Nash. Measurement and control of RF power (part III), 2000. URL http://www.analog.com/static/imported-files/tech_articles/561216689RF_Power_Meas_Part_I.pdf. (Cited on page 41.)

[96] P. Gorham. private communication, 2013. (Cited on page 52.)

[97] S.J. Orfanidis. Electromagnetic waves and antennas. URL http://www.ece.rutgers.edu/~orfanidi/ewa/. (Cited on page 55.)

[98] A. Ludwig. Computation of radiation patterns involving numerical double integration. *Antennas and Propagation, IEEE Transactions on*, 16 (6):767–769, 1968. doi: 10.1109/TAP.1968.1139296. (Cited on page 55.)

[99] P.M. Johansen. Uniform physical theory of diffraction equivalent edge currents for truncated wedge strips. *Antennas and Propagation, IEEE Transactions on*, 44(7):989–995, 1996. doi: 10.1109/8.504306. (Cited on page 55.)

[100] D. Einfeld, E. Huttel, F. Perez, M. Pont, and G.K. Sahoo. Commissioning results of ANKA. In *Proceedings of the 2001 Particle Accelerator Conference*, volume 4, pages 2683–2685 vol.4, 2001. doi: 10.1109/PAC.2001.987872. (Cited on pages 62 and 63.)

[101] Institute for Meteorology and Climate Research—Troposphere Research, Karlsruhe Institute of Technology (KIT). 200 m meteorological tower at KIT Campus North. URL http://www.imk.kit.edu/messmast. (Cited on page 62.)

[102] M.I. Skolnik. *Introduction to Radar Systems*. Electrical Engineering Series. McGraw-Hill Book Company, 1980. ISBN 9780070579095. (Cited on page 63.)

[103] D. Kickelbick. *The energy spectrum of cosmic rays measured with the KASCADE-Grande experiment*. PhD thesis, Universität Siegen, 2008. (Cited on page 63.)

[104] M. Stümpert. *Suche nach Anisotropie in der kosmischen Strahlung mit KASCADE-Grande*. PhD thesis, Universität Karlsruhe (TH), 2008. (Cited on page 65.)

[105] P.J. Rousseeuw and K. Van Driessen. A fast algorithm for the minimum covariance determinant estimator. *Technometrics*, 41:212–223, 1998. (Cited on page 65.)

[106] R. Brun and F. Rademakers. ROOT: An object oriented data analysis framework. *Nucl. Instrum. Meth. A*, 389:81–86, 1996. Proceedings AIHENP'96 Workshop, Lausanne; see also `http://root.cern.ch`. (Cited on page 69.)

[107] D. Kang. private communication, 2010. (Cited on page 70.)

[108] R.C. Weast, editor. *CRC Handbook of Chemistry and Physics*. 67th edition, 1986. (Cited on page 73.)

[109] J.M. Rüeger. *Refractive index formulae for electronic distance measurement with radio and millimetre waves*, volume S-68 of *Unisurv Reports*, pages 1–52. School of Surveying and Spatial Information Systems, University of South Wales, 2002. (Cited on page 73.)

[110] C.J. Clopper and E.S. Pearson. The use of confidence or fiducial limits illustrated in the case of the binomial. *Biometrika*, 26(4):404–413, 1934. (Cited on page 76.)

[111] F. Nerling, J. Blümer, R. Engel, and M. Risse. Universality of electron distributions in high-energy air showers—description of Cherenkov light production. *Astroparticle Physics*, 24(6):421–437, 2006. doi: 10.1016/j.astropartphys.2005.09.002. (Cited on page 81.)

[112] L. Perrone, S. Petrera, and F. Salamida. Gaisser-Hillas profiles and FD simulation. *Auger technical note GAP-2005-087*, 2005. (Cited on page 81.)

[113] D. Góra, R. Engel, D. Heck, et al. Universal lateral distribution of energy deposit in air showers and its application to shower reconstruction. *Astroparticle Physics*, 24(6):484–494, 2006. doi: 10.1016/j.astropartphys.2005.09.007. (Cited on page 81.)

[114] R. Engel, F. Salamida, R. Smida, M. Unger, and F. Werner. Microwave yield estimation for EAS simulation. Auger technical note GAP-2012-013, 2012. (Cited on page 82.)

[115] T. Huege, M. Ludwig, and C.W. James. Simulating radio emission from air showers with CoREAS. *AIP Conf. Proc.*, 1535(1):128–132, 2013. doi: 10.1063/1.4807534. (Cited on pages 82 and 84.)

[116] C.W. James, H. Falcke, T. Huege, and M. Ludwig. General description of electromagnetic radiation processes based on instantaneous charge acceleration in "endpoints". *Phys. Rev. E*, 84:056602, 2011. doi: 10.1103/PhysRevE.84.056602. (Cited on page 82.)

[117] J. Alvarez-Muñiz, W.R. Carvalho, A. Romero-Wolf, M. Tueros, and E. Zas. Coherent radiation from extensive air showers in the ultrahigh frequency band. *Phys. Rev. D*, 86:123007, 2012. doi: 10.1103/PhysRevD.86.123007. (Cited on pages 84 and 92.)

[118] K.D. de Vries, A.M. van den Berg, O. Scholten, and K. Werner. Coherent cherenkov radiation from cosmic-ray-induced air showers. *Phys. Rev. Lett.*, 107:061101, 2011. doi: 10.1103/PhysRevLett.107.061101. (Cited on page 84.)

[119] T. Pierog, M.K. Alekseeva, T. Bergmann, et al. First results of fast one-dimensional hybrid simulation of EAS using conex. *Nucl. Phys. B—Proc. Supp.*, 151(1):159–162, 2006. doi: 10.1016/j.nuclphysbps.2005.07.029. (Cited on page 90.)

[120] J. Alvarez-Muñiz, W.R. Carvalho Jr., and E. Zas. Monte Carlo simulations of radio pulses in atmospheric showers using ZHAireS. *Astroparticle Physics*, 35(6):325–341, 2012. doi: 10.1016/j.astropartphys.2011.10.005. (Cited on page 92.)

[121] F. Werner. Design and test of a flying light source for the calibration of the Auger fluorescence telescopes. Diploma thesis, Karlsruhe Institute of Technology (KIT), 2010. (Cited on page 101.)

[122] Mikrokopter website. URL `http://www.mikrokopter.de/`. (Cited on page 101.)

[123] u-blox AG. GPS compendium, 2009. URL `http://www.u-blox.com/en/tutorials-links-gps.html`. (Cited on page 103.)

[124] Wikipedia. Eulersche Winkel. URL `http://de.wikipedia.org/w/index.php?title=Eulersche_Winkel&oldid=122203611`. Retrieved on 3.9.2013. (Cited on page 104.)

[125] M. Clutton-Brock. Likelihood distributions for estimating functions when both variables are subject to error. *Technometrics*, 9(2):261–269, 1967. (Cited on page 116.)

[126] A.H.G. Rinnooy Kan and G.T. Timmer. Stochastic global optimization methods part II: Multi level methods. *Mathematical Programming*, 39(1): 57–78, 1987. doi: 10.1007/BF02592071. (Cited on page 116.)

[127] S.G. Johnson. The nlopt nonlinear-optimization package. URL `http://ab-initio.mit.edu/nlopt`. (Cited on page 116.)